Planar droplet sizing – LIF/Mie

Johannes Peterleithner

Diploma Thesis at the Institute for Thermal Turbomachinery
and Machine Dynamics
University of Technology Graz, Austria

Head of the Institute and Examiner: Univ.-Prof. Dr.-Ing. Franz Heitmeir
Supervisor at TU Graz: Ao. Univ.-Prof. DI Dr. techn. Jakob Woisetschläger
Supervisor at Alstom: Dr.-Ing Thierry Lachaux

STATUTORY DECLARATION

I declare that I have authored this thesis independently, that I have not used other than the declared sources / resources and that I have explicitly marked all material which has been quoted either literally or by content from the used sources.

.... date (signature)

Acknowledgements

This thesis was written during and after my time at ALSTOM Ltd. (Birr, Switzerland) in Birr, Switzerland. The thesis got clearance for publication by Alstom.

I would like to thank the employees at the department ‘LabTesting’ (TTTVG-LT) for their warm hospitality and the friendly atmosphere. Particularly I would like to mention Dr. Michael Gritsch for giving me the opportunity of writing this Thesis in the industrial research at Alstom, Dr. Thierry Lachaux, my supervisor who supported me beyond the call of duty and Mr. Dieter Schönwälder from the laboratories who always had practical solutions for my technical questions.

I would also like to thank Ao.Univ.-Prof. Dr. Jakob Woisetschläger and Univ.-Prof. Dr. Franz Heitmeir from the Institute for Thermal Turbomachinery and Machine Dynamics for the support and revision of this Thesis.

And finally my girlfriend Callie for being understanding and supporting me to go abroad for the time of the thesis.

Abstract

Fuel flexibility became a selling point in the gas turbine market recently. For efficient combustion of liquid fuels, knowledge about droplet diameters in sprays is essential. Some methods exist for point measurements but a planar system is required in order to shorten measurement periods, to gain detailed information about the spray. The goal of the thesis was to acquire deeper understanding of a planar measurement technique using the techniques of laser-induced-fluorescence and Mie-scattering (LIF/Mie), which is capable of measuring the Sauter mean diameter (SMD) of small droplets and particles, a commonly used size in combustion research.

In a first step appropriate nozzles are chosen and the characteristics described in the datasheets provided by the manufacturer were verified with a Shadowgraphy system from LaVision and a laser-diffraction system from Malvern.

The main part analyzes the properties the LIF/Mie system such as the behavior when measuring high- or low-density sprays. This technique relies on the assumption that fluorescent light intensity is proportional to the cubed diameter whereas Mie scattering is proportional to the squared diameter of droplets and particles. Division of those two signals results in a ratio, proportional to the diameter. The intensity ratio must then be calibrated with an absolute measurement technique in order to get absolute diameter values.

An investigation of the Mie signals dependency on the scattering angle has been carried out and a new setup consisting of 2 CCD cameras and a beam splitter is compared to the classic system using an image doubler coupled with an ICCD camera. Both setups have not been built up or used at Alstom before.

In detail, the influence of background subtraction and dark images, a setup for reference image acquisition and a procedure of calibration are described.

The finally designed and tested system was applied to the ‘ATMO’ test rig at the Alstom Test Lab in Birr, Switzerland. All experimental work was done at Alstom.

Table of contents

List of Figures

List of Tables

1 Introduction

1.1 Motivation

Alstom is a global acting corporation, employing 92,600 people. Overall sales were around 19.9 billion Euros in 2011/2012. The French company is a big player in transportation business, mostly known for designing the ‘Train à grande vitesse’ or TGV and the cruiser RMS Queen Mary II.

In 2000 Alstom acquired the entire Gas turbine business from Asea Brown Boveri (ABB Ltd), former Brown Boveri & Cie (BBC), who built the world‘s first commercially used industrial gas turbine plant in 1938.

Today their turbines GT24 and GT26, featuring sequential combustion, are known for minimal emissions and exceptional part load performance. In Birr, Switzerland the engines are designed and manufactured. The Testing and Validation department’s Spray Lab is regularly used for experiments on nozzles and combustors. The underlying experiments for this thesis were carried out there as well.

Increased application of renewables gives gas turbines a new role in power supply. Part load performance along with start up time become more and more important in order to balance electricity fluctuations of renewable sources such as wind and solar power. Recent developments emphasize emission reduction rather than further increasing the ratio of efficiency.

At the same time, attention has been turned to fuel flexibility. The 2005 Russia–Ukraine gas dispute clearly pictured Europe’s dependency on natural gas. This desired flexibility is also a driver for research on liquid fuels. The demand of fuel flexibility, part load performance and low emission makes deeper knowledge of sprays in combustors necessary.

Most crucial, is the so-called Sauter Mean Diameter (SMD) of fuel droplets, a commonly used parameter in combustion.

Computational approaches to two-phase flows are still deficient, therefore making experiments is extremely necessary. While point-measurement techniques such as phase-Doppler-anemometry (PDA) or shadowgraphy are established and reliable, they have their limitations with dense sprays. They are also very slow, if the whole spray must be analyzed.

An alternative was found with the planar droplet sizing system LIF/Mie. The method is capable of recording an entire plane at once. The whole spray can be defined with a few measurement positions. Drawback is a decreased accuracy compared to shadowgraphy or PDA. Application of the system has not been carried out yet.

1.2 Thesis Object

The sizing system LIF/Mie was planned to be the main instrument for quick experimental spray analysis at the Lab testing department.

For that, prove of functionality and a detailed characterization of the measurement system is necessary.

Firstly, the measurement samples must be chosen. The nozzles investigated within this thesis must cover the range of droplet size, as occurring in combustion and the density of the spray should be low enough to allow shadowgraphy measurements. Some preexisting information about the spray should be available in order to have a guideline.

Furthermore, the nozzles should be characterized with existing equipment, such as Shadowgraphy and diffractometry. Those are also necessary for calibration, as LIF/Mie only provides a signal, proportional to the diameter, not an absolute value.

An investigation of Mie scattering and its dependency on the scattering angle was necessary in order to clear doubts about the validity of the system.

In terms of application, the entire camera support and mounts had to be designed and built up at the ATMO, an atmospheric test rig with a vertical duct and consequently very low gas velocity. The design included considerations, so the setup could easily be adapted to the closed loop High Density Fluid Channel (HDFC) which was the second rig in the Spraylab, where momentum ratios of a high-pressure situation can be simulated using C2F6.

The Lab was not equipped with an ICCD camera. Therefore an alternative setup with 2 cameras had to be built up and compared to the ICCD setup.

Part of the task was to design, order and install the water supply for the measurements. Finally, a comparison between the different nozzles and measurement systems had to be made, in order to show the capabilities of the system, and formulate a recommendation.

2 Physical Background

2.1 Laser Induced Fluorescence

Fluorescence imaging is a tool conventionally used for visualization of mixing flows. For low laser power (I_v), LIF is linear with the number density (N_l) and the exciting laser power. This can be used for concentration measurements when mixing flows. Firstly a pulsed laser is in use because its short pulse width of less than 10 nanoseconds can freeze the image. Secondly a light sensitive CCD- or intensified camera necessary and finally a tracer capable of fluorescence must be used.

Fluorescence is the emitted radiation of a molecule when it decays spontaneously from a higher to a lower energy level via intermediate energy levels.

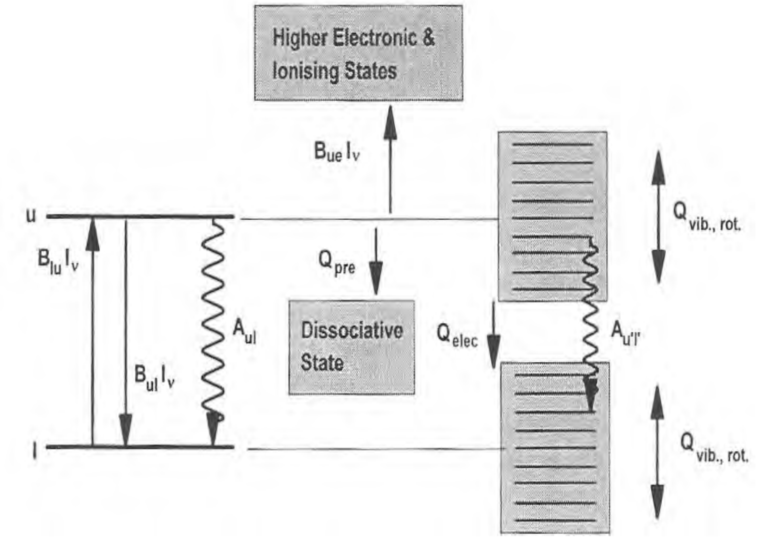

Figure 1: Energy transfer processes in LIF (Source: Greenhalgh, 1994).

In order to get the molecule into a higher level, in LIF it is pumped by photons emitted by a laser. For low laser intensity the whole process is controlled by the laser power I_v, the number density of absorber particles per fluid volume, N_l and Einstein's absorption rate coefficient, B_{lu}. With indices l and u for lower and upper level of energy. De-excitation can occur in several ways. Most likely relaxation or energy exchanges (Q_{vib}, Q_{rot}) convert the energy, but a small part causes spontaneous emission. This part is proportional to the number density N_u and Einstein's coefficient for spontaneous emission, A_{ul}.

More processes of energy conversion such as predissociation (Q_{pre}) and electronic quenching (Q_{elec}) are present, they are not individually described but accounted for by the term quenching, Q. A simplified two-level system, presenting the most important effects, is shown in **Figure 1**. The relation of the parameters explained above is shown in Formula **(1)**.

$$I_{LIF} = N_l \times B_{lu} \times I_v \times \frac{A_{ul}}{A_{ul} + Q} \qquad \textbf{(1)}$$

The quenching effect Q can be neglected under certain circumstances. During the experiments it was not considered.

An important side effect of fluorescence is, that its wavelength is generally longer than the one of the laser photons used for excitation of the molecules. This enables the user to cut off the laser light during experiments. Given the laboratory is dark, only fluorescence is recorded.

In order to apply LIF to droplet sizing, equation **(1)** must be rearranged. The parameter C_1 represents all influences of the measurement setup. Therefore it can be considered constant as long as the measurement setup is not altered (laser power, tracer concentration etc.), I_{LIF} is only proportional to the amount of tracer particles (N_l) when quenching can be neglected.

$$I_{LIF} = N_l \times B_{lu} \times I_v \times \frac{A_{ul}}{A_{ul} + Q} = C_1 \times N_l \tag{2}$$

When considering droplets in air, water with fluorescent dye of constant concentration (C_{conc}) is used. Assuming the concentration is kept constant, the droplets are spherical and evaporation is low, the following equation can be derived:

$$I_{LIF} = C_1 \times N_l = C_1 \times C_{conc} \times V = C_1 \times C_{conc} \times \frac{\pi}{6} d^3 \propto d^3 \tag{3}$$

Laser-induced-fluorescence applied to droplet measurement is therefore proportional to d cubed.

2.2 Lorenz-Mie theory

The Lorenz-Mie theory is the theoretical approach to light interaction with spheres. It is a closed solution of the Maxwell equations, and well documented by Born and Wolf (1980). The calculations are very complex and therefore usually solved by means of a Computer program such as Mieplot (Laven, 2011, *http://www.philiplaven.com/mieplot.htm*).

In **Figure 2** a very simplified model of light interaction with a particle is shown. The main processes are reflection and refraction of several orders, while low orders up to the 3rd mainly contribute to the overall intensity distribution. Considering not only one ray as in **Figure 2** but a planar wave, produces a scattering distribution as shown in Figure 3. The summed Mie scattering is black. It consists of diffraction (mainly at 0° forward scattering) and reflection shown by the red curve. First order refraction (green) gradually reduces with increased angle until

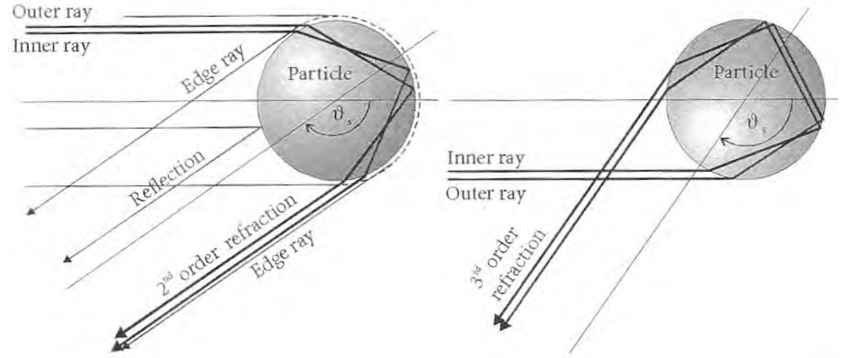

Figure 2: 2nd order and 3rd order refraction on a droplet (Source: Greenhalgh, 1994).

above 100° backscattering, while 2nd order refraction increases with angle in the region of backscattering. Heavy oscillations are inherent to it.

In order to calculate an intensity of Mie scattering three parameters must be defined. Firstly the ratio m of refractive indices for the particle, n_p, and the ambient phase n_a is given by:

$$m = \frac{n_p}{n_a} = \frac{n_{pi}+i\times n_{pi}}{n_{ar} + i\times n_{ai}} \tag{4}$$

The refractive indices are expressed in complex numbers, where the imaginary part represents absorption.

Secondly, the Mie parameter x_{Mie} which is a ratio of the particle diameter d_p and the incident wavelength λ can be calculated as follows:

$$x_{Mie} = \frac{\pi\times d_p}{\boldsymbol{\lambda}} \tag{5}$$

The third parameter is the scattering angle Θ. While the refractive angle ratio m is a system parameter, droplet diameter d_p and scattering angle Θ may vary during the experiments.

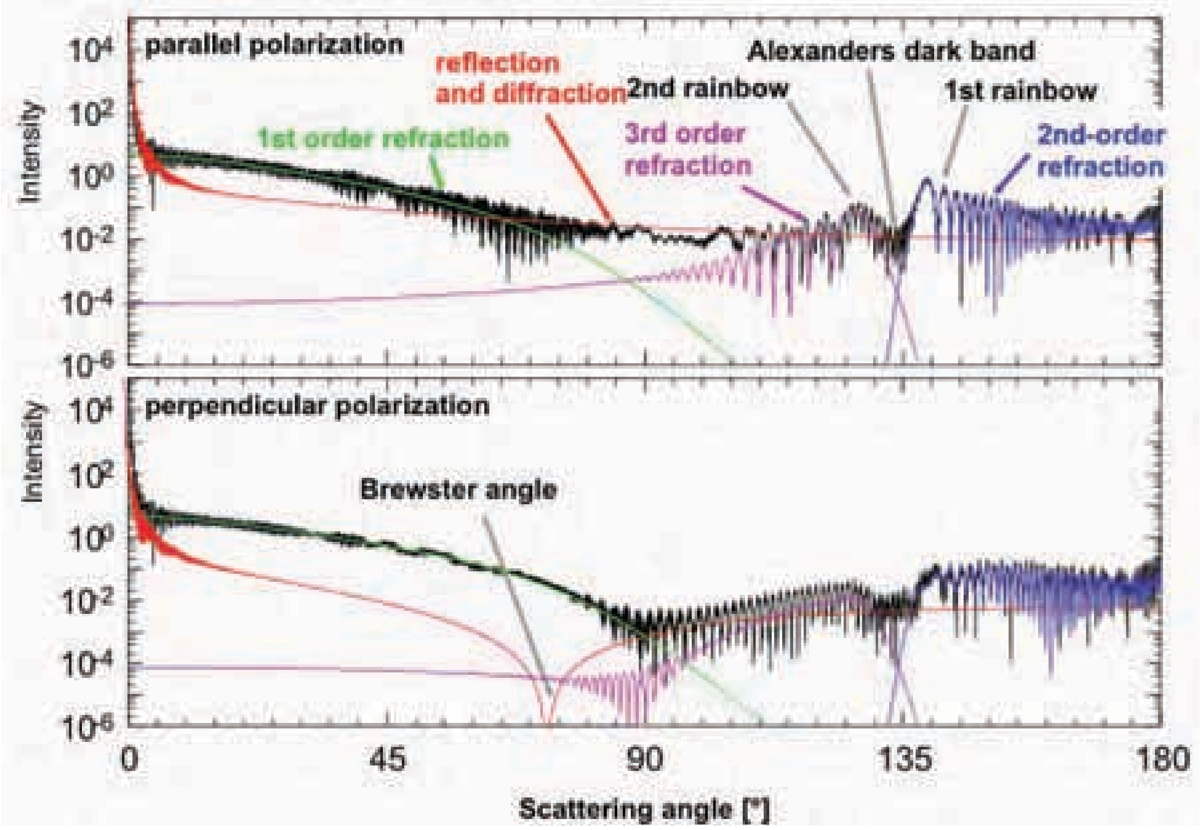

Figure 3: The intensity distribution over the scattering angle for a refractive index ratio m = 1.333 and a Mie parameter x= 643 (d=100µm , λ=488nm) (Source: Albrecht et al. 2003). Parallel means parallel to the polarization of the incoming light beam.

While the Mie theory is generally valid for light-sphere-interaction regardless of the droplet diameter, for completeness three particular cases can be distinguished:

$x_m << 1$: Elastic scattering also referred to as Rayleigh scattering can be described with a more simple equations which deliver good results for small particles. As shown in Figure 4, the scattering intensity in this region is proportional to d to the power of 6.

$x_m > 10$: When the diameter of the particle is large compared to the incident light, the rules of geometrical optics may be applied. Then the intensity is proportional to d to the power of 2.

$1 < x_m < 10$: In the transitional zone between Rayleigh scattering and geometrical optics heavy oscillations of scatter intensity occur. This size region is referred to as Lorenz-Mie region (Albrecht et al 2003).

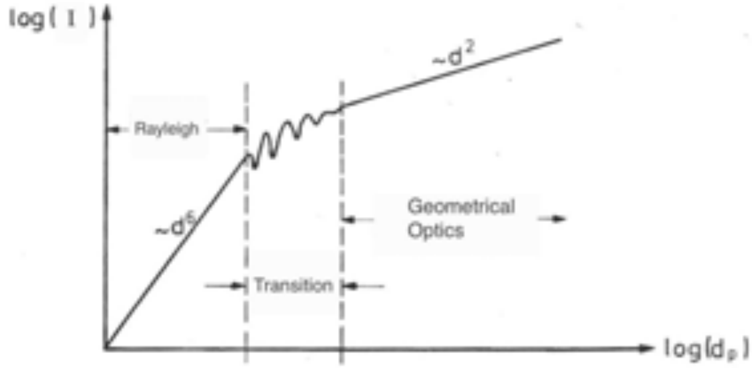

Figure 4: Scattering as a function of particle diameter, for a constant incident wavelength and a constant scattering angle (Source: Ruck, 1987).

While the Mie theory is valid for all droplet diameters, the assumption,

$$I_{Mie} \propto d^2 \tag{6}$$

which is necessary for LIF/Mie sizing, is only valid for diameters greater than 1.6 µm when radiated with a wavelength of 532nm typical for a frequency doubled Nd:YAG laser. As shown during the experiments of this thesis, a certain scattering angle must be kept as well. Backward scattering is not very favorable.

2.3 Sauter mean diameter

The Sauter mean diameter (SMD) is the diameter of a droplet with the same ratio of volume (V_d) to surface area (A_d) as the entire spray. It is commonly used in combustion engineering since the surface area is an important parameter for vaporization speed which influences combustion and the volume of fuel is proportional to the power.

The diameter is defined as follows:

$$d_{32} = \frac{\sum V_d}{\sum A_d} \tag{7}$$

2.4 LIF/Mie droplet sizing

The general idea of LIF/Mie droplet sizing is to divide a signal proportional to volume of the droplet (I_{LIF}) by a signal proportional to surface area of the droplet (I_{Mie}). The resulting intensity ratio (I_{ratio}) is then proportional to the Sauter Mean Diameter (SMD). This is shown in Figure 5.

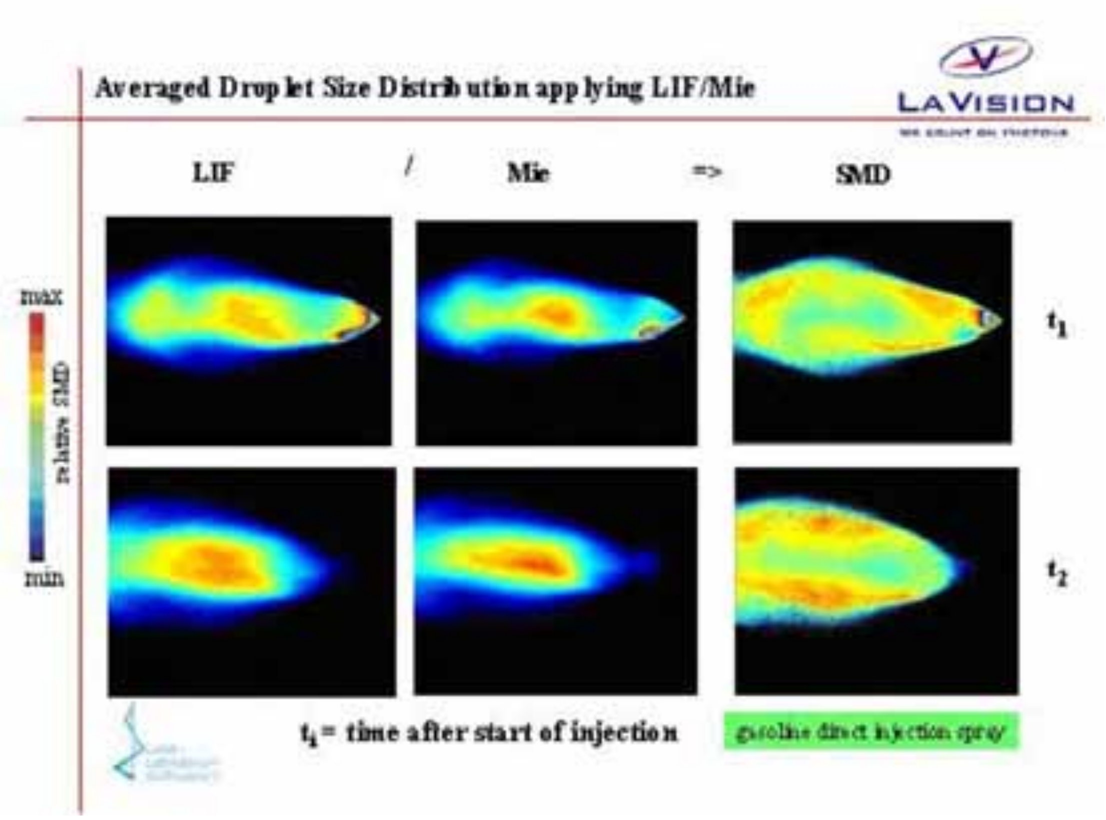

Figure 5: Division of the LIF signal by the Mie signal gives a Map of Sauter mean diameters (Source: LaVision Product manual, 1004052_SprayMaster_D32_D80).

First, a single droplet is considered, with the proportionality factors a_{LIF}, a_{Mie} and A.

$$I_{ratio} = \frac{I_{LIF}}{I_{Mie}} = \frac{a_{LIF} \times d_p^3}{a_{Mie} \times d_p^2} = A \times d_p \tag{8}$$

Applying this idea to a dense spray, where many droplets will be illuminated at once, the signal received by the cameras will be the sum of light of all droplets. Integration over the number N of particles must therefore be applied to the formula above.

$$I_{ratio} = \frac{\int_{d_p=0}^{\infty} I_{LIF}(d_p) \times dN(d_p)}{\int_{d_p=0}^{\infty} I_{Mie}(d_p) \times dN(d_p)} \tag{9}$$

Replacing the Intensity of the individual particle, gives:

$$I_{ratio} = \frac{\int_{d_p=0}^{\infty} a_{LIF} \times {d_p}^3 \times dN(d_p)}{\int_{d_p=0}^{\infty} a_{Mie} \times {d_p}^2 \times dN(d_p)} \tag{10}$$

As a_{LIF} and a_{Mie} are assumed to be constant, they can be put in front of the integration term.

$$I_{ratio} = \frac{a_{LIF}}{a_{Mie}} \times \frac{\int_{d_p=0}^{\infty} {d_p}^3 \times dN(d_p)}{\int_{d_p=0}^{\infty} {d_p}^2 \times dN(d_p)} \tag{11}$$

The division of those integration terms is exactly the definition of the Sauter Mean Diameter (SMD or d_{32}).

$$d_{32} = \frac{\int_{d_p=0}^{\infty} {d_p}^3 \times dN(d_p)}{\int_{d_p=0}^{\infty} {d_p}^2 \times dN(d_p)} \tag{12}$$

Therefore the intensity ratio is directly proportional to the SMD:

$$I_{ratio} = A \times d_{32} \tag{13}$$

Theoretically, the proportionality factor A should be constant. Calibration with a Measurement system, giving an absolute value for a droplet diameter, like phase-Doppler-anemometry (PDA) enables the user to gain a planar map of SMD values.

Several investigations have been carried out on the topic, and some researchers disagree on the correctness of the fundamental hypothesis of the LIF/Mie technique. For further readings, one should consult Charalampous and Hardalupas (2011 a & b). Among general investigations regarding LIF/Mie, they have also introduced a method reducing sizing error due to the fact that neither I_{Mie} nor I_{LIF} are exactly proportional to d^2 respectively d^3. In fact the exponent can slightly vary. Furthermore they have put together a comprehensive list of papers published on the topic.

3 Materials

3.1 Coordinate System

During the experiments, the origin oft the coordinate system was set at the orifice of the nozzles investigated. The z-axis points down vertically while the x-axis was directed into the laser head. The y-axis was then defined by the requirement of a right-handed coordinate system, shown in Figure 7 and Figure 6. In contrast to other experimental setups, not the measurement system, but the nozzle was traversed. It was mounted on a three-axis mechanical strut system to support the equipment, which defined a second coordinate system, rotated with an angle of 23° in the horizontal plane. Repositioning of the nozzle required a coordinate transformation.

3.2 Nozzles – Standard conditions

Part of the thesis's object was the search for appropriate nozzles. There was no typical reference nozzle for droplet sizing, which could have been used as reference for other nozzles or the measurement system. It was important to find a nozzle, which from then on could be used as a standard nozzle for the Spraylab. If there would be any uncertainties about results or the accuracy of a measuring system, this nozzle could be used to calibrate the sizing system again or at least see if the system produced the same diameters. It was important that some sort of information about

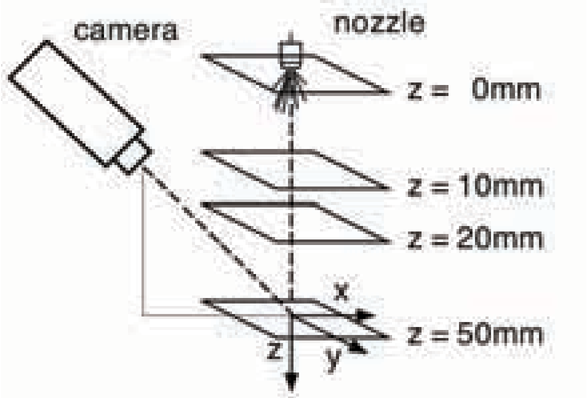

Figure 6: The allignement of nozzle and camera in the coordinate system. The z-coordinate is zero at the orifice. The camera is located in the x-z plane.

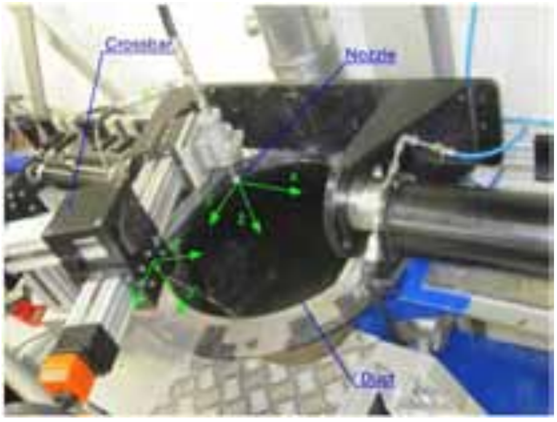

Figure 7: Vertical test rig with the nozzle coordinate system x, y, z, and the coordinate system x', y', z' of the mechanical struts used to support the equipment. The image also shows the Malvern diffraction system.

the produced spray exist, particularly the Sauter mean diameter (SMD) being the most important characteristic in combustion.

Five main requirements were set:

- Information about the spray behavior, especially the droplet size must have been available. Ideally, a scientific paper should have been published.
- The droplet diameter should have been in the range of 10 µm to 200 µm, which was the region of interest in combustion injection.
- A low spray density was desired in order to achieve results with shadowgraphy.
- The required pressure and flow rate must have been manageable with the existing equipment in the Alstom Spray Lab.
- Availability

The biggest problem was, that many nozzle producers did provide a SMD for their product but did not specify, where exactly in the spray they measured or which system they used. Also great production variations caused an uncertainty when choosing the appropriate nozzle.

The most promising nozzle was the IP-16 from Mee Industries Inc. (Mee Industries Inc. Monrovia, California, USA) used for inlet fogging of stationary gas turbines. It was described previously in two papers written for the ASME TURBO EXPO (Chaker et al. 2002 & 2003) and was provided from Mee Industries Inc. Those papers can be found online (http://www.meefog.com/downloads/white-papers/wp-gt-38801-experimental-and-analytical-investigations.pdf and http://www.meefog.com/downloads/white-papers/wp-gt-30563part-b-fog-droplet-sizing-analysis.pdf).

Figure 8: The Mee nozzle with its impaction pin. On the surface of the nozzle, facing the impaction pin, is the orifice measuring 0.15mm in diameter.

Figure 9: The Le1 flat cone nozzle tip is secured with a cap nut.

Figure 10: The Le2 nozzle is designed similar to the Le1 only with increase massflow.

Disadvantages of the Mee-nozzle were an asymmetric and very dense spray. Because of the good documentation and the very small droplets generated, it was chosen anyways.

The German manufacturer Lechler (Lechler GmbH, Metzingen, Germany) provided a datasheet for certain flat cone nozzles used in industrial applications. Not as detailed as a scientific paper, it lacked the type of measurement used for characterization and only gave an axial distance between the orifice and the measurement point. Never the less, it provided a diameter and a droplet distribution. Finally two Alstom oil pilot nozzles were used in order to prove the systems capability of providing results for a real gas turbine application. In Table 1, all nozzles that have been used during the experiments, are listed.

Throughout the project, the nozzle from ‘Mee IP-16 was referred to as ‘Mee’. The small nozzle from Lechler was abbreviated with ‘Le1’ and the bigger one as ‘Le2’. Standard conditions were defined for each of them. Those were set in any measurement if not stated differently. These conditions can also be found in Table 1.

Table 1 Nozzles with properties and Serial Number

Type	Manu-facturer	Manufacturers Serial	Expected SMD / µm	Standard conditions		
				Δp / mbar	Flowrate / gs^{-1}	Δz / mm
Mee	Mee Industries Inc.	IP-16	10	138000	2.83	50
Le1	Lechler	652.307.17.00.00.0	12 .2	4500	8.17	5 0
Le2	Lechler	652.516.30.00.00.0	240.1	3500	41.7	150
OP-P12	Alstom	-		-	-	-
OP 7	Alstom			-	-	-

3.3 Test Rigs

The Spray Lab at Alstom in Birr Switzerland consists of two test rigs. One is a closed loop High Density Fluid Channel, where momentum ratios of a high-pressure situation can be simulated using C2F6. This gas has a density about 6 times higher than air at ambient conditions.

The second rig (**Figure 29**), called atmospheric test rig (ATMO) was a vertical duct, with very low gas velocity. The open inlet design enabled high flexibility with measurements and quick setups. A low gas velocity was a necessary requirement for the assumption that the spray expanded into still air. Several metal bars, painted blue in (**Figure 29**) were available for mounting additional equipment.

Figure 11: Atmospheric test rig with power control, fan, duct, nozzle mount and crossbar.

3.3.1 Water Supply Chain

For the experiments Rhodamine 6g was used as a fluorescent tracer added to deionized watera 500-liter Rhodamine tank (Figure 12) was ordered. For mixing the Rhodamine solution a continuous flow pump (Figure 13) was installed. It was also necessary in order to deliver the required primary pressure for the main pump (Figure 14). This pump needed about half a bar primary pressure in order to avoid cavitation. It has been custom built earlier, equipped with a wobble plate pump, two equalizing tanks and a frequency converter for revolution regulation. Because of the equalizing tanks, the pump delivered a continuous flow. A maximum pressure of 140 bars was possible. Depending on the nozzle, the flow rate was measured with one of the coriolis flow meters (Figure 15). The smaller one was able to measure up to 21 g/s, the bigger one had a maximum flow rate of 250 g/s.

Figure 12: Rhodamine tank

Figure 13: Feed water pump

Figure 14: High pressure pump

Figure 15: Flowmeter 1 and 2

3.3.2 Hydraulic Configurations

Two different setups were built up. One for fluorescent tracer, the other one for tap water supply.

Configuration number one (Figure 16) shows the setup with the tank. The temperature of the liquid was recorded, since the bypass of the pumps fed back into the tank. Especially at low flow rates in combination with high pressure, the temperature increased considerably. Cycle one (Figure 16) was only for mixing the solution. The bypass was shut in experimental operation. Then, if necessary, bypass 2 (Figure 16) was active. Just before the nozzle, the flow meters and a pressure tapping point were located.

Configuration number two (Figure 17) was similar. Only the tank was replaced by the factory's water tap, which provided demineralized water. Then the 1st stage pump was not necessary anymore, since the tap water provided enough primary pressure for the system. Finally, the bypass led into the drain. This setup was only in use with shadowgraphy and diffractometry, since these techniques do not require any tracer.

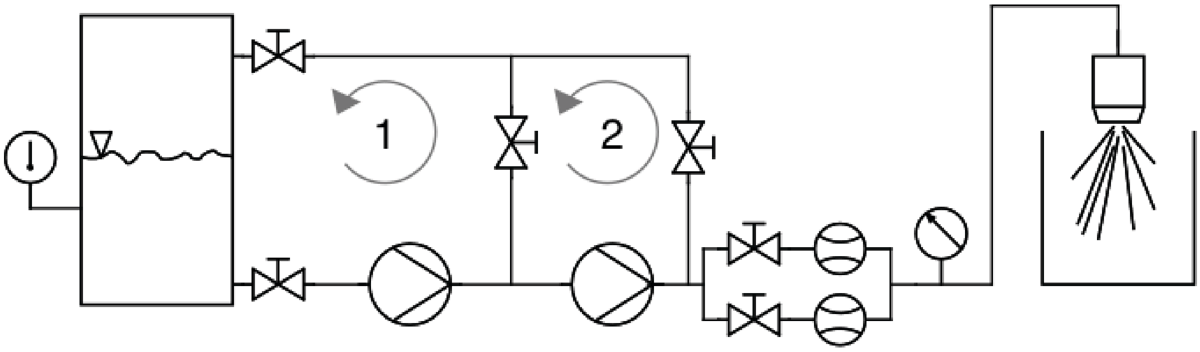

Figure 16: Hydraulic configuration 1 for tracer usage

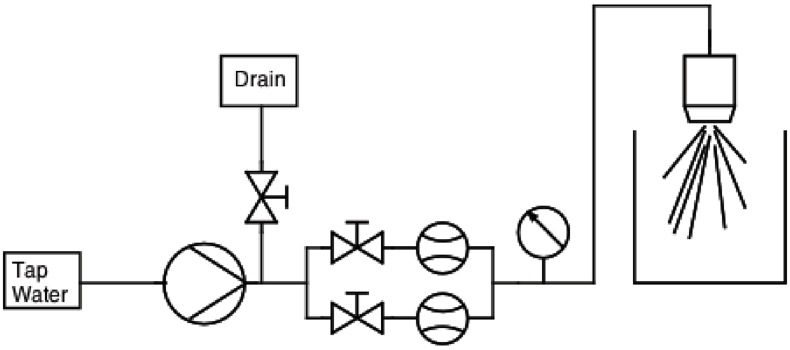

Figure 17: Hydraulic configuration for tap water supply

3.4 D32 Calibration Systems

3.4.1 Shadowgraphy – 'LaVision Particle Master Shadow'

The measurement principle of the LaVision shadowgraphy is shown in **Figure 18** (LaVision, Göttingen, Germany). A light source is pointed at the particles of interest, and a camera is set up behind the particles having the same optical axis as the light source. The imaging system is 'looking into the light'. Whenever a particle crosses, its shadow is imaged on the cameras CCD-chip. Once calibrated, the system can estimate the particles diameter. The laser's Pulse length of only 5 nano seconds guaranteed a sharp image of the particles.

Since the particles of interest measured down to only a couple of micrometers, a long distance microscope was required in order to magnify the measurement area. Highly dense sprays and the fact that the microscope only used part of the light, asked for a very bright light source, capable of a high on-off-switch rate. One option was to use a Nd:YAG Laser with a diffusor head scattering the light. The Labs Measurement Computer 'PIV-/Spray Machine' was used for recording and processing the images just as for controlling the laser.

In our case, the system, which has been provided by LaVision, measured an area of 2.1mm by 1.575mm. Only droplets, which were in focus less than several

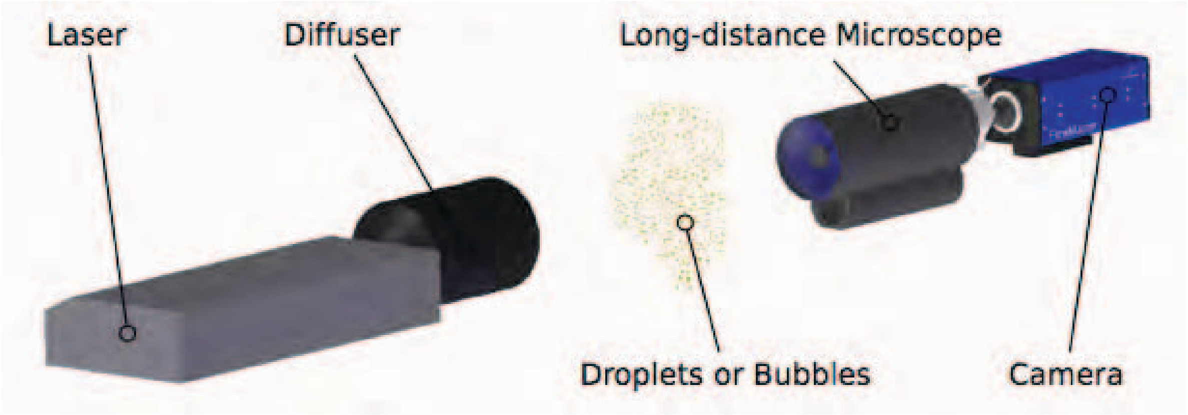

Figure 18: Shadowgraphy Setup suggested by LaVision (Source: LaVision Product manual, 1003014_ParticleMaster_Shadow_D72).

micrometers have been taken into consideration. Therefore the system was considered a point measurement technique.

3.4.2 Malvern Spraytec

Figure 19: Malvern Spraytec

The Spraytec is based on the optical effect of diffraction and sold by Malvern Instruments Ltd (Malvern, United Kingdom). The smaller the droplets, the larger the diffraction pattern (Airy rings) in the focal plane of the imaging lens. Any size distribution in the spray will so convolute to a diffraction pattern in the focal plane. From this intensity distribution a droplet size distribution can be deconvoluted by the

algorithms provided by the software. The system consisted of a laser head and a receptor head connected to each other with a stiff aluminum bar construction. In (**Figure 19**) the Malvern diffraction system is presented on a short baseplate. During the measurements, the long plate was used in order to span the opening of the ATMO test rig. The system was splash waterproof and the openings were protected from droplets by purge-air. The laser beam had a diameter of 10mm. The distance between the two heads times the cross-section of the laser represent the measurement volume. Since the system integrated over the volume, a high resolution in space was not achievable.

3.5 LIF/Mie – Planar Droplet Sizing

The measurement system used, was assembled by Lavision. The company developes the software and distributes rebranded hardware from other suppliers. The setup shown in Figure 20 was built up within the scope of the thesis. In use was a Nd:YAG laser including a laser arm for flexibility and a sheet optic mounted on it. Each of the two laser units had it’s own cooler with a manual remote control necessary during sheet adjustments. During experiments, the laser was controlled by an internal ‘Programmable Timing Unit’ (PTU). This device also triggered the image acquisition. It enabled the user to fully control the measurement with the computer using LaVision’s Davis software. The raw image data was moved directly from the cameras to an internal frame grabber card and then stored on a raid bundle.

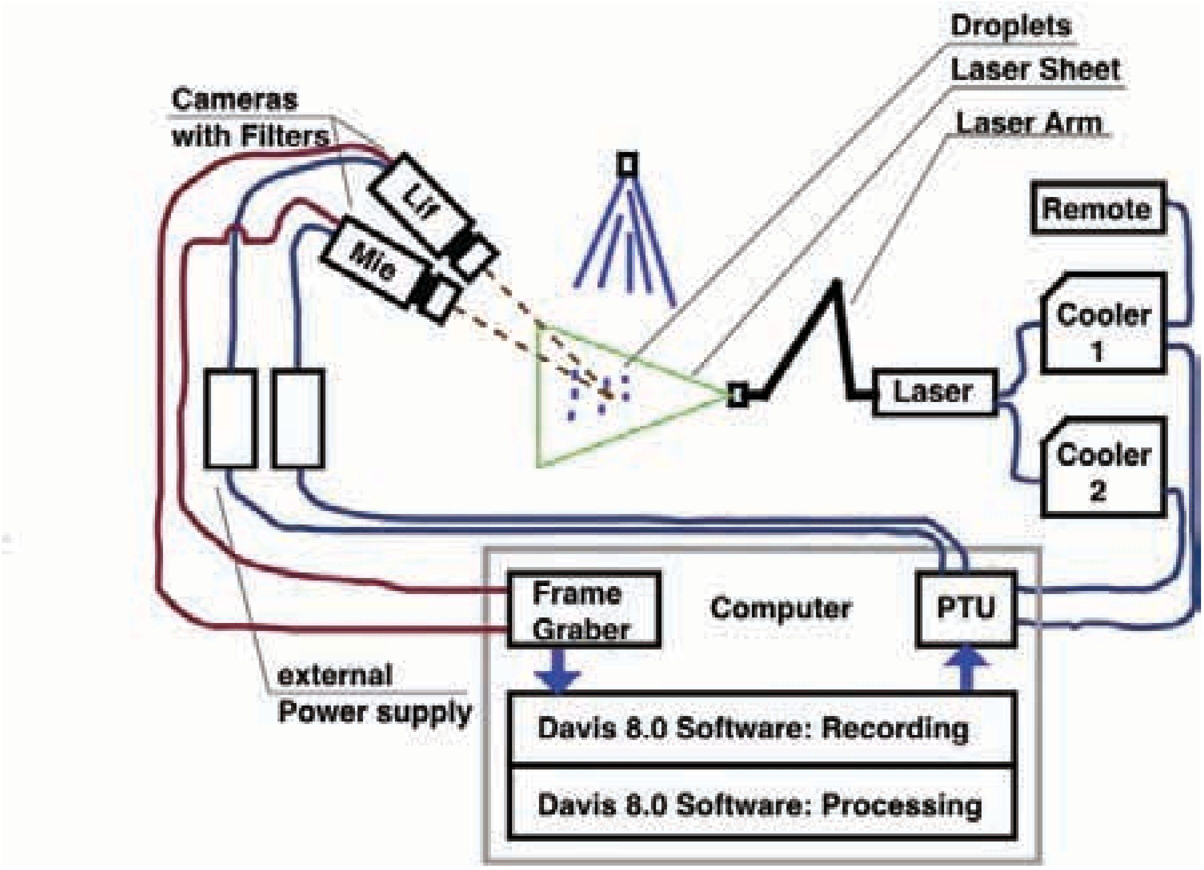

Figure 20: Measurement setup for LIF/Mie Planar Droplet sizing, here in the configuration with two separate cameras.

3.5.1 Laser

The Nd:YAG laser was a 'Gemini PIV 15' make from New Wave Research, Inc. (Fremont, California, USA). The PIV version of the laser was already frequency doubled to 532nm wavelength and included two laser heads with an optical arrangement joining them to one beam of vertical polarization. It featured 120mJ pulse energy with a pulse length of 5 nanoseconds and a beam diameter of 5mm. Repetition rates of up to 15Hz were possible. It lacked an optical attenuator, therefore power had to be controlled by changing the flash lamp energy. This is not common for adjustable systems, especially at low power it causes instabilities. Sometimes a pulse was missing, and the laser worked intermittently.

For our high power demands with certain nozzles, the offset between the pulses of Laser 1 and 2 was set to zero. Then the pulse energy was doubled. For setup flexibility and laser safety, a laser guiding arm was attached. The other side of the arm was mounted onto the sheet optics, which is described in chapter 5.1.

3.5.2 CCD Camera

There are two LaVisions Imager Pro X2M cameras available in the lab. Their charge-coupled devices (CCD) had a resolution of 1600 by 1200 pixels and could generate images with 14bit, equivalent of 16384 gray levels. For reduced chip noise, the camera was peltier-cooled and the power unit was in an external housing. The minimal exposure time of the shutter was 0.5 µs.

3.5.3 ICCD Camera

Because there was no intesified CCD (ICCD) camera in the Spraylab, the LaVision Nanostar camera was borrowed from the Waterlab. It could be gated down to 10 nanoseconds and used a 1280 by 1024 pixel CCD-chip with 12bits. The Intensifier was not optimized for our desired region of 532nm to 600nm but still reached enough intensification in this area to make up for the loss of light, caused by the image doubler.

3.5.4 Beam splitter

Two plate-beam splitters from 'Edmund Optics' were used. One (Stock Nr NT31 434) had a reflection of 25% and a transition of 75%, the other one (Stock Nr NT31 433) had a distribution of 50% each. They were nonreflective coated on the backside and measured 76 by 51 mm.

3.5.5 Image doubler

The image doubler from LaVision projected two copies of one image on a single camera chip. It enabled a very compact setup with just one camera and one objective. As a drawback the aperture of the lens had to be closed at least to f-stop 16 better 22 in order to properly separate the two images. In (**Figure 21**) the optical path of the image doubler is shown. The core pieces included two mirrors on the sides, and a prism located in the center. Filters were mounted in front of each mirror.

3.5.6 Filters

The LIF camera (recording the LIF image) was equipped with a SCHOTT OG550 long pass filter for the fluorescence signal. Three were ordered in case, one would not cut off enough of the Mie signal intensity (elastic scatter, at the laser frequency). A transmission curve can be found in the Appendix.

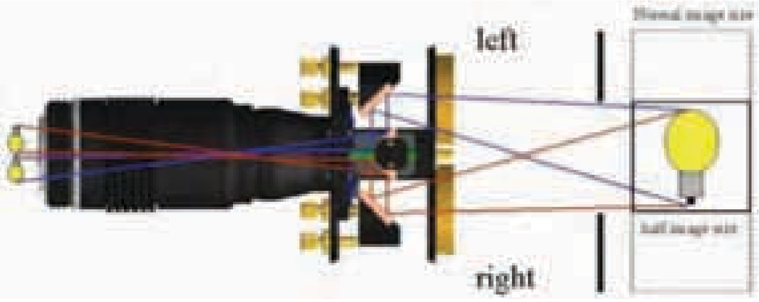

Figure 21: Working principle of LaVision's image doubler. The object can be seen on the right, the image is behind the lens on the left.

For the Mie camera (recording the Mie scattering signals), a 532±2 notch filter was used, which lets only pass the wavelength of the laser light (including the elastic Mie scattering at the same frequency). In addition, a set of Balzers Neutral Density filters with different transmission values was available.


Figure 22: A cup of Rhodamine 6G solution.

3.5.7 Scheimpflug-adaptor

For maximum light efficiency without the tradeoff of a blurry picture at the edges, a Scheimpflug-adaptor was mounted onto the LIF-Camera. It had to be adjusted by focusing on a calibration plate.

3.6 Fluorescent tracer

Rhodamine 6G was chosen because of its comparably low toxicity and a convenient excitation wavelength of 532 nm, which, in contrast to UV, is visible to the human eye and therefore safer. The safety advice can be found in the Appendix.

3.7 Measurement computer

For laser control and recording, a computer with a fast Intel i7 core2quad processor, a Matrox frame grabber card and a programmable timing unit was provided.

3.7.1 Programmable Timing Unit (PTU)

The PTU was the main unit controlling the measurements. Among its tasks were triggering the laser during experiments, adjusting the power of the flash lamps, adjusting the offset between the two laser units, synchronizing the camera acquisition with the laser emission and adjusting the camera exposure time.

3.7.2 Frame graber card

The frame grabber card received the images from the cameras. Therefore it had to be capable of handling high data rates.

3.7.3 DaVis software

DaVis is a program by LaVision, which enables the user to fully control laser emission and automatic or semiautomatic recording. During the experiments generally Davis 8.0 under Windows 7 was used. Since the Nanostar is an older model, the ICCD experiments were done using Davis 7.2 under Windows XP.

Processing the images had to be performed with the same program, because it is optimized for computing speed and exceeds general engineering tools as Matlab in performance.

The software does not require any programming skills. For special application it was of advantage to have some knowledge of LaVisions command language.

3.8 MiePlot

The behavior of Mie scattering at different angles of observation had to be calculated theoretically. Of particular interest was the dependency on the droplet size, especially for disperse sprays. The program MiePlot by Philip Laven (2011) can be found online (*http://www.philiplaven.com/mieplot.html*). It applies the Bohren and Huffman MIE algorithm.

3.9 Setup for LIF/Mie (geometrical configuration) ATMO test rig

3.9.1 2-Camera-Beamsplitter-Setup

The desired setup included a LIF-camera with a Scheimpflug-adaptor and a Mie camera. Also necessary was a beam splitter on a precisely adjustable mount with an anti reflection housing. A support on which everything can be mounted was also necessary. The beam splitter separated the light at a certain ratio. Part of the light passed straight through to the OG550 filter which was mounted on the LIF camera. The other part was reflected onto the Mie camera which was protected by a 2.2% neutral density filter from Balzers and a 532±2 notch filter. Since a beam splitter works in both directions, a light blocker was necessary in order to avoid additional light from other directions. The arrangement is shown in Figure 23. The support for a two-camera setup had to be exceptionally stiff in order to exclude any movement of the cameras towards each other. If the cameras position had moved after calibration, not only the coordinates were wrong, but more critically

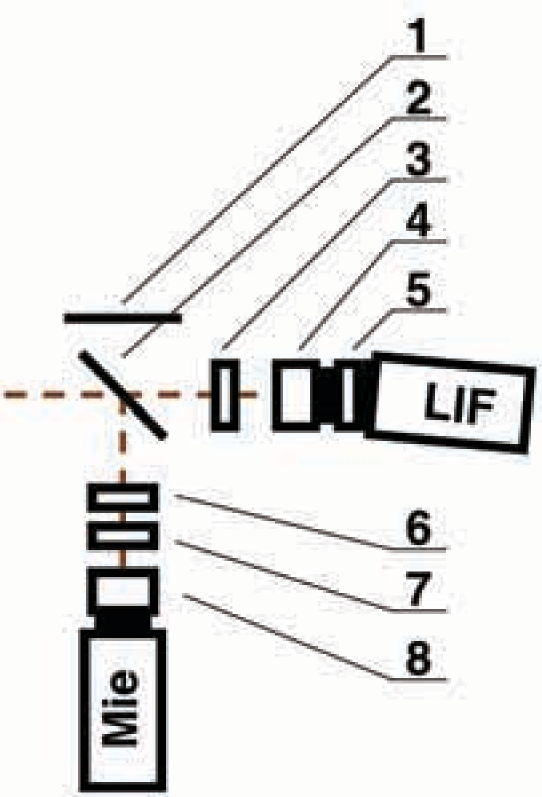

Figure 23: 2 camera setup with light blocker (1), beam splitter (2), long pass filter (3), objectives (4,8), Scheimpflug-adaptor (5), a neutral density filter (6) and a laser line band pass filter (7).

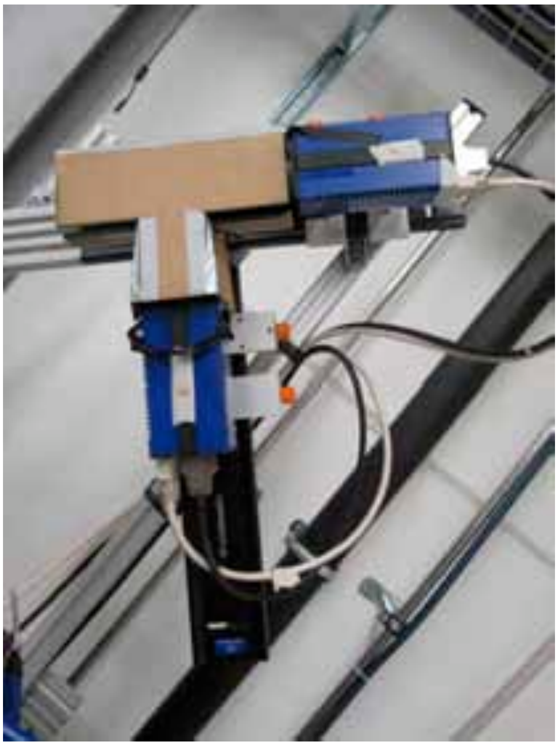

Figure 24: The T-bar with Camera 1 (LIF) and Camera 2 (Mie) in the anti reflection housing.

Figure 25: The opened anti-reflection box showing the beam splitter on a rotational mount and the two camera lenses. Camera one (top) had the Scheimpflug adaptor mounted. The rubber bands were necessary for provisional stabilization of the lenses.

the software divided wrong pixels of the LIF and the Mie camera, which introduced an error.

Another criterium was a flexible design. In order to change the angle of view later on or to quickly set it up at another test rig, the strut-construction was suitable.

By unbolting 3 screws the whole setup could be removed keeping the beamsplitter, it's housing, the cameras and the Scheimpflug-adaptor in position. Only the focus had to be adjusted to the new distance. To avoid reflection, the objectives and the beamsplitter were protected by a black coated housing. In a further step, stabilizers were used to reduce the lens clearance of the Nikon 1:1.8D objectives. The T-shaped support rested on a structure attached to the test rig, which again was designed for maximum stiffness.

3.9.2 ICCD-Setup

The Setup using an image doubler required fewer parts and was a lot simpler in general.

It consisted of an ICCD Camera and an objective connected to an image doubler, on which all filters were mounted. In contrast to the 2-camera setup, the LIF- and the Mie-signal had to pass through one objective. It was not possible to reduce the light discrepancy by changing the aperture. This was the reason, why another 1% Neutral Density filter had to be mounted in addition to the Balzers 2.2% filter. Furthermore

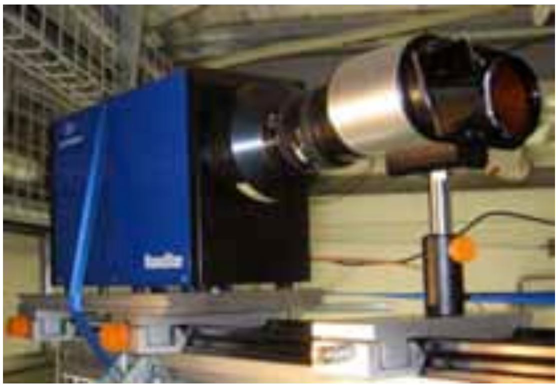

Figure 26: ICCD camera with objective and beamsplitter. On the far right, the long pass filter was mounted for extraction of the LIF signal, next to it, was the neutral density filter from Balzers.

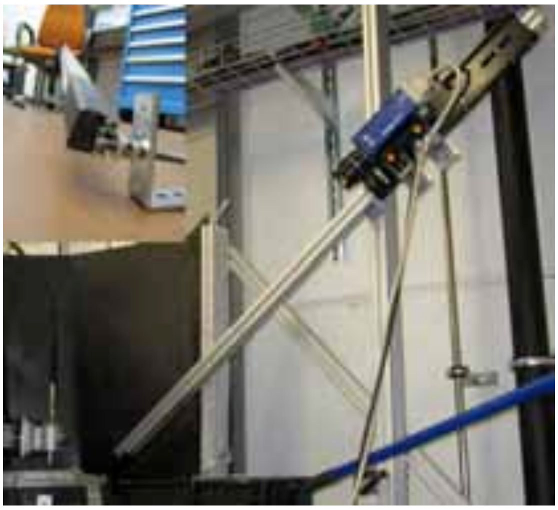

Figure 27: Setup for Mie Angle dependency experiments.

the Nanostar ICCD required a fiber optic connector for data transfer and therefore the frame grabber card had to be borrowed from the water lab as well.

3.10 Setup for Mie angle experiments

A different setup was chosen for the analysis of the Mie scattering. Only one camera was necessary and therefore, a light and flexible support had to be built. The experiments were carried out only once. That meant the setup did not have to be as sturdy as one made for daily measurement use. Several camera-positions had to be tested. Therefore one requirement was the capability of a fast change of angle. At the same time the setup had to be just stiff enough to guarantee, that the angle did not change anymore once it was adjusted.

4 Methods

4.1 D32 Calibration - Shadowgraphy

The LIF/MIE measurement system delivered only an intensity proportional to a droplet diameter with the proportionality factor *A* linking one intensity to a certain droplet diameter. The factor had to be determined for every setup, using an absolute measurement method. Therefore the droplet diameter had to be known in at least one position of the measurement plane. Once this diameter was linked to a signal at the same location, the diameter for the whole plane can be determined easily.

For that purpose a generator of monodisperse droplets could be used. As an alternative, the droplet diameter was measured in the actual spray. Phase Doppler anemometry or shadowgraphy are techniques capable of that. The later is simple and available in the Lab. Therefore it was our choice for calibration.

An earlier project, investigating the shadowgraphy system, was not completed by the end of this thesis (*Bensch 2012*). It will cover a detailed investigation of the individual parameters and their influence. For this thesis the parameters in Table 2 were used. The 'Image Validation' is a step introduced during the investigations, while the other ones were set by LaVision in the processing protocol.

Initially, the recorded images were evaluated. The average and the minimum value of each picture were calculated. Rejected were the ones where the difference between the minimum and average was below a defined threshold. If average and minimum were close together, the difference between them originated in noise and inhomogeneity of the laser diffusor and not a particle being present. Especially in sprays with low density, many images contained no particles at all. These images needed to be removed in order to improve accuracy of processing in the subsequent steps.

In contrast to conventional background processing, LaVision has developed an algorithm, which calculates the background rather than the user subtracting it manually. This algorithm works well as long as there are particles in the image.

As shown in **Figure 28**, the image is subtracted from the background and not the other way around. From now on, the particles are represented by the brightest spots in the image. In step 3 the actual particle is defined by a threshold related to the average. Then (4 and 5) the inner and outer diameter are set. The average of those is the diameter of the droplet as shown in **Figure 29**.

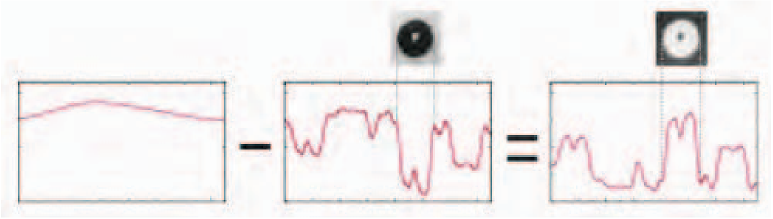

Figure 28: The raw image is subtracted from the background, which combines two steps: background subtraction and inversion.

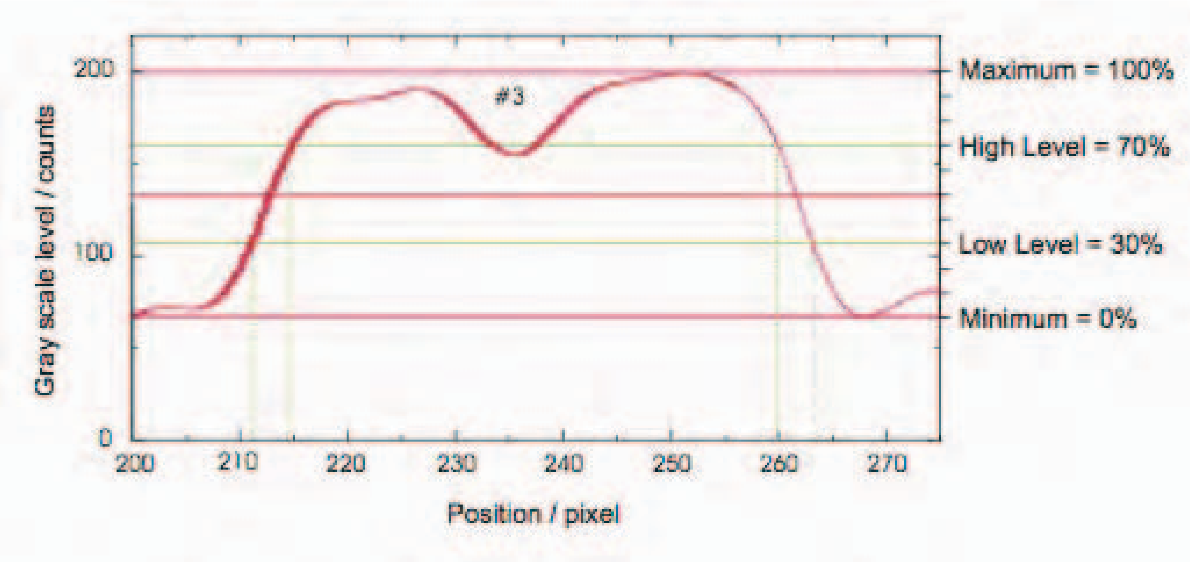

Figure 29: Intensity vs. position with maximum, minimum, and the thresholds: High and Low level just as the average diameter.

Whether a particle is in focus or not, can be recognized by its brightness but also by the appearance its borders. If they smoothen out into the background the particle is not in focus, we see it being blurry (**Figure 30**). If it has a steep-edge, it is very sharp. A droplet, which is not in focus, might have a different diameter than the picture suggests. Therefore only well focused particles are relevant. The more the particle smoothens out the bigger is the discrepancy between the low level areas (including dark areas) and the high level ones (only bright areas). This discrepancy is evaluated by step 6. If the low level area is more than twice as big as the high level area, the particle will be rejected. In the last step the centricity of the particle is checked. In our

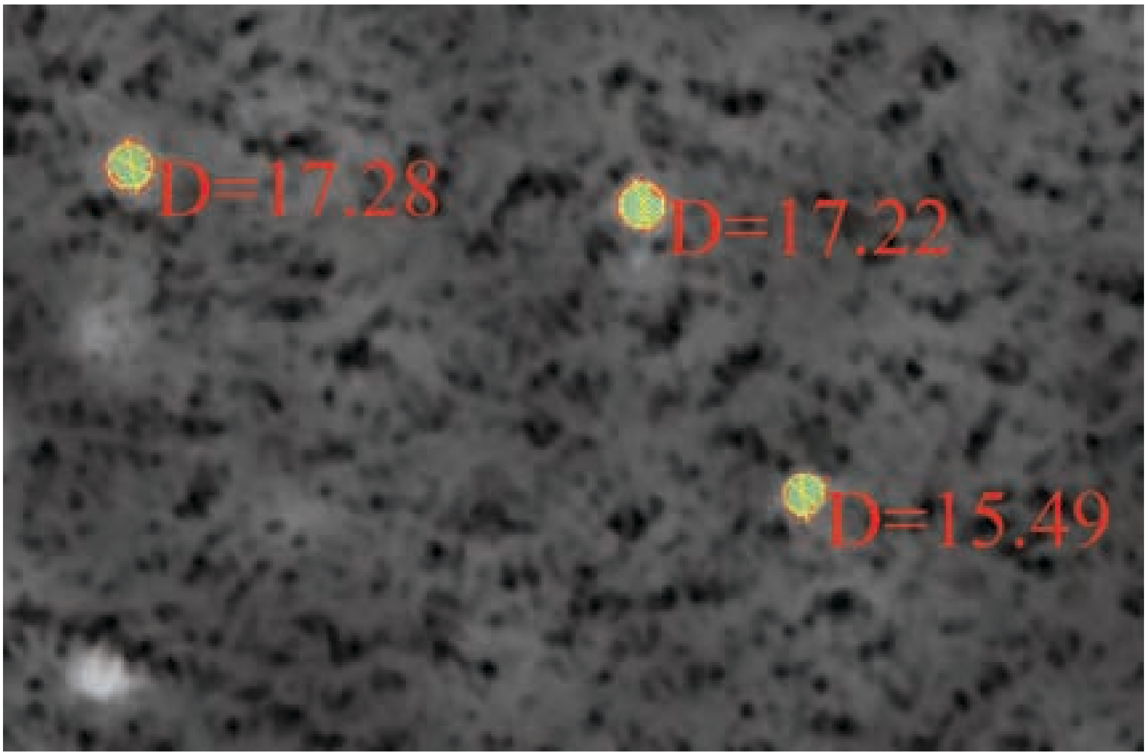

Figure 30: Snapshot of a Shadowgraphy result. Dark grey and black dots were due to the laser diffusor, the white peak in the lower left corner is a particle out of focus, not clear enough to be recognized by the prozessing.

case the smallest diameter had to be at least 50 percent of the biggest.

The complete list of parameters and their values can be found within the processing files provided on Compact Disc.

Depending on the spray parameters, a maximum of 2000 pictures was taken in order to have enough particles recognized for a reliable result.

Table 2: Processing steps of the Shadowgraphy system.

	Name	Value	Note
1.	Image Validation	40%	Rejects images which do not contain particles (highest allowed minimum as % of average)
2.	Background	Calculated	with strict sliding maximum
3.	Particle Recognition	72%	particle is at least x% of the brightest pixel in the image
4.	Low Intensity Level	55%	Defines the outer diameter
5.	High intensity Level	80%	Defines the inner diameter
6.	Maximum Low level Area	200%	Defines the maximum allowed ratio between inner and outer diameter
7.	Centricity	50%	Ratio between smallest and biggest diameter

4.2 Comparison of sizing systems with powder of known distribution

In order to compare two sizing systems like Spraymaster diffractometer and LaVision shadowgraphy, which have different measurement volumes, a disperse spray is not suitable. Diffractometry would always measure an average diameter across the spray while shadowgraphy can measure certain points in the spray. Therefore only a monodisperse spray guarantees that both systems measure the same particle diameter.

At the time of the experiments there was no monodisperse droplet generator available at the Spraylab in Birr. As an alternative, powder with known diameter was used. Particles with a guaranteed diameter are on the market, but they are extraordinary expensive. Therefore powder, which is used in ‘Particle Image Velocity’, was chosen. It was available in different diameters and reasonably cheap, but since the exact diameter of the particles is not of interest when measuring

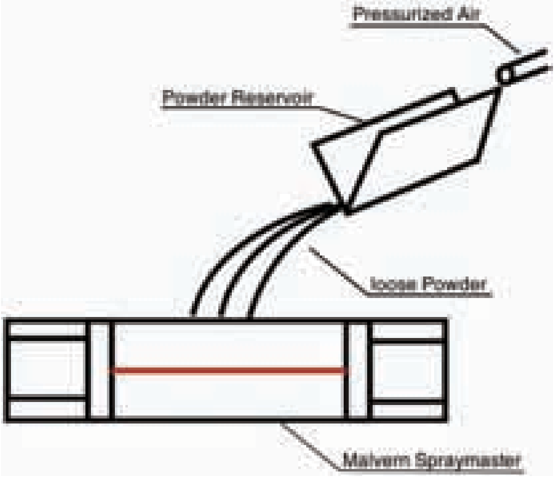

Figure 31: Arrangement for powder distribution. The powder reservoir is a folded sheet of paper.

with ‘Particle Image Velocity’, the manufacturer provided no distribution chart.

To have a third independent diameter, the powder was put under a microscope. The Zeiss Axioplan with an Epiplan-Neofluar 50x/0.75 HD lens had a total magnification of 0.63*50. The Axioplan was equipped with a Leica DFC 420 Camera and connected to a computer. Calibration enabled the user to take measure on the images. Diffraction at the particle’s edge and the fact that they were not round, limited the accuracy of this measurement method.

During the actual experiments with Malvern and Shadowgraphy, the most critical part of the setup was to guarantee that the powder does not stick together. Especially the 20µm particles were prone of agglomeration. Several attempts were made, until it was decided to blow the powder off a V-shaped reservoir using pressurized air, as shown in **Figure 31**. The particles then drizzled down into the measurement volume.

Measurements have been carried out with Dantecs Polyamide Seeding Particles (PSP). They are commonly used for Particle Image Velocimetry and available in the lab in 20µm and 50µm diameter.

4.3 Reduction of the mechanical play of the lens

The Nikon 1.8D lens is a consumer objective for single-lens-reflex cameras, and therefore had considerable play on the moving parts of the lens. Since it is mainly radial play, the picture quality for a photographer would not be affected. In a measurement situation though, it does matter whether the lens moves or not. The play might cause an image-shift, which was a problem with our special setup of two cameras. The operator could not rely on the pixel’s matching anymore, as only slightly touching the objective would move the image.

In order to quantify the influence of the mechanical play, the mounted OG550 Filter of the LIF Camera was pulled gently in four directions perpendicular to the optical axis. At each position several pictures of the calibration-plate were taken.

An unacceptably big shift of more than 10 pixels made a stabilization of the lenses necessary. Rubber bands were installed in order to pull the lenses in one direction as shown in (**Figure 25**). That way, a reduction of uncertainty to less than 4 pixels was achieved.

Further precision was not possible by means of hardware improvement. In order to match the images exactly, a processing step was introduced. After taking the recordings, a pair of LIF- and Mie-images was chosen, where an outstanding droplet was seen and the pixel-discrepancy between LIF and Mie could be counted. A macro, introduced into the processing, shifted the Mie image in a desired direction. Now the pictures were exactly matched before the LIF/Mie ratio was calculated.

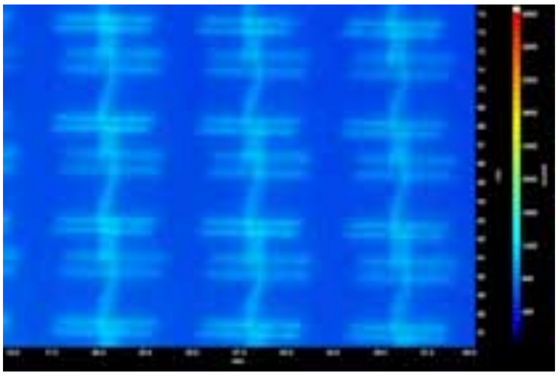

Figure 32: The DaVis snapshot shows an average of 4 records. The lens was always bent in another direction, and then released.

4.4 Mie scattering angle

Earlier investigations by *Charalampous and Hardalupas (2011 a & b)* have shown that the Mie signal was not always exactly proportional to d^2. This assumption was only valid in certain regions of scattering angles. The scientists investigated the angles of 60° to 120°. As these angles could not been used in the High Density Fluid Channel, an investigation of angles lower than 60° and higher than 120° was necessary.

Three parameters influencing the angle between laser sheet and camera axis have been identified:

- The physical accessibility in both test rigs must be given.
- The cameras angle of view caused a varying scattering angle along the x-axis of the image. Only slight angular deviation is therefore acceptable. Ideally, the proportionality factor should be constant for a scattering angle deviation of approximately ±5°.
- The correlation between signal (IMie) and droplet diameter (d) shown in equation **(14)** must be valid and should be as close to equation **(6)** as possible. Here aMie is the proportionality factor of the correlation and bMie is the power law factor.

$$I_{Mie} = a_{Mie} \cdot d^{b_{Mie}} \tag{14}$$

A setup was desired where the measurement sheet was perpendicular to the nozzle-axis, with an angle of 90° between the laser sheet and the camera would have been perfect because of smallest possible distortions. This was not possible though, since the camera and the nozzle would be at the same position, or the droplets would splash onto the camera. As shown in **Figure 33**, this left the area around 45° forward scattering and the area around 135° backscattering for the ATMO-RIG and an angle between 15° and 45° or between 135° and 165° for the High Density Fluid Channel.

Regarding the angular dependency, the slope of the curve must not be steep for two reasons. Firstly, when the system was taken down and set up again, the exact same angle between laser sheet and camera could not be guaranteed, therefore a difference in angle should not alter the results too much, otherwise the reproducibility of the measurement could not be given. Secondly the camera had an angle of view, which caused a changing scattering angle along the image in the region of roughly ±5° from the optical axis of the camera. If there was a big change in intensity along these 10°, the same droplet would reflect a different amount of light

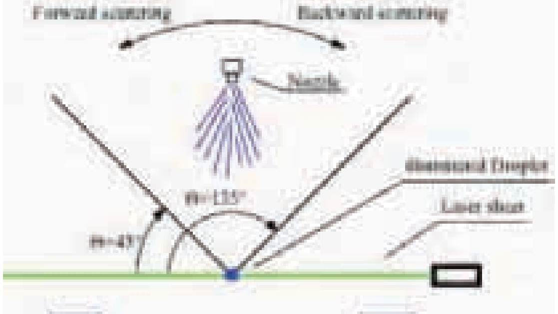

Figure 33: Visualization of the scattering angle at the example of the ATMO test rig .

depending on where it was located on the measurement plane. Since the LIF-signal had no angular dependency, this would alter the intensity ratio and therefore result in a different droplet size.

The problem was approached in two ways, a theoretical one, which was then proven by experiments.

4.4.1 Mie camera with different scattering angles

A camera with aperture 22 was equipped with a 532nm notch- and a 2.2% neutral density filter. Backscattering of theta = 120° (close to the nozzle) up to 165° (just above the laser head) was recorded (**Figure 33**). The average of 200 images was calculated and a previously taken background was subtracted. The total counts of the whole picture were plotted for nozzles Le1 and Mee with their individual standard parameters. After recording the different angles, 200 pictures were averaged, the background was subtracted and then the number of total counts in the image was compared with the theory.

4.4.2 Theoretical calculation

For calculation of the intensity as a function of scattering angle and droplet size, the program ‘MiePlot’ was used. Two different calculations were carried out:

- The intensity over the scattering angle, for a set diameter.

The calculation included a normal distribution of the set droplet diameter in order to make the calculation comparable to the measurements.

- The intensity over the droplet diameter, for the individual scattering angles. The calculation was performed for the region of 10µm up to 100µm with an increment of 0.01. In a further step, a 2nd order polynomic trendline ($I_{Mie}=a_{Mie}*d\hat{}b_{Mie}$) was calculated, using the least square method. The value b of the trend line should be as close to two as possible.

4.5 LIF/Mie measurement preparation

4.5.1 Background – Parameters of Influence

The dark image represents the chip noise (e.g. thermal noise or shot noise). The background is defined as the dark image and external noise, such as ambient light reflected by parts in the measurement plane. It must be subtracted from the records before any further processing was done.

Two variables were investigated:

- The difference between the dark image and the background image.
- The influence of the number of images averaged.

The cameras were setup the same way as they were at the main experiments. A 2.2% neutral density filter and a 532-notch filter were mounted on the Mie camera with aperture 22, while the LIF camera Had an OG550 long pass filter and an aperture set to 1.8. Since the laser pulse was very short, an exposure time of only 50 µs was set. This should have avoided any influence of the ambient light. For taking the dark image, simply the lens cap was put on the objective. The background was taken, while the main laboratory lighting was off, but a low ambient light was on.

Two different configurations for the background image have been tested. Firstly the water supply nozzle was turned on but the laser is off and secondly (the classical background) with the spray off but the laser on.

4.5.2 Generation of an evenly illuminated white sheet

To guarantee equal signal recognition by the camera over the chip area, LaVision suggested a white-sheet correction. The so-called vignetting was recorded by evenly illuminating a white sheet placed into the measurement plane, ideally out of focus. The effect causes a decrease in intensity radially outwards. Two different approaches have been performed in order to generate a white sheet:

Spotlight

A Spotlight was placed behind a paper screen, illuminating a white sheet also made of paper and positioned 100mm out of measurement area. Since there was an obvious influence of direct reflection, the setup was improved by using a guide rail to

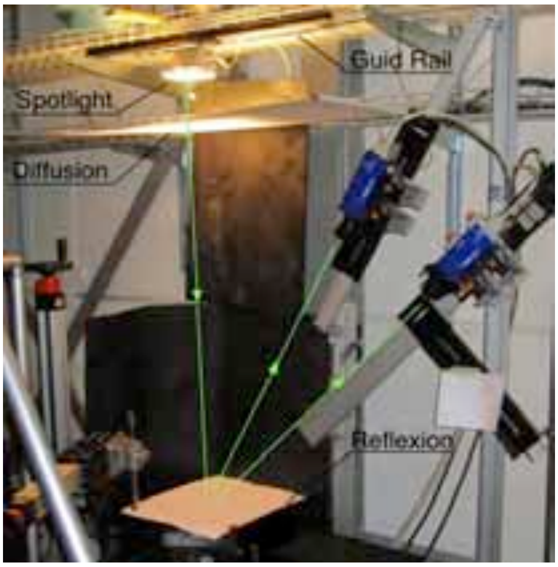

Figure 34: The initial white sheet setup with a spotlight.

Figure 35: The generation of the white sheet with a computer screen. The LIF camera had the Scheimpflug adaptor mounted.

Table 3: Processing steps of the white sheet image.

Function	Value
Remove Particle Size	3 pixels
Smoothening	5x5 pixels
Relative Threshold	40% of Average

move the Spotlight across the measurement area. Every 20mm an image was taken and all of them were averaged. This procedure was more accurate, but only moving in y-direction as well would have avoided any influence of reflection. Such a setup would be very time consuming and not be practical for a mature measurement-technique in daily use. Therefore another approach was taken.

Computer screen

The new setup included a computer screen at close range with an empty PowerPoint slide open as set up in **Figure 35**. In this case, all pixels were white. This represented a quick setup with reproducible results. It was still slightly dependent on the angle, which was explained by the computer screen, throwing the light mainly perpendicular to the screen. Best results were achieved, by positioning one screen in front of each camera. The exposure time was adjusted in order to have a maximum of approximately 10,000 count.

The white image had to be recorded for both cameras and all 8 apertures. That made 64 possible combinations. In order to reduce the amount of records required, the same aperture was set on both cameras. The desired combination of frames had to be stitched together with a macro. Its code can be found in the Appendix.

Before the white sheet was ready to use, some treatments needed to be set. Particles smaller than 3 pixels had to be removed, a filter had to be applied which smoothened the image and finally a relative threshold had to be defined. Pixels lower than that were set to the thresholds value. The values of the individual steps can be found in Table 3.

4.5.3 Geometrical Calibration – Distortion

Rectification was generally necessary when measuring. In particular at the setup with 45° between the measuring plane and the camera, the raw image was strongly distorted. It needed a clean geometrical correction. The second and even more important reason for the calibration was the matching of both cameras. Since LaVisions Spraymaster LIF divides pixels, it was critically important that the software recognized, which pixel of each camera represented the same droplet. This was achieved by putting a calibration plate with crosses or a dotts into the measurement plane. Three plates were tested, their specifications can be found in Table 4.

Table 4: Different Calibration plates.

Type	Cross length / mm	Center distance / mm	Material
2d Crosses	6	8	A4 paper print
2d Crosses	5.5	8	Black anodized aluminum
3d Crosses	5.5	12	Black anodized aluminum

In a first step, the characteristic values of the used calibration plate had to be set in the programs dialog. Then a picture was taken (Figure 36) and the user had to define three crosses on both camera images, which represented the same crosses on the calibration plate. DaVis software found the other crosses automatically (Figure 37), provided that the plate was well focused and illuminated. It then calculated the straightened image (Figure 38) and even told the cameras position including angle and distance, just as the focal length of the objective (**Figure 39**). The value “Average Deviation to marks (in Pixels)” represented the quality of the form-fit-function, calculated by DaVis. According to LaVision, it had to be below 2, should be below one but is ideally below 0.3. During the tests it was not possible to push the value below 0.7. Different light settings, changing the aperture or changing the calibration-plate to a volume model did not alter this value. While the aluminum 2D and 3D plates produced an “Average deviation to marks” value between 0.7 and 1, the A4-paper print proved to be quite inaccurate with a value of 3. A reason for that might be the fact that the paper was not perfectly even.

Making sure that the calibration plate matched the camera image increased the quality of the fit-function slightly. When the plate was bigger than the image, the number of viewed crosses was reduced, when the plate was considerably smaller, the area around had to be extrapolated. The matching was achieved by changing the plate-camera distance.

The calibration took place without any filters, because otherwise the black anodized aluminum plate would not have been illuminated enough.

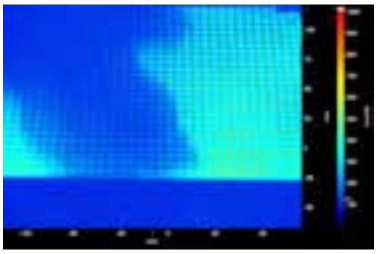

Figure 36: The raw image of the calibration plate visible through camera one’s focus. Obvious is the shadow of the nozzle holder, coming in from the top left corner.

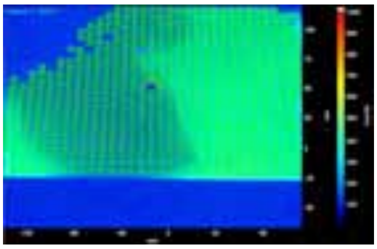

Figure 37: The first step consists of the automatic recognition of the crosses. As one can see, the combination of shade and the top left corner being slightly out of focus, lets the recognition fail in this area

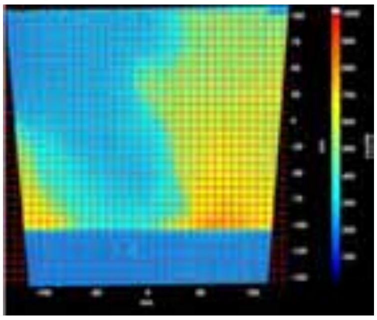

Figure 38: After rectification, the measurement plane turns out to be a lot wider in x-direction than initially thought.

4.5.4 Droplet sizing calibration

The most critical part of this planar droplet sizing system was the droplet calibration, because of its great contribution to the final result. This step could only be carried out, once an image of the light intensity ratios existed. That meant, the recordings have had taken place already and for at least one measurement, the processing described in Table 6 has been carried out until step 6 (‘Droplet Sizing’).

Table 5: The calibration coefficients A for the different diameter regions.

Nozzle Type	Valid for Measurement Number	SMD (µm)	Calibration	I_ratio (counts)	A (counts/µm)
Mee	All	15	Shadowgraphy	122.5	8.17
Mee for ICCD	All	15	Shadowgraphy	148.7	9.91
Le1 for ICCD	All	95.5	Diffractometry	631.8	6.62
Le1	243-252	95.5	Diffractometry	270.8	2.84
Le1	268-281	95.5	Diffractometry	409.5	4.29
Le2	All	168	Diffractometry	2681.76	15.9

The second requirement was, that the droplet diameter in at least one position and spray condition was known.

$$A = \frac{I_{ratio}}{SMD} \qquad \textbf{(15)}$$

The idea was to take the light intensity ratio of a certain position in the spray and link it with a droplet diameter measured at the same location by Shadowgraphy or a different point-measurement-technique. It was then assumed, that a droplet diameter of 0 corresponds to a light ratio of 0 counts. This assumption was necessary because the used version of DaVis was not capable of any other calibration curve than the linear one. Further more it automatically set the first point for the curve to 0 counts = 0 µm. In Table 5 the absolute values of droplet diameters for the individual nozzles in their standard conditions are listed. The corresponding intensity ratio measured with LIF/Mie can be found as well. Every nozzle's spray was calibrated individually at their

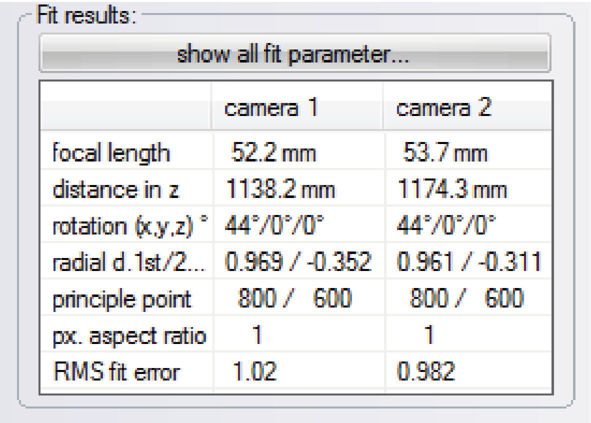

	camera 1	camera 2
focal length	52.2 mm	53.7 mm
distance in z	1138.2 mm	1174.3 mm
rotation (x,y,z) °	44°/0°/0°	44°/0°/0°
radial d.1st/2...	0.969 / -0.352	0.961 / -0.311
principle point	800 / 600	800 / 600
px. aspect ratio	1	1
RMS fit error	1.02	0.982

Figure 39: DaVis showed the calculated position of the Cameras and the quality of the form fit function (RMS fit error). In reality, the focal length was 52 mm and the angle was 45°. The distance should have been 1150 mm. One can see that DaVis was not as accurate with camera 2's values. The beam splitter reflected the light on this one, while camera one got the transmitted light information.

standard condition. This was necessary, because the sizing parameter *A* defined in equation **(15)** proved not to be constant over a wide range of diameters.

Calculation of *A* by dividing the averaged Intensity ratio I_{ratio} by the previously acquired Sauter mean diameter (*SMD*) completed the calibration. Since it was not possible to position the nozzle exactly the same as it was positioned during the Shadowgraphy and diffractometry tests, it was decided to take an average of a square of 10mm by 10mm for the I_{ratio} when calibrating with Shadowgraphy. For diffractometry a vertical rectangle was taken which was 10mm wide and as long as the spray.

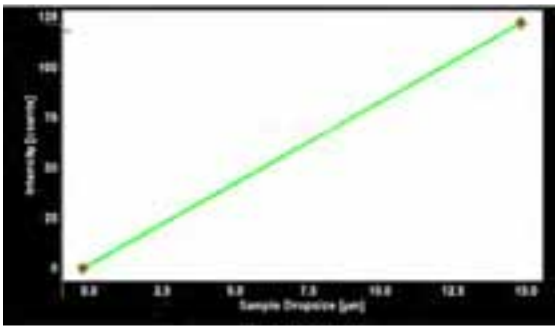

Figure 40: The Calibration curve for droplet sizing.

Table 6: Processing steps of the LIF/Mie system.

Ste	Name	Description
1	Averaging	Averages the raw images
2	Backgound	Subtraction of the back round
3	Whitesheet	Standardization, using the white sheet
4	Geometrical Calibration	Rectification of the image
5	Pixel Sliding (not suggested by LaVision)	Shifts the images against each other
6	Droplet sizing	Division of the signals
7	Diameter size calculation	Allocates a diameter to the intensity

4.6 LIF/Mie post processing

The processing steps in Table 6 were suggested by LaVision. They were applied to the raw images in order to gain a specific diameter at a given location. For both, the LIF- and the Mie-Images a total of 200 pictures were averaged.

Then the previously recorded background was subtracted and a white sheet correction was applied according to equation **(16)**. The correction compensated for the CCD chips weaker sensibility at the corners. In order to get the new Intensity at a certain location ($I_{new(x,y)}$), the intensity at this pixel ($I_{old(x,y)}$) was multiplied by the white sheets average intensity $I_{sheet\_average}$ and divided by the intensity of the white sheet at the same pixel ($I_{sheet(x,y)}$). The acquisition of background and white sheet are described in Chapter 4.5.1 and 4.5.2.

$$I_{new(x,y)} = W \times I_{old(x,y)} = \frac{I_{sheet\ average}}{I_{sheet(x,y)}} \times I_{old(x,y)} \tag{16}$$

The ‘Geometrical Calibration’ step rectified the images of both cameras and fitted them, so the individual pixels actually represented the same physical location. This step used the previously acquired calibration-set as described in Chapter 4.5.3.

Step number 5 was not suggested by LaVision, but it was necessary, due to our 2-camera setup and its problematic mechanical play of the lens. After the image distortion was corrected they were exactly matched. This step was iterative and not automated. After a first test processing, the user had to find a droplet, which could be clearly localized on both images. Then he had to look how far the sheets were off, and change the macro so they would match. Once they match, he had to perform the processing for the entire set of recordings, given that the lens system was not touched or dislocated by severe vibration. The typical rig vibrations during the tests were not strong enough to alter the lenses adjustments.

If in doubt, the user could easily check whether the lenses were still in position, and if necessary readjust the images.

Once the images were in the correct position, the intensity ratios $I_{ratio(x,y)}$ were determined for each pixel by dividing the LIF signal $I_{LIF(x,y)}$ by the Mie signal $I_{Mie(x,y)}$ using equation **(17)**. The constant *k* was necessary because the Mie signal was a lot stronger than the LIF signal. During the experiments it had to be kept constant. For all measurements it was set to 1000.

$$I_{ratio(x,y)} = \frac{I_{Lif(x,y)}}{I_{Mie(x,y)}} \times k \tag{17}$$

Finally the actual diameter calculation took place (equation **(18)**). Every intensity ratio $I_{ratio(x,y)}$ was linked to a diameter d_{32} with the calibration coefficient *A* from Table 5. This was performed pixel by pixel.

$$d_{32(x,y)} = \frac{1}{A} \times I_{ratio(x,y)} \tag{18}$$

The complete processing for one pixel is shown in equation **(19)**.

$$\frac{\left[\left(\frac{1}{n} \times \sum_{n=1}^{200} I_{Lif(x,y)}\right) - I_{background(x,y)}\right] \times \frac{I_{sheet\,average}}{I_{sheet(x,y)}}}{\left[\left(\frac{1}{n} \times \sum_{n=1}^{200} I_{Mie(x,y)}\right) - I_{background(x,y)}\right] \times \frac{I_{sheet\,average}}{I_{sheet(x,y)}}} \times k \times \frac{1}{A} = d_{32(x,y)} \tag{19}$$

4.7 Measurement positions

Table 7 presents the standard conditions, defined at the beginning of our measurements. Nozzles Le1 and Le2 were delivered with a measurement protocol for those conditions.

Table 7: Standard conditions for the three nozzles used.

Nozzle	p /mbar	z / mm	y / mm	Note
Mee	138 00	50	0	Arch parallel to y axis, coming from negative y
Le1	4500	500	0	Flat cone parallel to y axis
Le2	3500	150	0	Flat cone parallel to y axis

The Mee nozzle was investigated in more detail at the given conditions by *Chacar et al. (2002)*. The orientation of the Lechler nozzles was defined because of expected expected during the measurements, while the Mee nozzle's position was defined for repeatability. There was no obvious advantage of that certain position, only the spray was not perfectly symmetrical and therefore it had to be defined somehow.

Table 8: Positions, measured with Shadowgraphy. The Δy*-column was recorded in y-direction but with the Mee nozzle rotated by 90°.

Nozzle	Measurement Numbers				
	Δp	Δz	Δy	Δy*	Δφ
Mee	-	-	70-78	79-89	-
Le1	-	52-58	43-51	-	-
Le2	-	-	-	-	-

Table 8 and Table 9 present an overview of the measurements carried out with Shadowgraphy and Diffractometry. Not all parameter variations were available for both systems. Generally, pressure variation Δp, axial distance variation Δz and radial distance variation Δ y have been investigated. Rotating the nozzle (Δφ) was only carried out for the combination of the Diffractometry system and the asymmetric spray-cone of the Mee nozzle.

Table 9: Measurement positions with Diffractometry. The Δy*-column was recorded in y-direction but with the Mee nozzle rotated by 90°. *[1]) Le1 pressure dependency was measured at the standard condition z=500 but also at z=100.

Nozzle	Measurement Numbers				
	Δp	Δz	Δy	Δy*	Δφ
Mee	337-340	-	90-100	101-111	112-117
Le1	341-352*[1]	145-1 0	134 144	-	-
Le2	-	-	120-133	-	-

LIF/Mie measurements did not feature Δy and Δφ variation. This was not necessary because of its planar measurement character. Therefore two more nozzles were added to the list (OP-P12, OP37). Both were combustor pilot oil nozzles with different flow rates.

Table 10: Measurement positions with LIF/Mee in 2-camera setup and ICCD setup. *1) Le1 pressure dependency was measured at the standard condition z=500mm but also at z=100mm.*2) The ICCD measurement of Le1's pressure dependency has only been recorded at z=100mm, which is not the standard condition of the nozzle.

Nozzle	Measurement Numbers			
	2-Camera Setup		ICCD Setup	
	Δp	Δz	Δp	Δz
Mee	253-256	282-295	317-320	320-325
Le1	267-271 276-281*1	271-276	330-335*2	326-330
Le2	-	257-266	-	-
OP-P12	304-308	309-313	-	-
OP37	298-303	-	-	-

5 Design of hardware

5.1 Sheet optics support

The existing laser head consisted of a cylindrical concave lens and a standard convex lens. When the distance between them was altered, it was possible to align the sheet thickness.

Since the sheet had to hit the beam trap at the other side of the channel, fine adjustment had to be possible. Also for security reasons, the single holder originally supplied was insufficient. It was improved by adding a three-point support behind the optics, which was on a horizontal track and securely held the laser head in position. The custom-built support was capable of slight rotation around the y- and the z-axis. This fine adjustment made it possible to point the laser sheet directly into the beam trap on the opposite side of the channel.

5.2 Beam traps

5.2.1 Warm-up beam trap

During warm-up (prior to measurements) the laser had to be fired at high power. To guaranty laser safety during that period, a special warm-up-beam trap was designed. It was screwed on the laser head instead of the cylindrical lens and blocked any light emission. For increased heat transfer it featured cooling fins on the back.
Using this device, lab time had been reduced. The laseralready warmed up while final adjustments at the rig were made without the need of laser safety goggles.

5.2.2 Sheet cleaning beam trap

Due to the design of the laser head with a convex lens, the laser sheet it self was not perfectly parallel, and some light scattering was observed. Therefore a beam trap was designed and mounted just after the laser head. It left a horizontal adjustable gap for the sheet. It fitted on the optical rail system from Edmund optics, where the laser head was mounted.

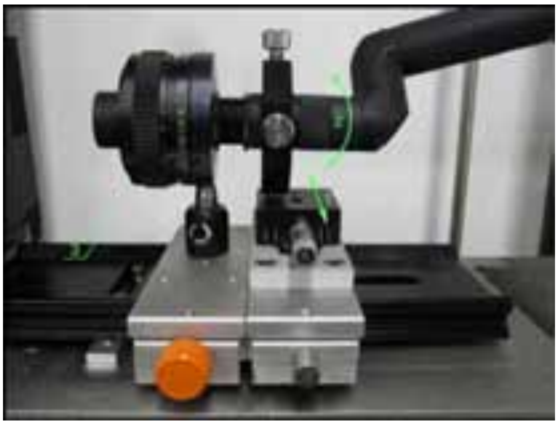

Figure 41: Sheet optics (3) with its support, including the rotational adjustment-possibilities around the z-axis (1), and around the y-axis (2).

Figure 42: The warm-up beam trap with cooling fins. When both lasers run on full power, the temperature of the device was only slightly above room temperature.

Figure 43: The sheet cleaning beam trap seen from the backside. By loosening the four wing nuts the gap for the laser beam was reduced. The gates were bent towards the laser beam to avoid any double reflection.

Figure 44: The anti-reflection beam trap with 2 slots for flexible mounting.

5.2.3 Anti-reflection beam trap

Laser light, which was not absorbed or scattered by the droplets, hit the wall at the opposite side of the test rig and was uncontrollably reflected. On the one hand this was a safety problem, on the other hand it possibly influenced the results. To avoid unnecessary scattering, a beam trap was designed for the end of the measurement section, in order to trap all light not scattered by the spray. It was curved in order to blend into the rig, reducing aerodynamic influence on the spray to a minimum. The top was sloped to avoid water accumulation and the bottom was kept shorter to guarantee, that no droplet could find its way into the beam trap. There, big droplets would work as an optical lens or mirror and could influence the measurements.

6 Results

6.1 Comparison of sizing systems using powder with known size distribution

As shown in Figure 45, shadowgraphy and the Malvern diffraction system were very close to each other when characterizing the 20µm powder. Shadwography is slightly more precise, but the Diffractometry system is also in the range of typical droplet diameter measurements.

Characterization of the 50µm powder on the other side showed a clear difference between the two systems of about 10% of the expected diameter. The fact that Shadwography is measuring a smaller diameter, goes along with the experience gained during measurements of actual nozzles.

The microscope experiments showed a constant error of about 1.3 µm. It seemed not to be diameter dependent.

As seen in Figure 46, the particles are not perfect spheres. The circles are put on top by hand therefore accuracy is limited. Furthermore diffraction of the light makes it hard to detect the actual edge.

The microscope experiments should only be seen as a way of getting an idea of the size and investigating the shape of the particles. They are not suitable for any kind of calibration.

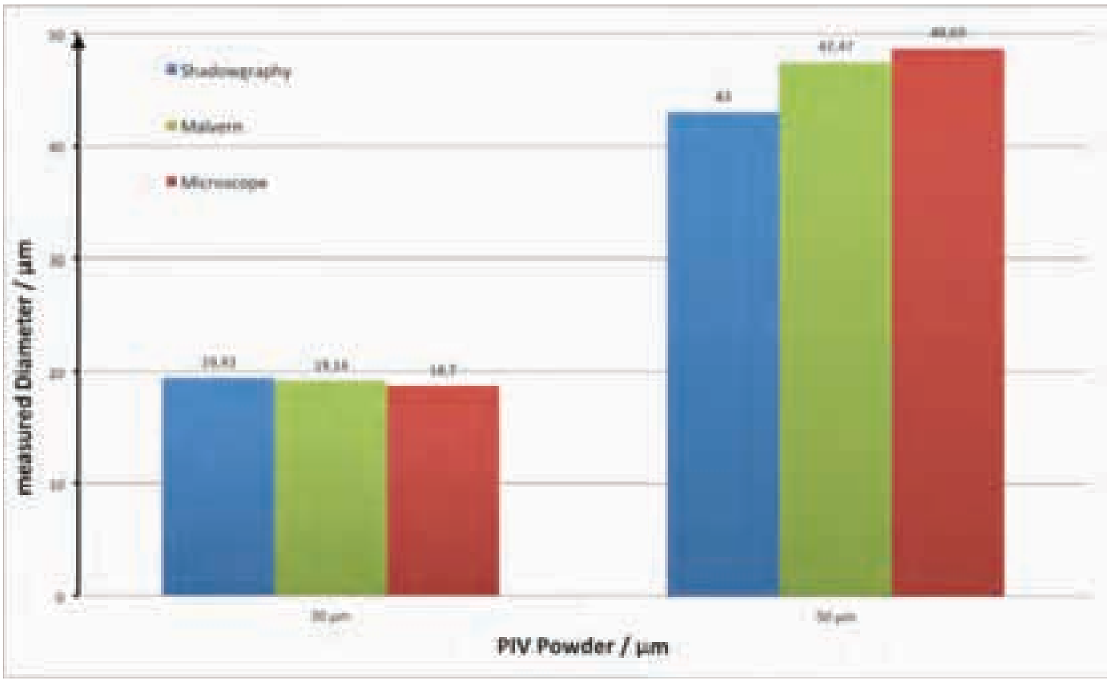

Figure 45: Measured diameters of two samples with 20µm and 50µm seeding particles, when comparing three different measurement thecniques for particle sizing. Namely microscope observation, diffcartion and shadowgraphy.

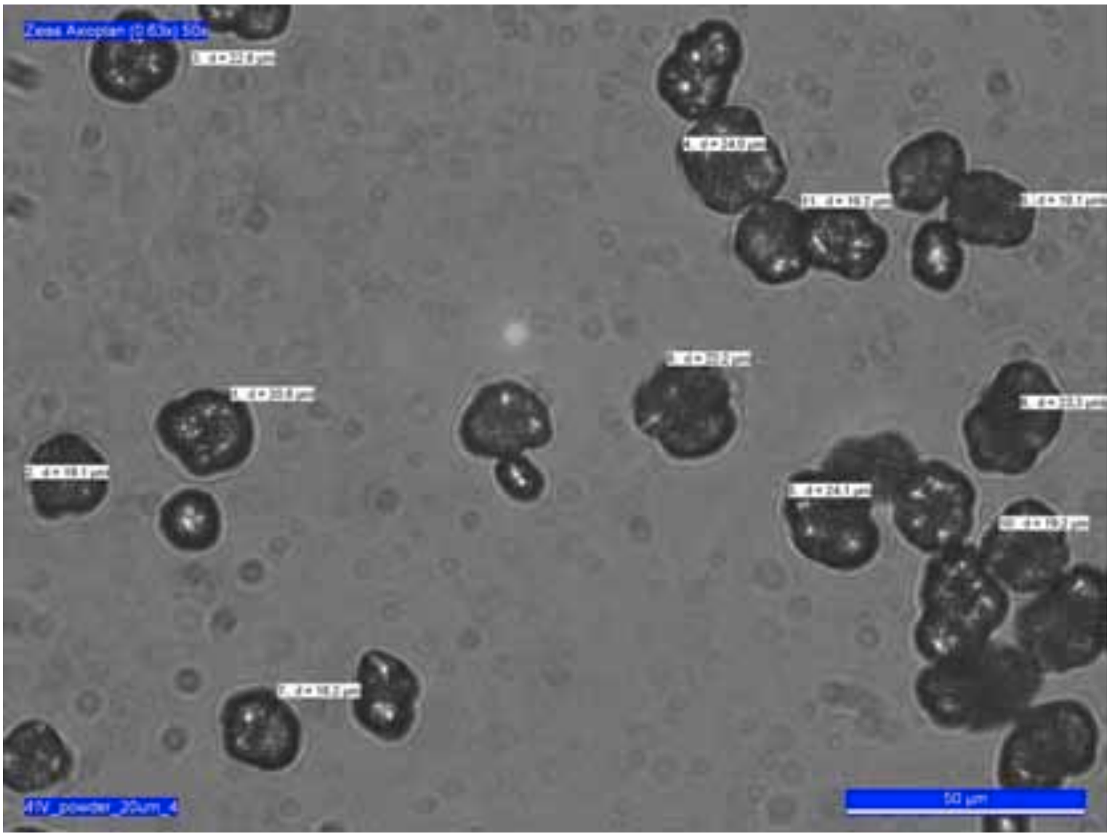

Figure 46: 20µm particles under the microscope, with manually added circles for diameter evaluation.

Furthermore, they show that most particles are not spherical. This is a problem as droplet sizing by LIF/Mie is based on the assumption of spherical particles. Since the induced error is unknown and would need its own investigation, the results are not as reliable as using a monodisperse droplet generator. Only this device can guarantee comparability between a point-measurement-technique and a volume-integrative system.

6.2 Mie-Scattering – Theoretical calculation and experimental validation

6.2.1 Different Scattering Angles

Mie scattering was recorded according to the setup, described in Chapter 3.10. The experiments for 120° to 165° match the theory very well. The graphs in Figure 47 and Figure 48, show that the theory matches our experimental results very well for the Mee and the Le1 nozzle. They prove that our setup with a finite solid angle and a disperse spray provides the same trend as the theory. The heavy oscillations of the Le1's calculation cannot be resolved experimentally. This is due to the averaging character of both the camera's finite solid angle and a disperse spray.

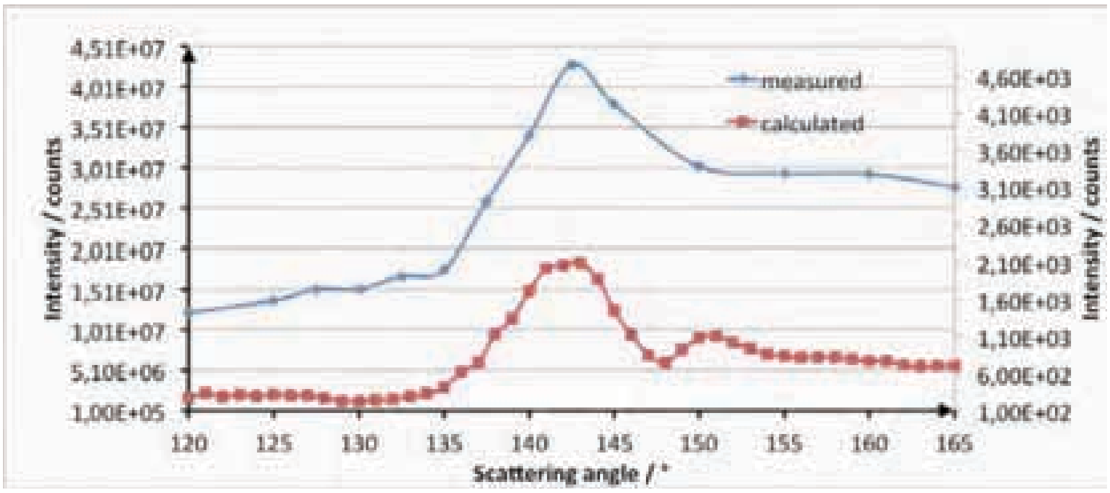

Figure 47: Mee nozzle: Comparison of measured and calculated Mie intensity along the backward scattering angles of 120° to 165°. The calculation was set for 18µm using a log normal distribution with a standard deviation of 10%

The graphs can only be compared qualitatively because of many parameters influencing the intensity. Those parameters are in particular the laser power, the aperture of the objective or the quantum efficiency of the camera.

Matching of the theoretical and experimental results in the backscattering region, gives confidence in the theoretical results. Therefore the forward scattering was theoretically investigated only.

Figure 49 shows that the region around 90° scattering angle would be the best region for measurements in terms of angular dependency, because the slope of the curve is almost flat. The region of backscattering is very disadvantageous in terms of continuity. For example, in the region around 135° the 100µm particle scatters with about the same intensity as the 15 µm particle does at around 140°, although

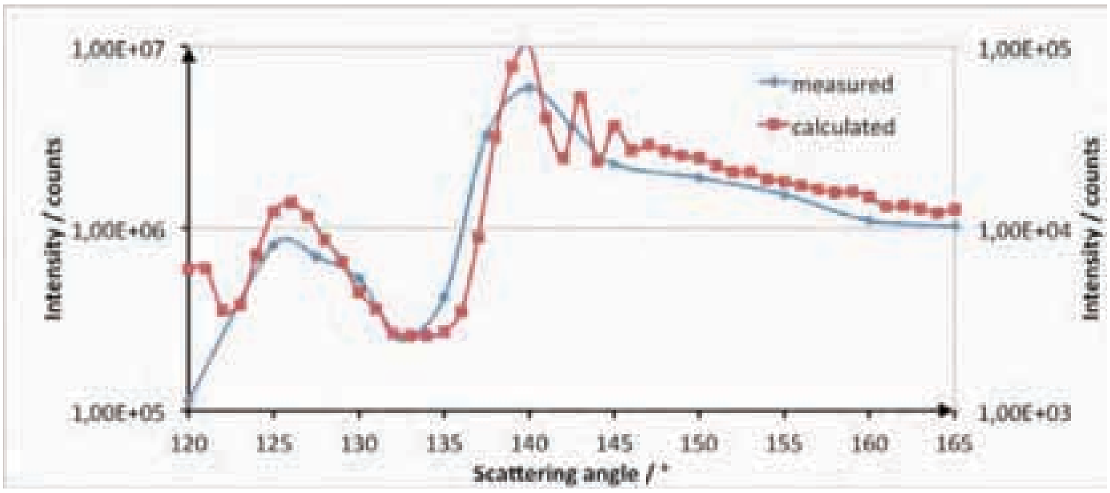

Figure 48: Le1 nozzle in a logarithmic graph: Comparison of measured and calculated Mie Intensity along the backward scattering angles of 120° to 165°. The calculation was set for 95µm using a log normal distribution with a standard deviation of 10%

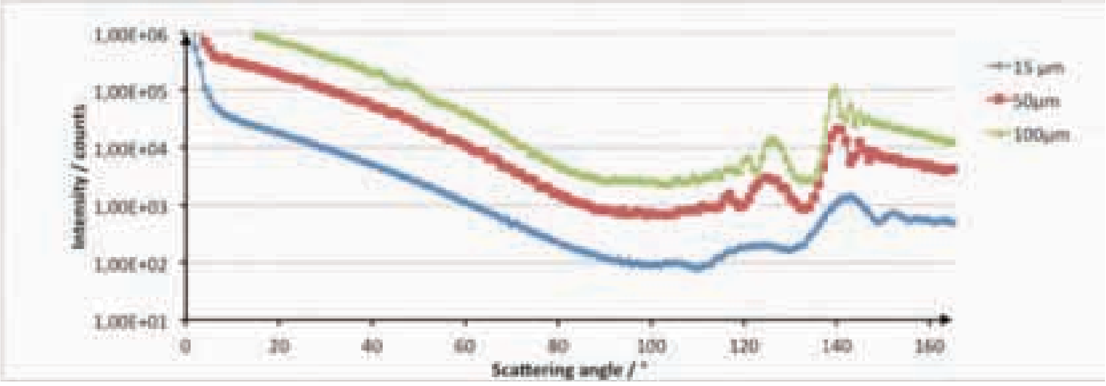

Figure 49: A comparison between different diameter's scattering behavior in the region from 0° to 165°.

according to the LIF/Mie theory, their scattered light should be proportional to d^2.

That leaves the region around 45° forward scattering, where the curve is not flat but still very smooth.

6.2.2 Different Droplet sizes

The second investigated parameter was b_{Mie}, the exponent of the power law, describing the relation of Mie intensity and droplet size. While the parameter is expected to be 2 (equation **(6)**), it turned out that this is not perfectly correct as shown in Figure 50. Deviation from 2 can be seen. It varies with the scattering angle.

The software Mieplot calculated the diameter dependency theoretically, producing a chart. The results had to be transferred to Microsoft excel, and a trend line was calculated, using a power-law. The equation was fitted with a least square method. Figure 50 shows the calculation of the parameter for a scattering angle of 45° and a diameter range of 10µm to 180µm. b_{Mie} in this case is 1.9841. The individual calculation points are not visible anymore because of the very small increments of diameters calculated. Never the less, the figure shows that the oscillations around

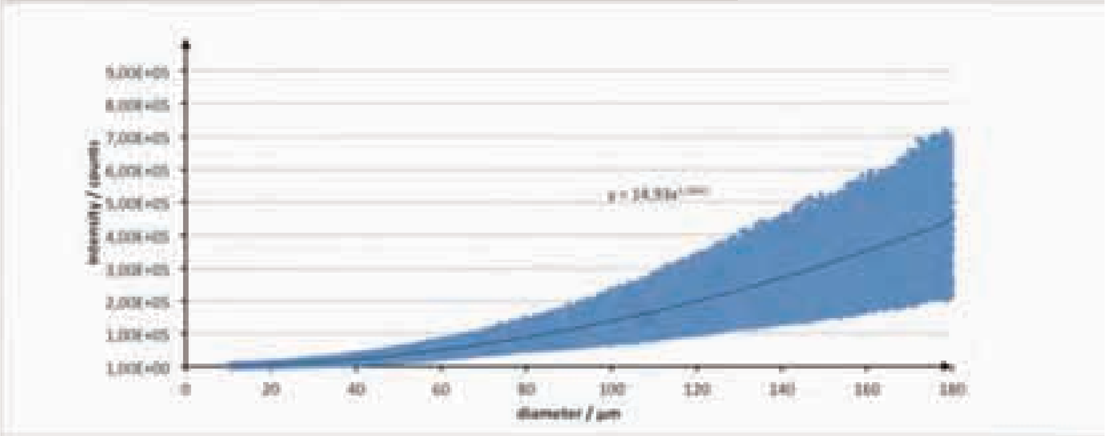

Figure 50: The scattering intensity as a function of the diameter d for an angle of 45° forward scattering. The calculation was carried out with a 0.02 µm increment. The resulting 8600 calculation points make the graph appear rather crowded. The trend line is $y= 14.93*x^{1.9841}$.

the trend line strongly increase with larger diameters. This makes averaging over several images necessary.

The same procedure has been carried out for other angles as well. The parameter b_{Mie} calculated for the specified angles is presented in Table 11. The assumption of surface proportional intensity seems to be good in the region around 45° the lower the better, until at very low angles, b_{Mie} rapidly increases to almost 4. High values of backscattering are not useful for measurements either. For meeting the objective the values of b_{Mie} must be as close to 2 as possible.

Table 11: The parameter b_{Mie} as a function of the scattering angle γ, calculated with Mieplot.

γ / °	0	15	30	40	42,5	45	47,5	50	120	140
b_{Mie} / -	3.961	2.002	1.997	1.990	1.982	1.983	1.971	1.964	1.566	2.462

On the one side, experimentally, a strong angular influence of the Mie scattering was proven. On the other side, calculation of the intensity vs. droplet diameter reveals that the general assumption of Mie scattering being proportional to d^2 is only valid at very specific angles. Especially at 135°, our initially preferred angle, the parameter b_{Mie} changes rapidly. Furthermore, heavy oscillations of intensity is observed appear in this region. The forward scattering is much more favorable because of a smooth change of intensity over the scattering angle and a smaller amplitude of these oscillations.

Minimizing the oscillations is important for two reasons. On the one hand, sizing accuracy can be achieved without an increase in the number of pictures averaged. Secondly, a narrower distribution of intensity means, that the laser power can be increased without saturating the CCD chip, and therefore a wider range of droplet sizes can be recorded with one setup, because the chip is then more sensitive in low light regions. This was also observed during the actual LIF/Mie experiments.

6.3 Background - Number of averaged pictures

Comparison of different background images show that the number of images, averaged, makes the most difference. A superposed frequency is smoothened out by increasing the number of averages as seen in the histograms in Figure 51.

The improvement between averaging 1 and 50 shots is also visible in the actual records (left column) in Figure 51. Noise is gradually reduced the more images are averaged. Even when the number exceeds the number of experimental images, a further improvement of quality is achieved For example the horizontal pattern in the background can only be resolved with higher numbers of images.

Generally the noise tends to a Gaussian distribution around 100.7 counts. Subtracting this number of counts evenly across the picture actually produced a better result than subtracting a background of 50 or less averaged pictures, but was not as good as subtracting an averaged background of 250 or more individual pictures.

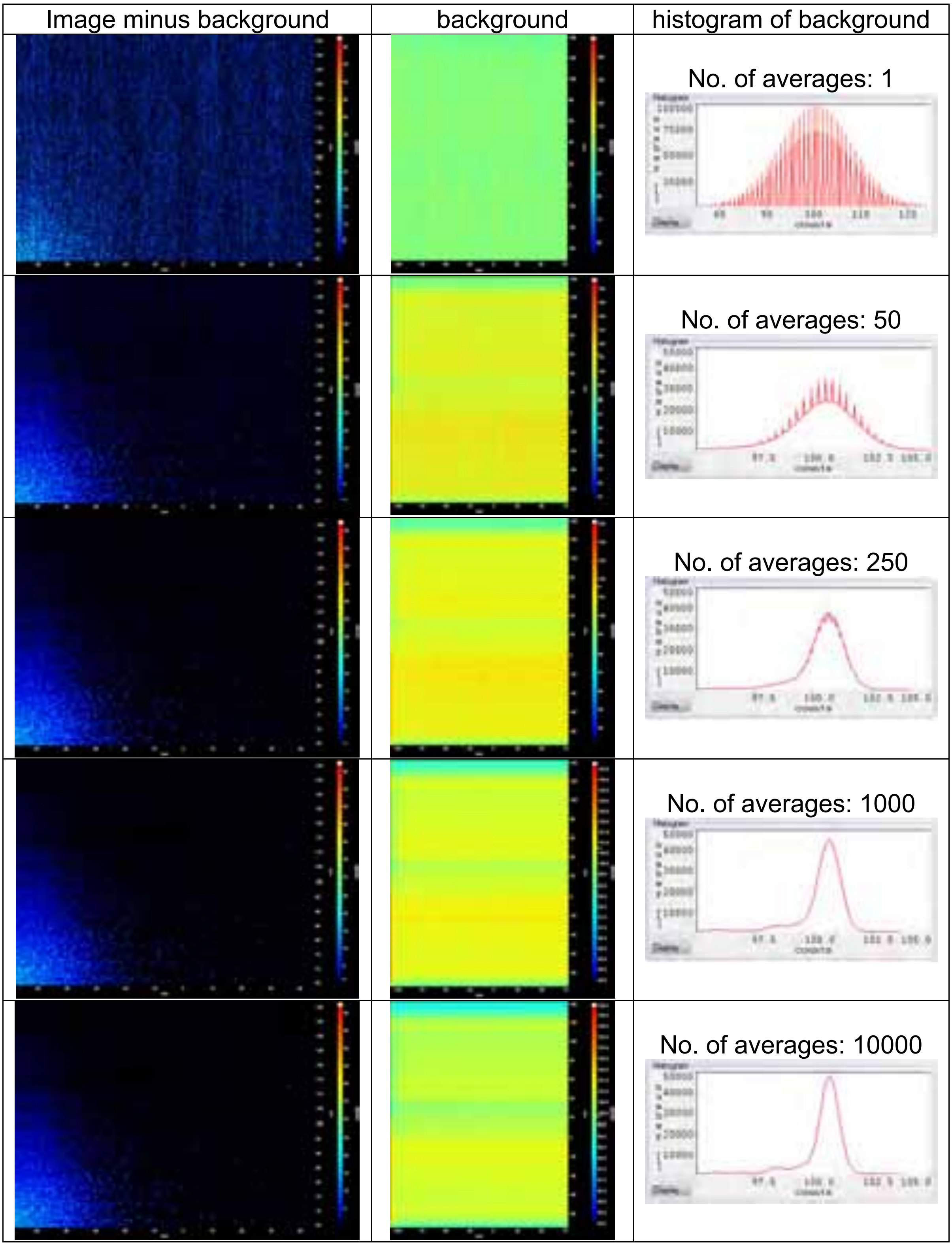

Figure 51: The images are the top right detail from a single shot of Le1 with subtracted background, part of the spray can be seen in the bottom left corner of the images. The middle column shows the used backgrounds and to the very right, a histogram with the distribution of the background files is presented.

As differences might not be visible, a high-resolution version of the images can be found on the CD added to this thesis. Since the chip noise was expected to be in the region of 100 counts, and this was almost the value of our recorded background, a comparison between background and dark image had to be carried out. **Figure 30** shows that the difference between them was marginal.

The small difference between the dark and the background image means, that the electronic noise of the CCD caused most of the 100.7 counts. The very short exposure-time of only 50 microseconds and the filters helped to reduce the ambient light reflections, the beam traps made sure that there is no unwanted laser light pollution. Therefore with this setup it made hardly any difference which of the two is subtracted from the image, though at other circumstances the background picture with the laser on and no spray, may be of advantage, e.g. when it is not possible to use a beam-trap.

The vertical pattern, which was resolved by 250 pictures and more, was the main advantage of physically taking a background image, other than, over the simple subtraction of a constant number of counts.

Considering the results above it was then suggested for further experiments, to average the background with a number of images, higher than at least 5 times the number of experimental images taken. In our case we used 1000 background shots for averaging.

6.4 White sheet - Influence of the aperture

The white sheets, which were used for our setup, are displayed in Figure 52 and Figure 53. Comparing the images for camera one and two at aperture 1.8, it can be seen, that the effect of vignetting was not negligible. Especially at the corners, the intensity droped down to almost 70%. The images also show that there was a difference in peak intensity between the individual cameras, although they were of the same make. Since camera one was set up with a Scheimpflug-adapter, the white sheet is slightly off center. In comparison to that, aperture 22 is shown in Figure 54 and Figure 55. As predicted by theory, vignetting was much higher with a large aperture. This is due to the CMOS technology, which has the actual sensor located below several layers on the CCD-chip. Only incident light perpendicular to the chip can fully illuminate the sensor below the other layers. Only light close to the optical axis can be considered perpendicular. As larger apertures let pass more light on the edge of the lens where it is deflected stronger, more light hits the sensor at an angle on the side of the chip.

An inevitable consequence of a small aperture like 22 is a high depth of field. In normal experiments, this is a desirable effect, but it also makes structures on the white sheet or dust particles visible. In Figure 56 the Mie image from Figure 55 is magnified and the color code was narrowed to the range of 0.9 to 1.1. This makes a pattern visible, which is caused by the individual pixels of the flat screen display (monitor) we used instead of an actual sheet.

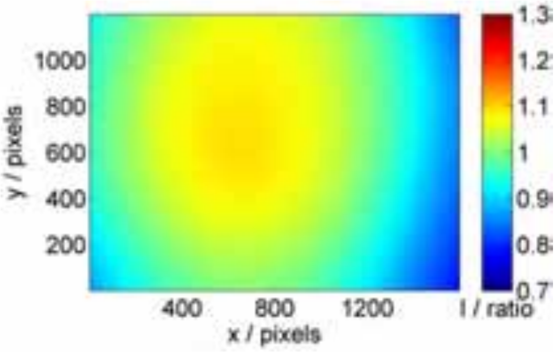

Figure 52: Vignetting on the LIF camera with aperture 1.8

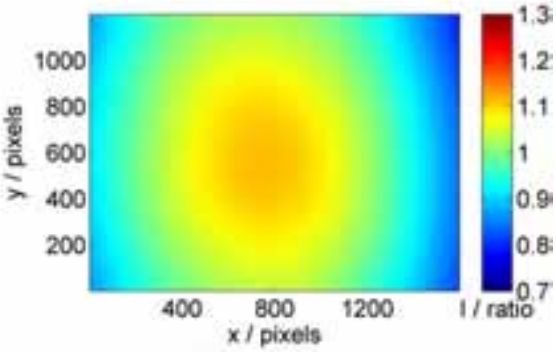

Figure 53: Vignetting on the Mie camera with aperture 1.8

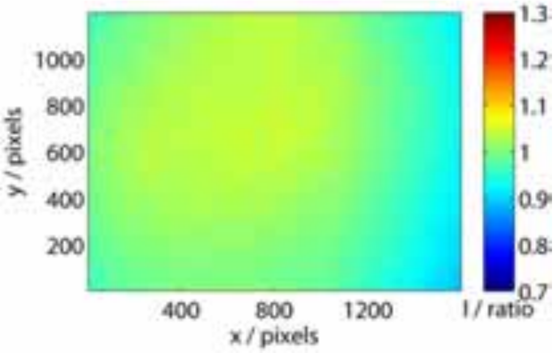

Figure 54: Vignetting on the LIF camera with aperture 22

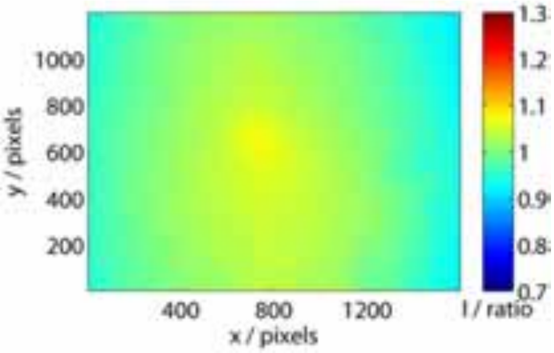

Figure 55: Vignetting on the LIF camera with aperture 22

It is therefore necessary to apply some treatment to the raw files. After processing, the image is smoother, but big particles were still apparent (Figure 57). The exact processing can be found in chapter 4.5.2.

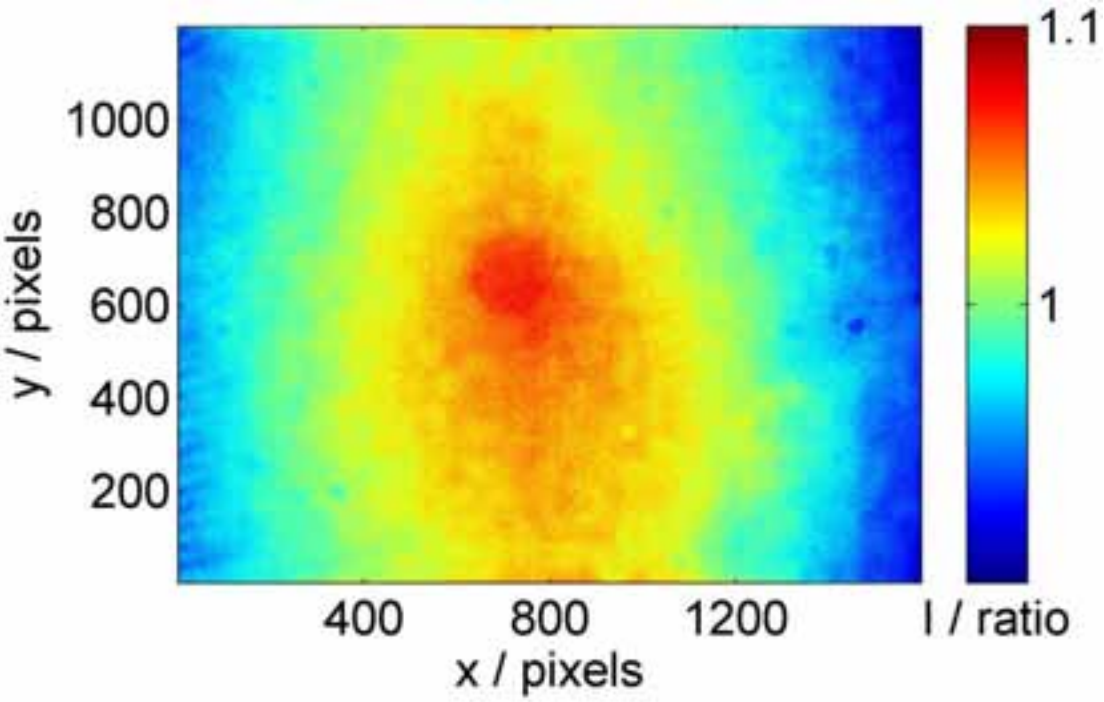

Figure 56: The white sheet of the Mie Camera with aperture 22.

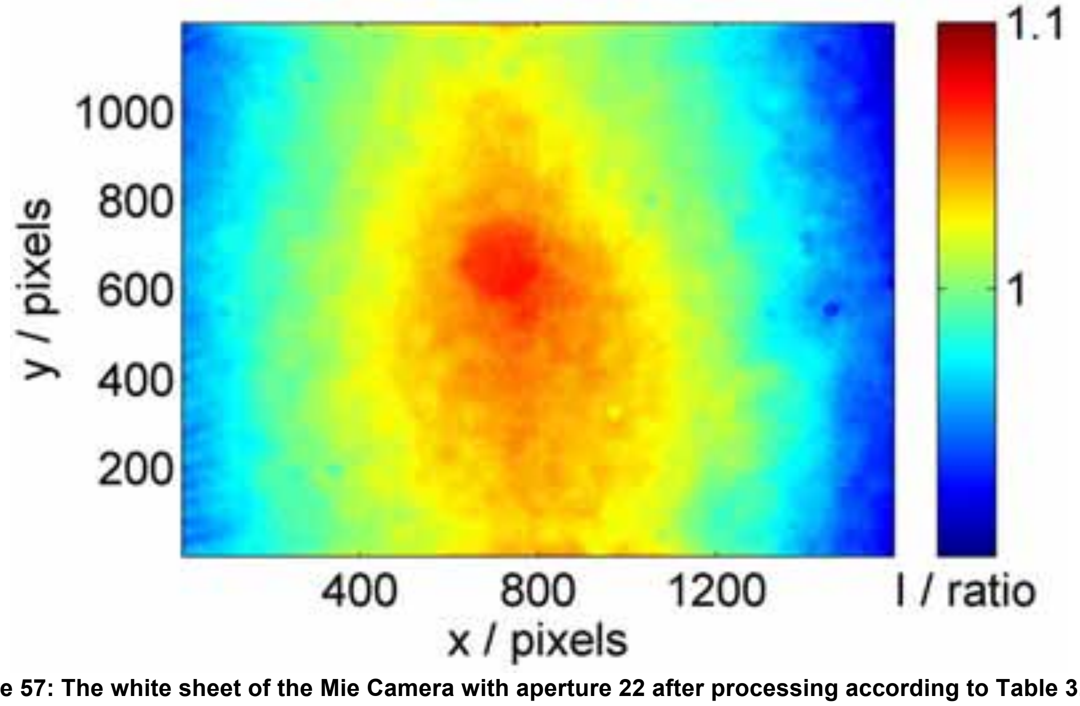

Figure 57: The white sheet of the Mie Camera with aperture 22 after processing according to Table 3.

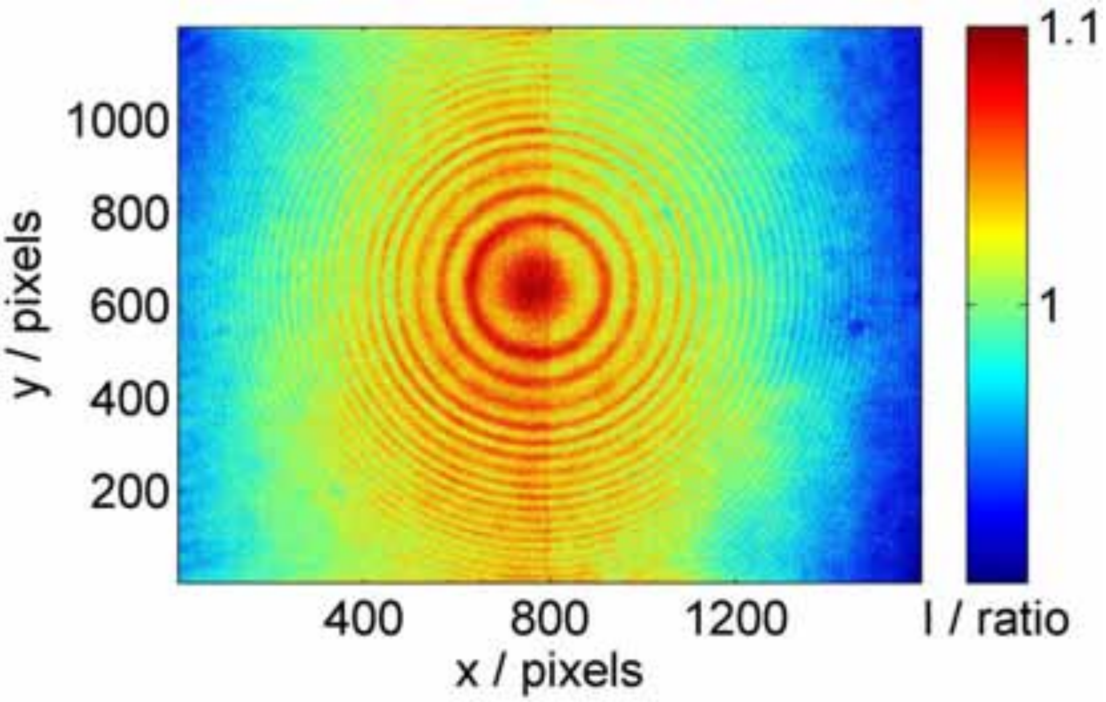

Figure 58: The white sheet of the Mie Camera with aperture 22 using a ND64 filter which was originally intended to be used during the experiments.

Initially it was tried to take the white sheet images with the filters mounted. A Hoya ND64 filter was ordered but as it turned out, dark circles appeared on the Mie camera with mounted filter and fully closed aperture, as shown in Figure 58, the effect seems to be caused by interference. Neither with aperture 1.8 nor with the LIF-filters this effect was seen. Replacing the filter with a Blazer 2.2% eliminated the problem.

6.5 Calibration technique – Variation of parameter *A*

From equation 12 it is hypothized that the intensity ratio LIF/Mie is directly proportional to the SMD, by a constant factor A. Figure 60 shows the calibration points for *Mee* and *Le1*. It can be seen, that the *Le1* nozzle does not touch the extrapolated linear calibration curve of the *Mee* nozzle. In fact the discrepancy is that big, that it is not possible to calibrate *A* for the whole range of droplet diameters by recording *A* at one droplet diameter. In other words, the parameter *A* is not constant, as theory suggests. Therefore it was decided to calibrate the system for each nozzle individually, in order to keep the error low.

The second problem encountered, was finding the same location in the coordinate grid, for both measurement systems. On the one hand, the supporting strut had considerable play and was not stiff enough to exclude any changes in position. On the other hand, it was constructively not possible to have both measurement systems built up simultaneously. Consequently, all nozzles had to be characterized with one setup first and then with the other one. As soon as a nozzle was taken down, it could not be guaranteed any more that next time it would be at exactly the same position.

Figure 59 shows the Mee fog nozzle in the conditions it was calibrated in. The spray spans 80mm vertically, this means an uncertainty of 5mm when calibrating has a big effect on the accuracy of the system. This was the reason why it has been decided to average a square of 10mm by 10mm around the core in order to link it with the droplet diameter provided by Shadowgraphy.

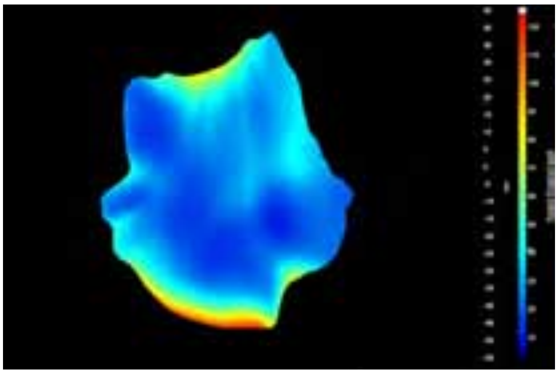

Figure 59: The Mee nozzle measured perpendicular to the orifice-axis with LIF/Mie at standard conditions (138bar z=50mm). The spray spans about 80mm vertically.

PIV-powder-experiments described in chapter 4.2 show that there is a considerable offset between shadowgraphy and the Malvern diffractometry, where Malvern is generally more accurate, but does not have as good of a geometrical resolution as shadowgraphy. It was therefore decided to use Diffractometry for our calibration with the exception of the Mee nozzle, where shadowgraphy produced better results.

6.6 2-camera setup

6.6.1 Depth of field – Scheimpflug-adapter

The low fluorescent light requires a high light sensitivity of the camera lens, respectively a large aperture (low f-number). At an f-number of 1.8, which was the

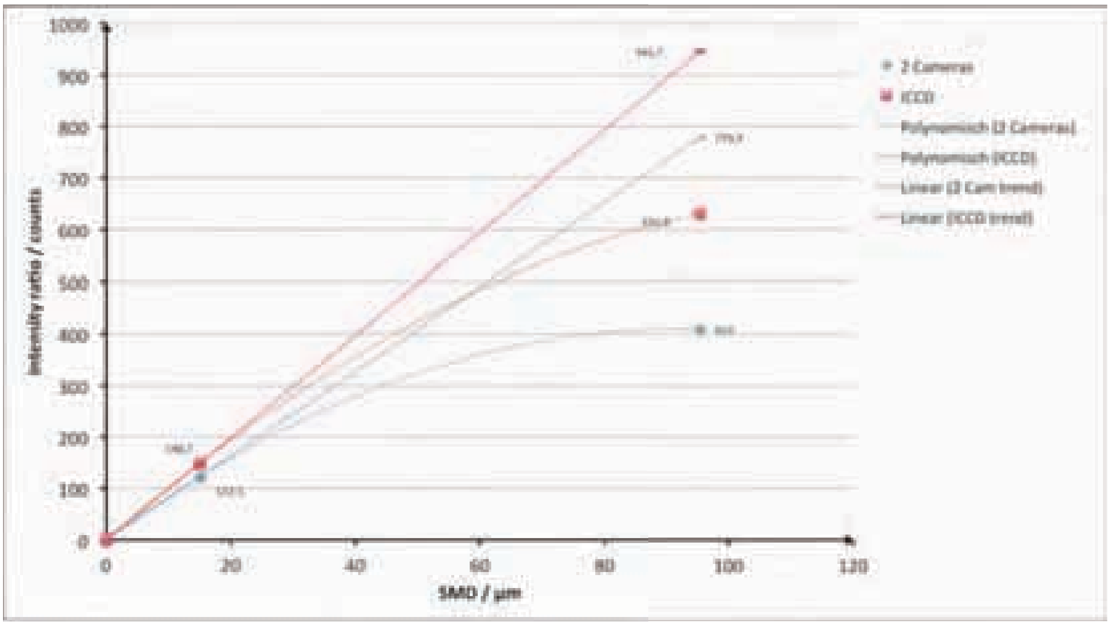

Figure 60: The calibration curves, measured for the 2-camera and the ICCD setup. The linear curves were extrapolated from the Mie calibration, while the polynomic ones were a match with the origin and both calibration points from Table 5.

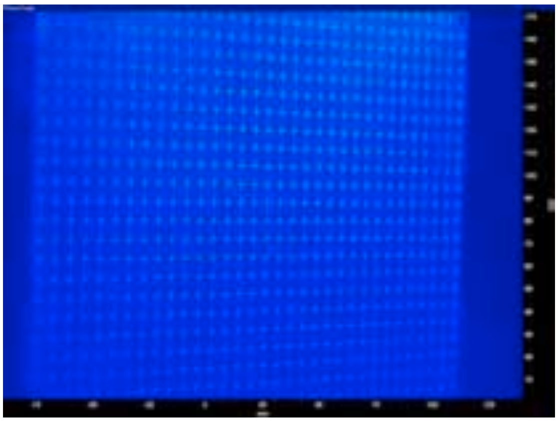

Figure 61: The calibration plate recorded with a Nikon 1.8d lens with aperture 1.8 in a 45° position and 1000mm camera-to-subject distance.

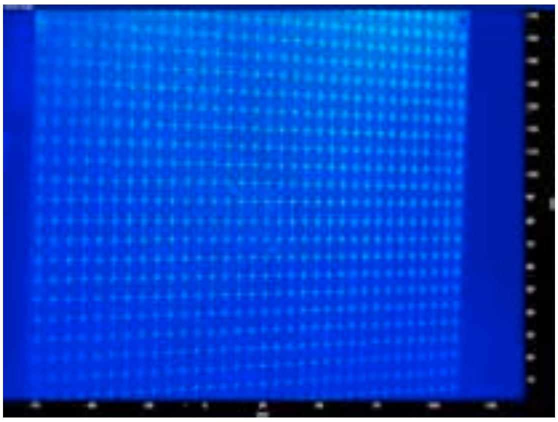

Figure 62: The calibration plate recorded with a Nikon 1.8d lens with aperture 2.8 in a 45° position and 1000mm camera-to-subject distance.

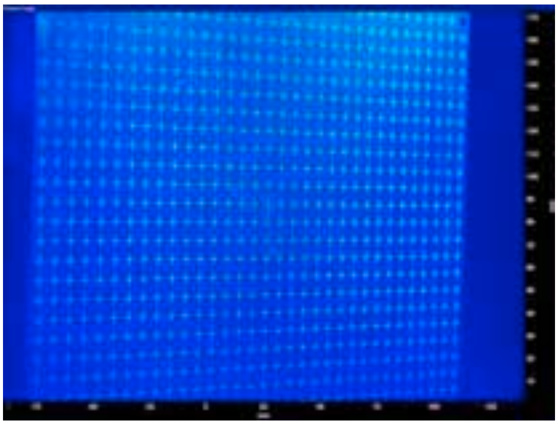

Figure 63: The calibration plate recorded with a Nikon 1.8d lens with aperture 4 in a 45° position and 1000mm camera-to-subject distance.

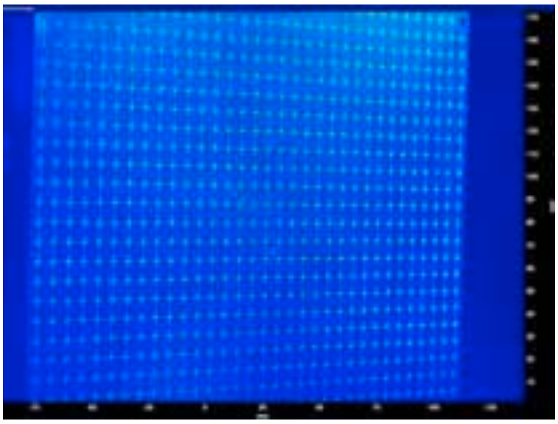

Figure 64: The calibration plate recorded with a Nikon 1.8d lens with aperture 5.6 in a 45° position and 1000mm camera-to-subject distance.

maximum aperture of the lenes used, the borders of the calibration disc got very blurry. This is due to the depth of field, which decreases with lower f-numbers, and due to the inclination of the calibration target. In Figure 61 to Figure 64 the calibration target was recorded using the largest 4 f-stops. At least aperture 5.6 is required in order to guarantee the whole plate being in focus. The irradiance of the sensor must be divided by two with each f-stop. Therefore at aperture 5.6 only 12.5 percent of the light passes the lens compared to aperture 1.8. Therefore a large aperture is a must for low-light LIF recording, but due to the low depth-of-field at large aperture and the inclination of the target area (calibration target, LIF laser light sheet), most parts of the target are out of focus. To compensate for that effect a Scheimpflug adaptor was necessary. With such a Scheimpflug adaptor the image plane can be tilted relative to the lens, such that the inclined target plane is in focus for all positions imaged (see also Figure 23).

6.6.2 Beam splitter

Fluorescence is generally a lot weaker than the Mie scattering. Therefore the idea was to use a beam splitter, which distributes the light unevenly. Desired was a ratio

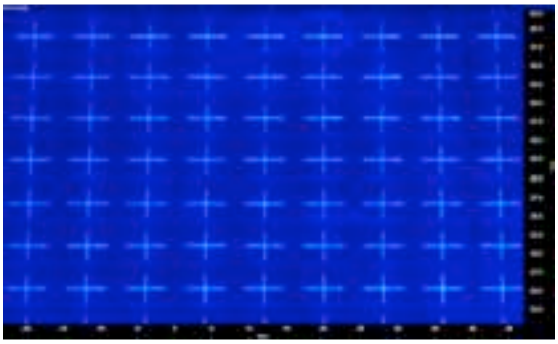

Figure 65: The calibration plate recorded through the beam splitter no.1 with 25% reflection and 75% transparency set up the right way.

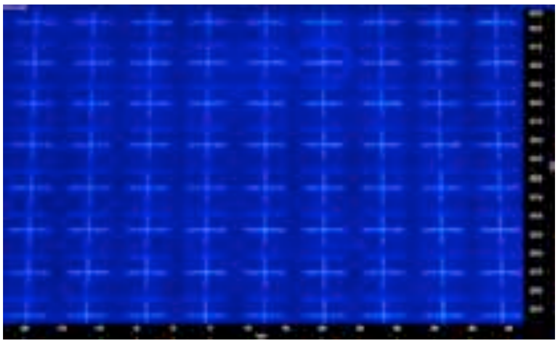

Figure 66: The calibration plate recorded through the beam splitter no.1 with 25% reflection and 75% transparency set up the wrong way.

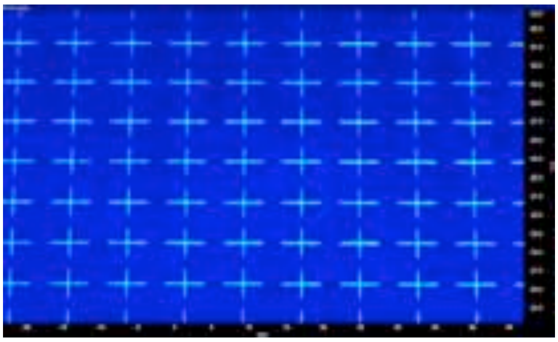

Figure 67: The calibration plate recorded through the beam splitter no.2 with 50% reflection and 50% transparency set up the right way.

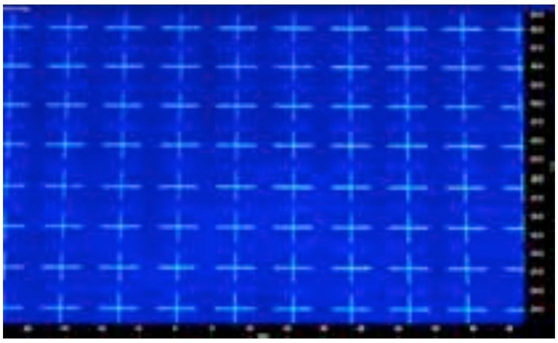

Figure 68: The calibration plate recorded through the beam splitter no.2 with 50% reflection and 50% transparency set up the wrong orientation.

of 99% transparency and 1% reflection (99/01). That would have replaced the neutral density filter, used in order to reduce the strong intensity of Mie scattering. The necessary ratio was not available at the time though. Therefore a 75/25-filter was tested. The problem with this part was, that a ghost image of the target appeared. Depending on the way the beam splitter was mounted, the second target image (crosses) was weaker (Figure 65) or stronger (Figure 66), but there was no setup where the ghost image was eliminated.

In contrast to that, a major improvement was achieved by using a 50/50-splitter. No matter, which way it was built in, the signal was clearer than the one recorded with the 75/25-splitter. A significant difference between the two different orientations of mounting can be seen in Figure 67 and Figure 68, where the first one has no ghost image at all.

6.7 ICCD - Image doubler

6.7.1 Gain vs. shutter time

When using an image intensifier, a higher gain increases not only the intensity but also the noise. In Figure 69 and Figure 70 a low gain of 0.32 and a high gain of 0.88 are compared. The first image is clear and the calibration target (crosses) are well defined. The latter is quite noisy, fine details such as the crosses are not well displayed. The very bright spot on the lower left side of the center is due to reflection of the spotlight.

In order to reach a similar number of counts in both pictures, the shutter time has been adjusted individually.

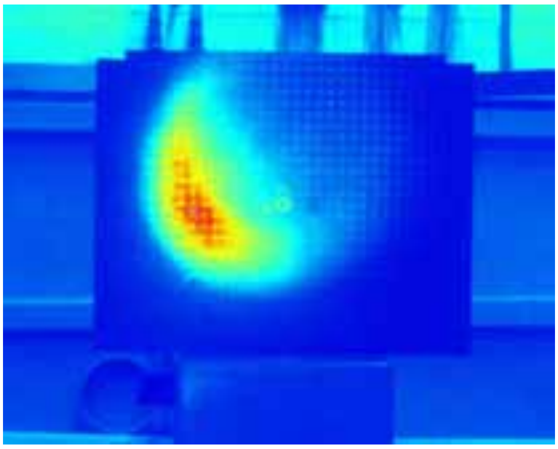

Figure 69: The calibration plate recorded with the ICCD camera. The gain was set to 32 percent and the exposure time was 10000 µm.

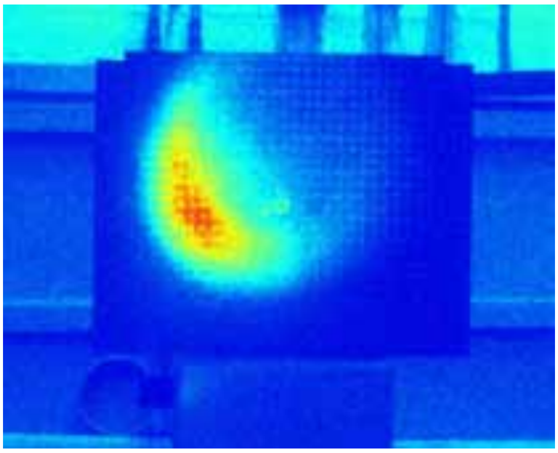

Figure 70: The calibration plate recorded with the ICCD camera. The gain was set to 88 percent and the exposure time was 1000 µm.

6.7.2 Image doubler

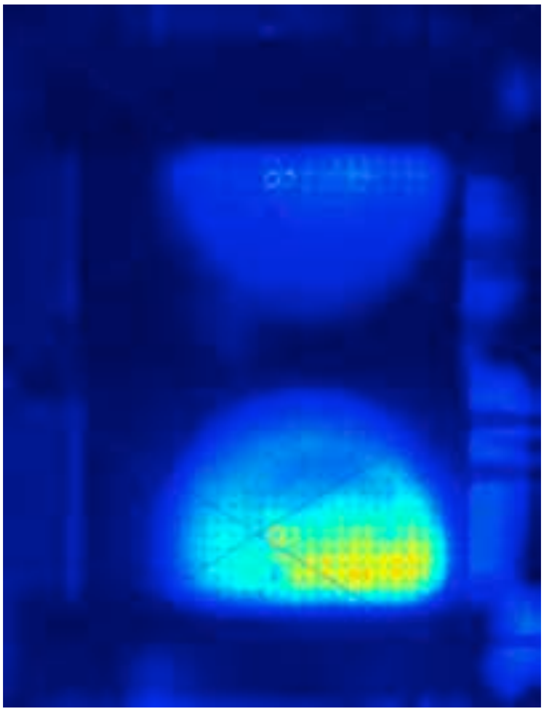

Figure 71: Adjustment of the beamsplitter using the calibration plate (array of crosses).

The image doubler had to be adjusted before use, an adjustment which was conducted in two steps. First, the mirrors had to be set so that the measurement area was centered on each of the CCD's half-sides. As shown in Figure 71, this is done by, using the calibration plate. A small circle seen in the figure is drawn onto the plate, marking its center. The diagonal crosses mark the center of each CCD chip-half. They were drawn as an additional layer in the DaVis software. In order to adjust the mirrors, they were moved until the circles on the plate touched the center of the diagonal crosses.

The semilunar shaped brighter spots in both halves were due to the low aperture of 22.

The second step of adjustment is moving the center-prism into the appropriate direction. In Figure 72 and Figure 73 the LIF and Mie halves of the CCD chip are shown with the prism all the way in. It can be seen, that on the LIF's half, the lower side of the calibration plate and on the Mie's half the opposite side just vanished. On the other side, the positioning screw all the way out, causes a ghost image. The LIF's image (Figure 74) shows a silver part of the laser support, which in reality was about 100 mm away from the calibration plate in x+direction, while the Mie image shows the top edge of the beam trap, which was about 80mm in opposite direction.

It was then necessary to find a good compromise between a reduced measurement area (all the way in position) and the ghost images (all the way out position), where neither of the two effects would influence the result too much.

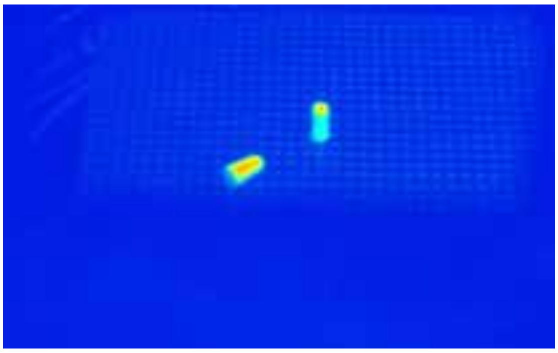

Figure 72: The LIF side of the chip with the center-prism all the way in. Two cones can be seen. They were placed there in order to find the center of the calibration target more easily.

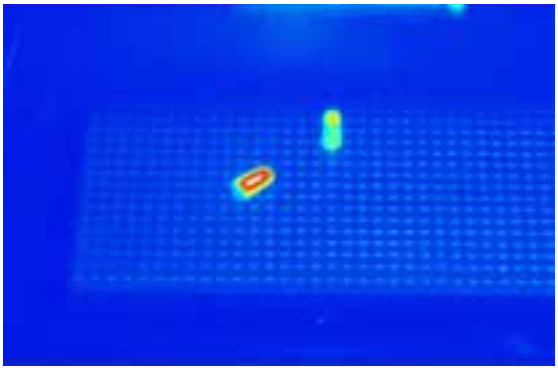

Figure 73: The Mie side of the chip with the center-prism all the way in.

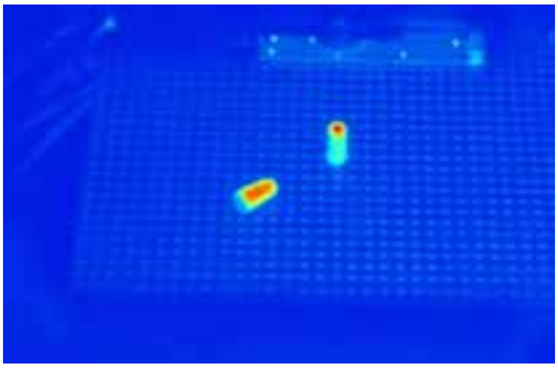

Figure 74: The LIF side of the chip with the center-prism all the way out.

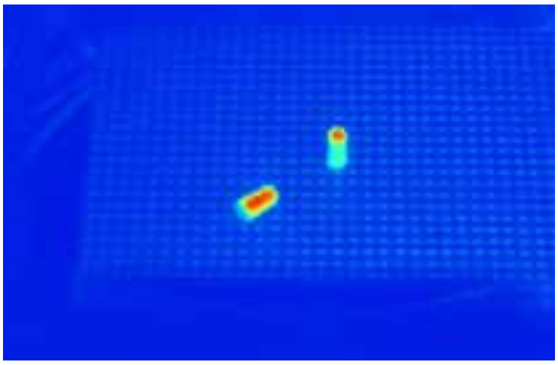

Figure 75: The Mie side of the chip with the center-prism all the way out.

6.8 LIF/MIE – Parameters of influence

6.8.1 Order of processing

It was necessary to average the pictures before and not after performing the geometrical calibration. Otherwise the diameter was highly dependent on the density and the fluctuation of the spray. Figure 76 and Figure 77 show the comparison of processing for a highly dense spray on the example of the Mee nozzle at a distance to orifice of 50mm and a cross section, perpendicular to the orifice-axis. Qualitatively, the error was not big. The image, averaged at the end (the one on the right side), appeared smoother in general and faded out more at the edges. The region of big droplets seen on the bottom of the images can not be explained yet, the droplets in this region are actually not bigger than on the left and right edge of the spray as shown in chapter 6.10.6.

In contrast to that the low-density spray of Le1 is shown in Figure 78 and Figure 79. Measured at 500mm down the z-axis with a crosssection, perpendicular to the orifice-axis, the error made by averaging at the end was extremely high. Averaging at the end lowers the diameter across the spray by a factor of 2-3. Here, chances that a

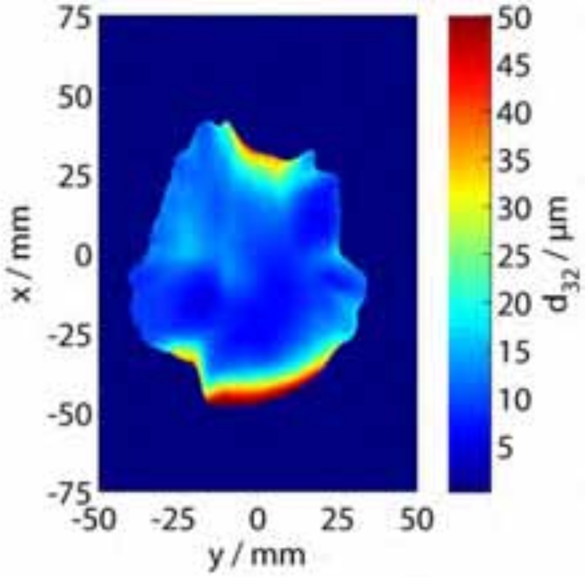

Figure 76: The Mee Nozzle was recorded in standard conditions. Processing was performed according to 4.6.

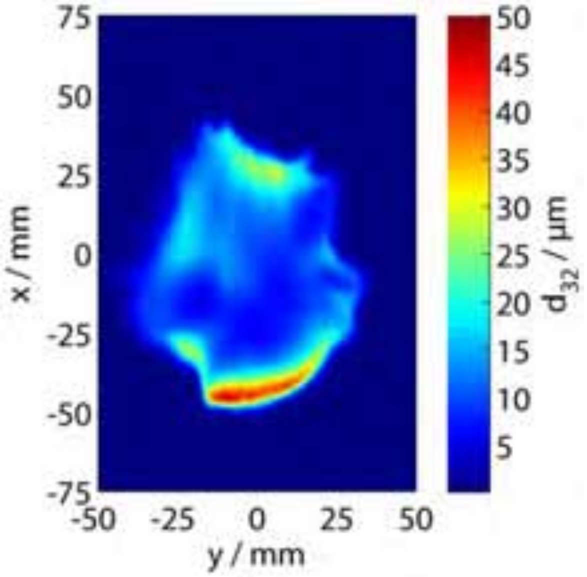

Figure 77: The Mee Nozzle again recorded in standard conditions. This time, processing was applied to the individual images. At the very end all images were averaged.

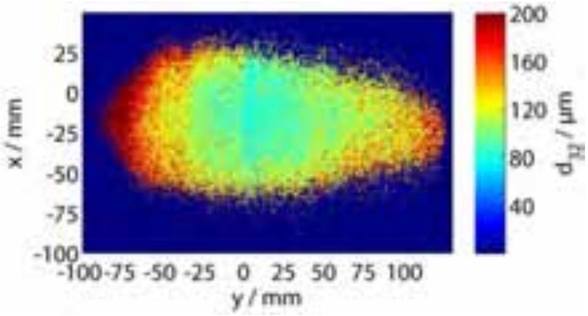

Figure 78: The Le1 Nozzle was recorded in standard conditions. Processing was performed according to Table 6.

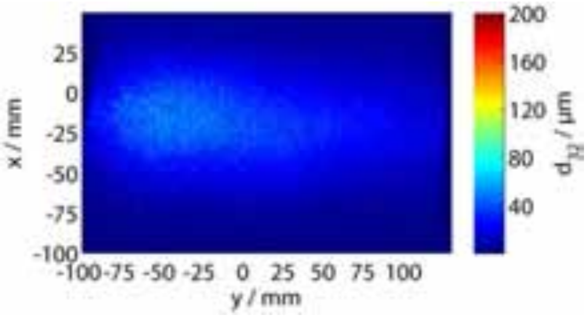

Figure 79: The Le1 Nozzle again recorded in standard conditions. This time, processing was applied to the individual images. At the very end all images were averaged.

pixel with a particle on it is averaged with an empty pixel is much higher than in a high density spray, where, at least in the core of the spray, all pixels have a droplet.

6.8.2 Number of images averaged

The influence of the number of averaged images has been investigated in Figure 80 Figure 81. The high-density spray of the Mee nozzle generated enough droplet samples, so the number of images did not significantly change by averaging more than the usual 200. A maximum of 2000 pictures had been recorded, but compared to an average of 200, no difference can be seen. Only the contour lines get smoother. Averaging 200 pictures was therefore chosen to be sufficient.

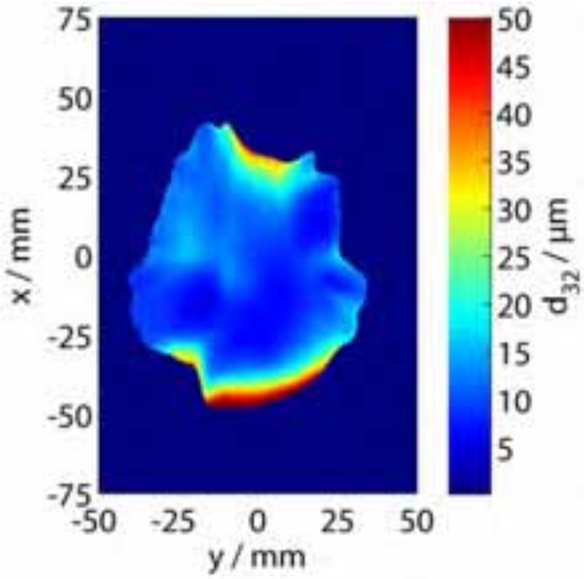

Figure 80: The Mee Nozzle is recorded in standard conditions with a sample number of 200.

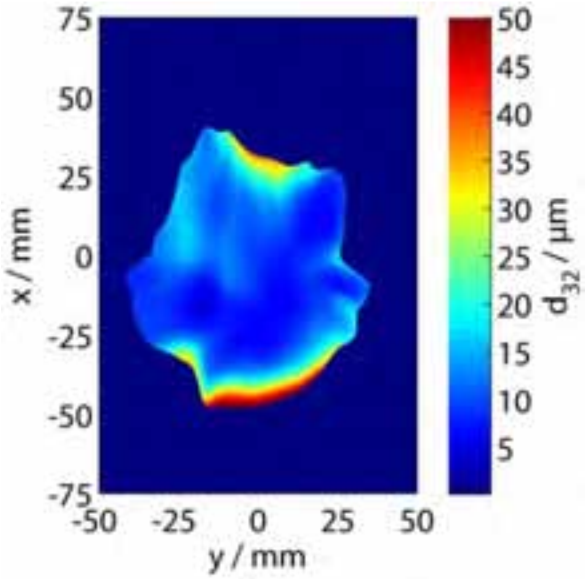

Figure 81: The Mee Nozzle is recorded in standard conditions with a sample number of 2000.

6.8.3 Pixel sliding

The function ‘Pixel sliding’ was necessary because of our setup with two cameras. Both lenses had a mechanical play, which could produce an unwanted shift between the images of up to 10 pixels. Even stabilizing the lenses with rubber bands did not guarantee that the lenses go back to their initial position, after they have been touched. E.g. every time the filters needed to be mounted or after strong vibrations of the test rig, LIF and Mie images did not match anymore. Therefore the pictures need to be rematched afterwards. For that reason, a big isolated droplet was chosen which could be clearly identified in both, the LIF- and the Mie-image. Then the variables for x- and y-shift in the macro ‘pixel sliding’ were altered until the LIF and the Mie signal of the droplet matched again. Rotation of the images was not necessary, as the mechanical play of our lenses seemed to affect only transversal movement. As you can see in Figure 82 to Figure 85, this step is particularly important when single rather than time-averaged shots are of interest. The most critical situation is the low-density spray seen in Figure 83 and Figure 84. In unmatched images, the chance is high that the LIF signal of a certain droplet is divided by a zero value of the Mie image, since the Mie signal of the same droplet is zero in the neighboring pixel. The Output is then cancelled. Figure 83 shows that in contrast to the matched image (Figure 82) the spray with not matched processing was characterized by higher peaks (red dots) but less overall spray density. The denser Mee nozzles spray proved to be less affected even when a single image was considered, but a systematic error remains anyway without image shift correction.

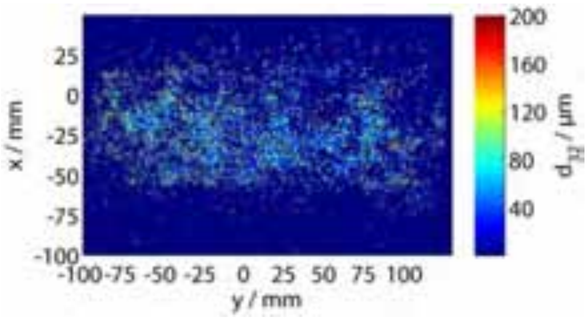

Figure 82: A single shot of the Le1 nozzle in its standard conditions. The introduced processing step ‘pixel sliding’ has been applied.

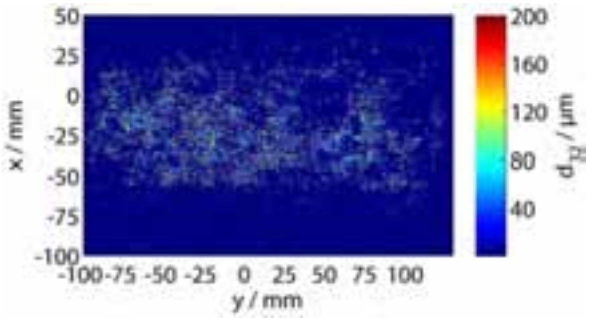

Figure 83: The same record of Le1 nozzle in its standard conditions processed with the conventional steps without ‘pixel sliding’.

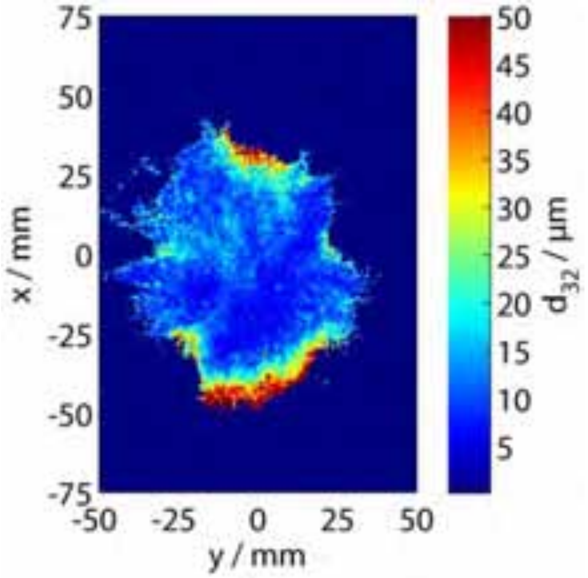

Figure 84: A single shot of the Mee nozzle in its standard conditions. The introduced processing step ‘pixel sliding’ had been applied.

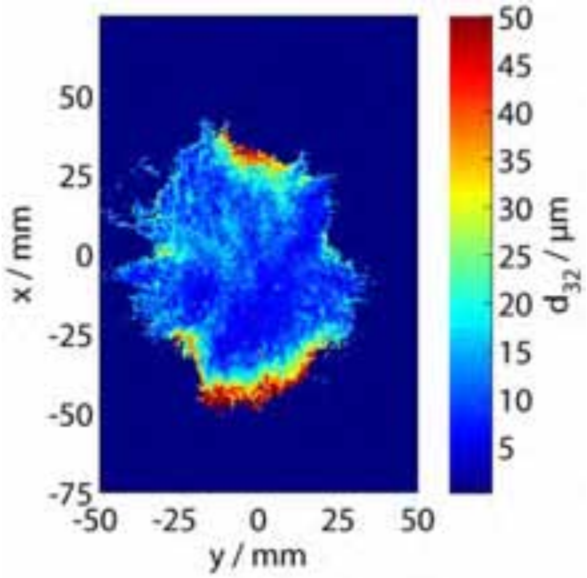

Figure 85: The same record of Mee nozzle in its standard conditions processed with the conventional steps without ‘pixel sliding’.

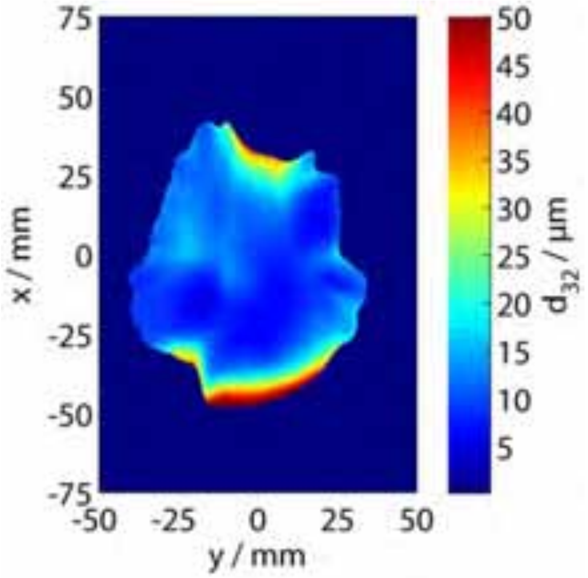

Figure 86: The Le1 nozzle in its standard conditions, recorded and averaged over 200 shots. The introduced processing step ‘pixel sliding’ has been applied.

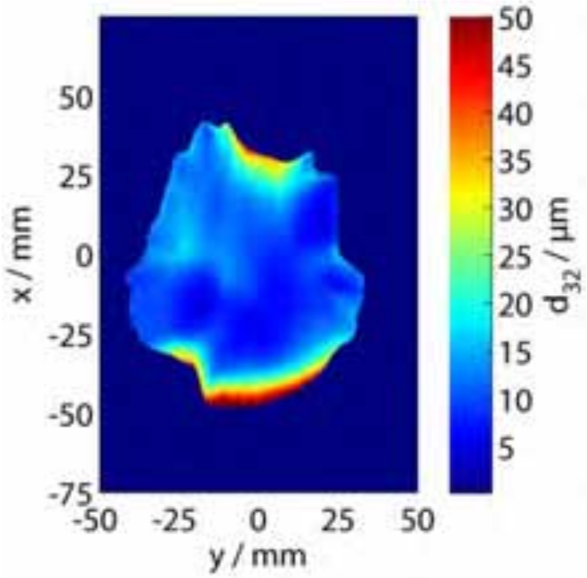

Figure 87: The Le1 nozzle in its standard conditions, recorded and averaged over 200 shots, processed using the conventional steps without ‘pixel sliding’.

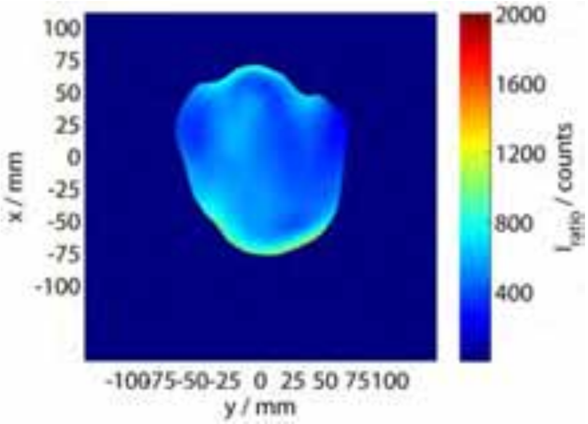

Figure 88: The OP-37 pilot oil nozzle at a distance z=200m downstream (measurement Number 303), recorded with laser A and B at 100% power.

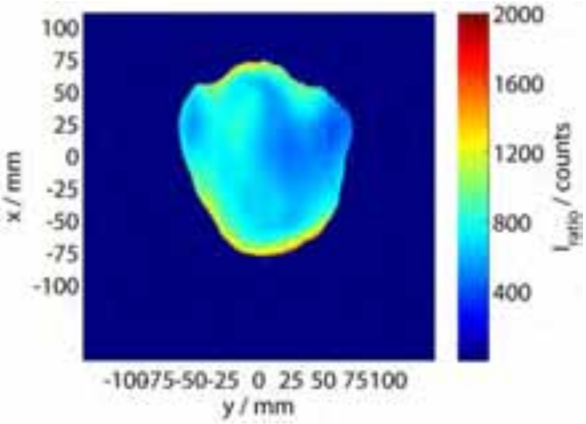

Figure 89: The OP-37 pilot oil nozzle at a distance z=200m downstream (measurement Number 302), recorded with laser A at 30% power.

6.8.4 Influence of laser power

The laser power had to be reduced considerably for measuring the pilot oil nozzles. Their great mass flow and droplet diameter caused an increased LIF signal combined with a still moderate Mie signal.

In theory, light emission should be proportional to the irradiance by the illuminating light, for both, Mie scattering and fluorescence. Dividing the two images should therefore cancel out any fluctuation of the incoming light. From Figure 88 to Figure 89 the laser power has been reduced by 85%. A clear influence can be seen when the droplet diameter seems to increase while decreasing laser power.

The smooth appearance of Figure 88 is caused by a stronger smoothening filter.

6.8.5 Effect of image smoothening

Smoothening was generally applied to the images for better visibility. In case of the pilot oil nozzles, a distinct pattern was observed. It only appeared after geometrical distortion and indicated aliasing. A smoothening filter helped to reduce the effect, although this was normally avoided by an increase of interpolation points.

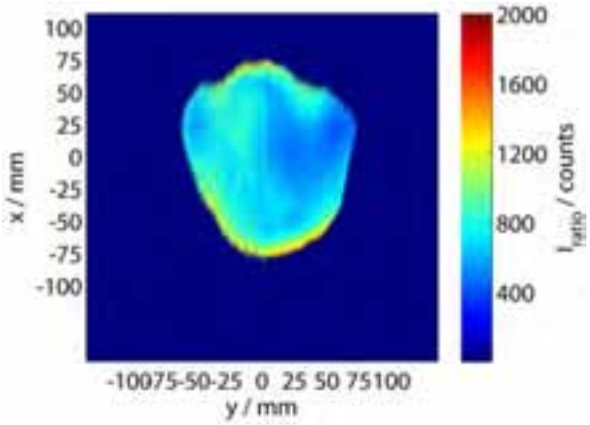

Figure 90: The OP-37 pilot oil nozzle at a distance z=200m downstream (measurement number 302). 200 frames have been averaged. No smoothening has been applied during processing.

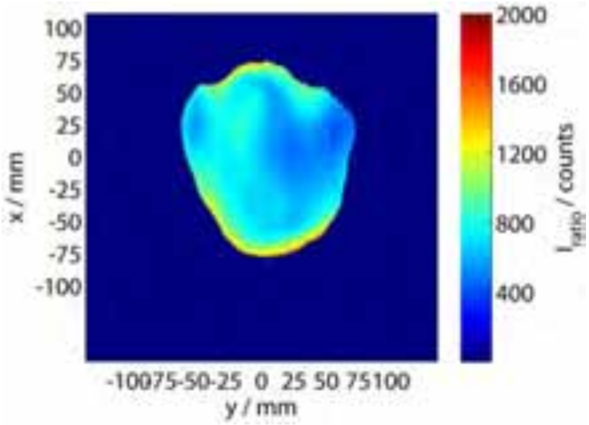

Figure 91: The OP-37 pilot oil nozzle at a distance z=200m downstream (measurement number 302). 200 frames have been averaged. A 5x5 pixel smoothening filter has been applied during processing.

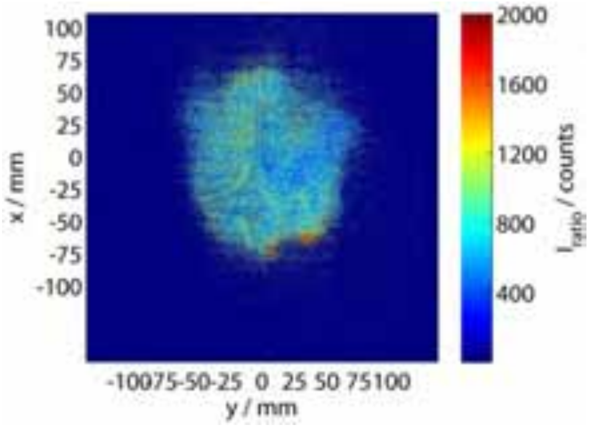

Figure 92: A single shot of the OP-37 pilot oil nozzle at a distance z=200m downstream (measurement number 302). No smoothening has been applied during processing.

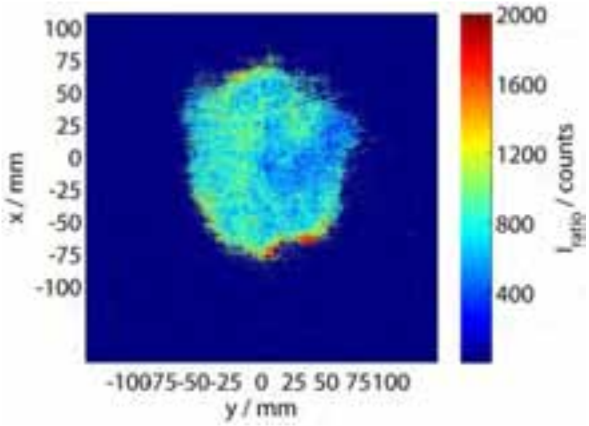

Figure 93: A single shot of the OP-37 pilot oil nozzle at a distance z=200m downstream (measurement number 302). A 5x5 pixdel smoothening filter has been applied during processing.

6.8.6 Division of images – Intensity ratio

The LIF images of the Mee nozzle (Figure 94) and the OP-P12 (Figure 97) show that the spray cone out of the laser sheet was also partially fluorescent. Especially the OP-P12's image shows how the droplets were illuminated right after the nozzle orifice.

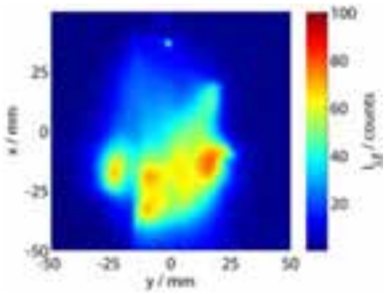

Figure 94: The LIF-image of the Mee-Fog nozzle in standard condition.

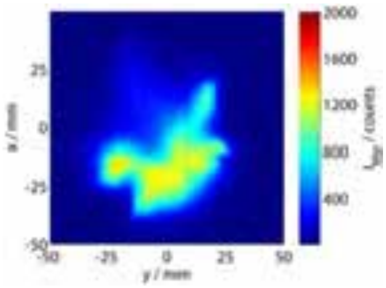

Figure 95: The Mie-image of the Mee-Fog nozzle in standard condition.

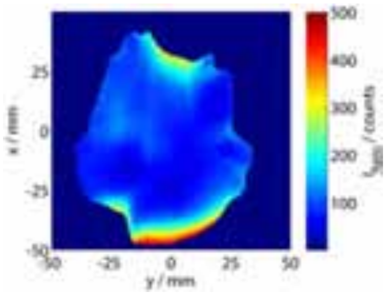

Figure 96: Division of the LIF- and Mie-image give the intensity ratio

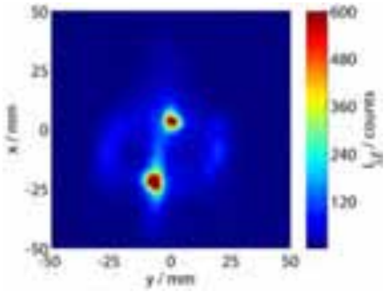

Figure 97: The LIF-image of the OP-P12 pilot oil nozzle measured at z=50mm

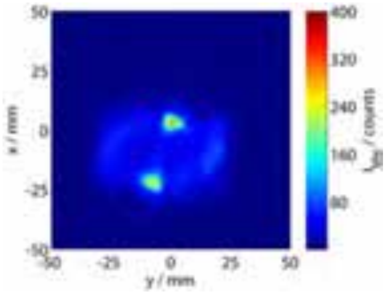

Figure 98: The Mie-image of the OP-P12 pilot oil nozzle measured at z=50mm

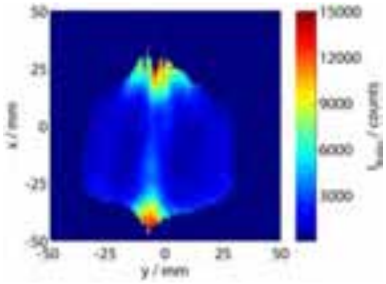

Figure 99: Division of the LIF- and Mie-image give the intensity ratio

In the Mee nozzles image, the region below the spray was additionally illuminated. This caused an unreasonably high droplet diameter in –x direction of the spray, visible on the bottom of Figure 96. Only ignoring counts below a certain threshold helped reduce the effect, but this was a tradeoff where signal was lost in other regions. The images below were processed with quite a high threshold already. A lower one would have increased the region of big diameters on the bottom of Figure 96. Therefore the assumption of a planar measurement area included a systematic error. The fact that the area along the y-axis is not prone of the effect, proved, that it had to do with droplets being above and below the spray.

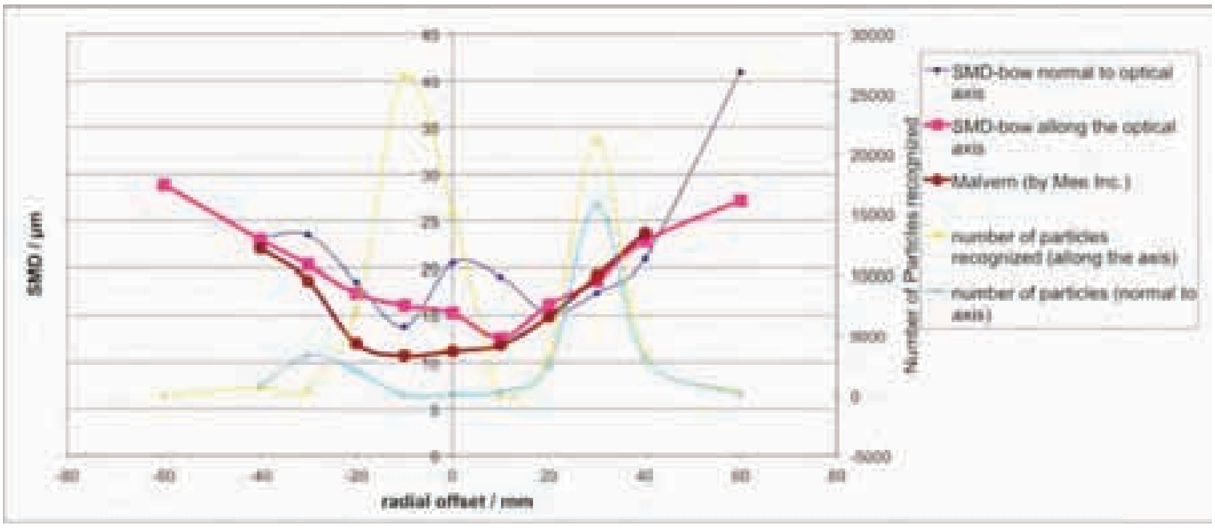

Figure 100: The Mee nozzle at standard conditions, measured with Shadowgraphy. For comparison, the diffractometry measurements, carried out by Mee Inc. and described by Chaker et al (2002), are shown too.

6.9 Characterization of nozzles

The Mee nozzle was characterized with shadowgraphy at standard conditions at 138 bar pressure and 2.7g/s mass flow rate. The recordings were done at an axial distance from the orifice of 50mm from the orifice. This is presented in Figure 100. Immediately it can be seen, that there was a big difference depending on the way the nozzle was mounted. Due to an asymmetric nozzle design, the pink and blue curves differed considerably. The pink curve was symmetrical around y = +10mm, since the nozzle was mounted parallel to the optical axis, this was the estimated result. The slight offset can be explained with an imperfectly welded nozzle bow, which directed the spray in to a direction slightly off-axis.

The light blue curve representing the number of particles recognized in the configuration normal to the optical axis shows, that the region behind the nozzle bow had barely any droplets, while the number of particles on the opposite side was in the order of magnitude of the perpendicular measurements. In comparison to that, the Diffractometry measurements from the Mee nozzle done by Mee Inc. were very close to the pink curve, although it was unknown, which way Chaker et al (2002) mounted the nozzle.

As an example for variation of the y-coordinate, the Le1 nozzle is presented in Figure 101. LIF/Mie measurements have been averaged across the spray in order to be comparable to the ones recorded with the diffractometry system. The sample number was not increased and still counted 200. At the same time, droplet diameters were as high as 250 µm. The resulting reduction of the number of droplets was also a reduction of total samples. Therefore, the number of image-samples should have been increased to balance this effect. The large oscillations of the LIF/Mie curve in Figure 101 were explained by that.

Comparing Diffractometry and LIF/Mie records, a good agreement was given around

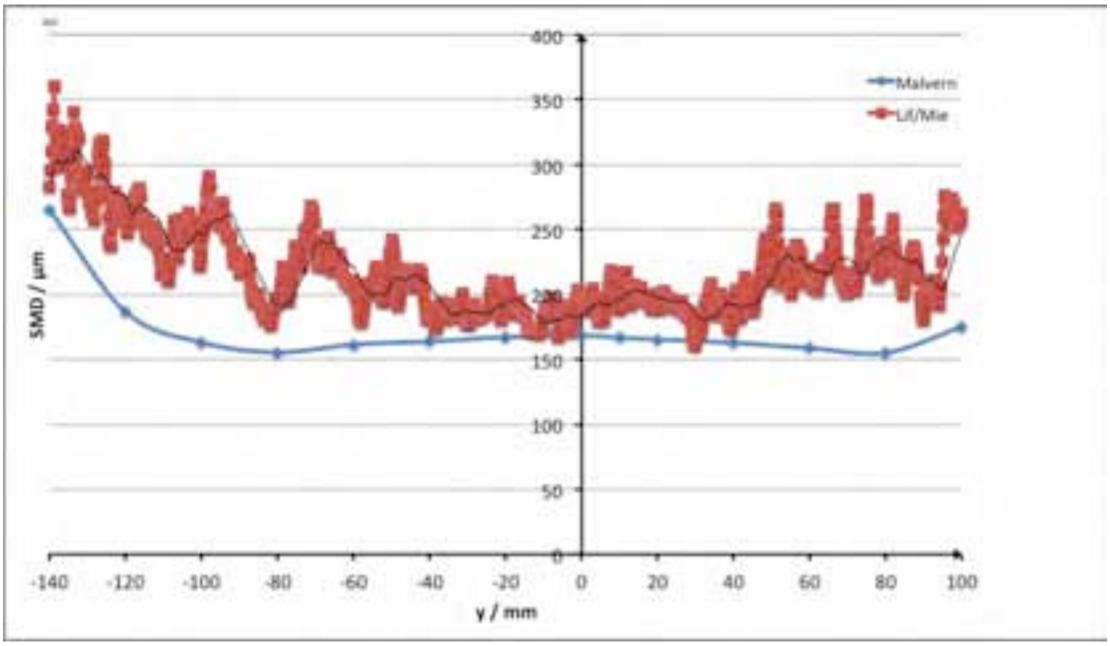

Figure 101: A profile of the Le2 nozzle at 3500mbar and z=150mm, measured by diffractometry and LIF/Mie. The black line is a moving average of the LIF/Mie records.

the origin (y = 0). As LIF/Mie was calibrated at y = 0, this was expected. Discrepancy increased though, in y+ and y- direction.

6.9.1 Pressure Variation

Variation of the pressure has been carried out with LIF/Mie in both, the ICCD- and the 2-camera configuration and with the Diffractometry system, not with shadowgraphy. In Figure 102 the varying SMD of the Mee nozzle is presented. The curves at the core were gained by averaging a 10 by 10mm square as described in the chapters 4.5.3 and 4.5.4, while the green and purple curves were an average across the spray with 10mm width, in order to compare the result with the integrating character of Diffractometry. For both the ICCD and the 2-camera measurements, the core value was lower than the across value (Figure 102). The difference was increasing with pressure. Both phenomena are typical behavior for sprays, when bigger droplets, with higher momentum keep their direction for a longer time than smaller ones. Theoretically both ICCD and 2-camera results should have measured 15µm at standard conditions (138bar, z=50) while the ICCD setup achieved this value. The 2-camera setup failed it by 5µm. This was explained by several points of measurement. 1. Calibration was performed 2 weeks earlier than the pressure variation.

2. LaVision specifies the uncertainty of the system with 30% (LaVision, 2010) which could be an explanation.

3. The fact, that the axial distance to orifice variation as shown in Figure 104 seemed to be off by 3µm as well, shows that the system was only reproducible, when accepting a certain uncertainty.

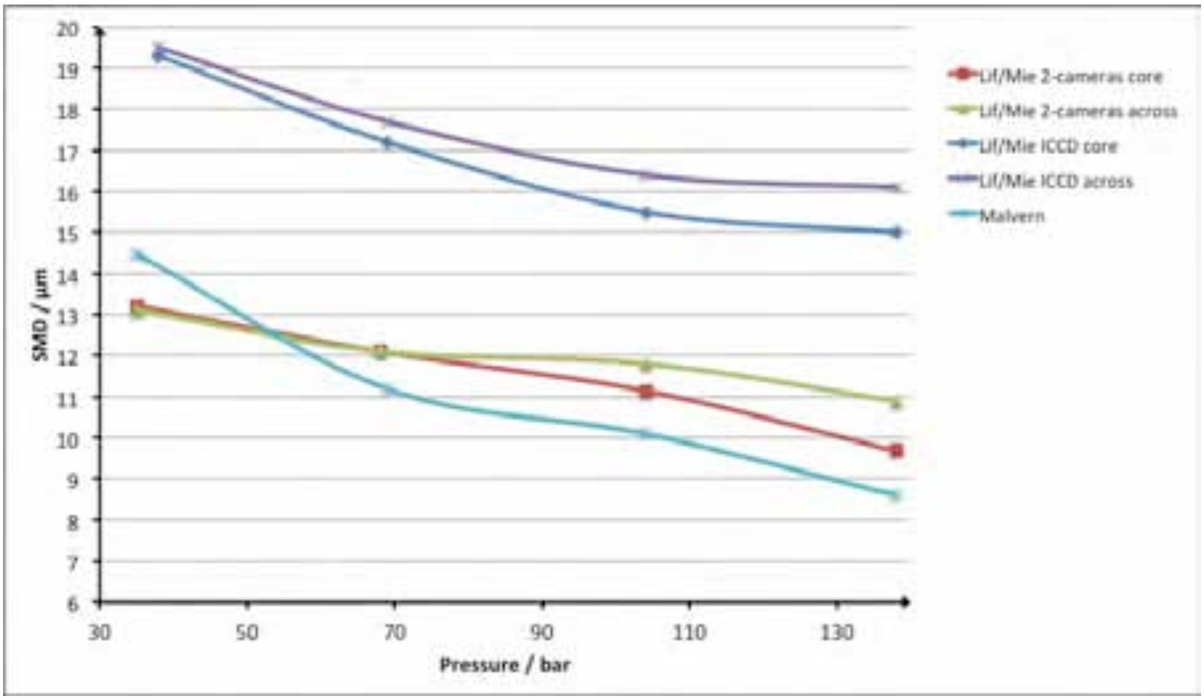

Figure 102: Pressure variation of the Mee nozzle at z=50mm.

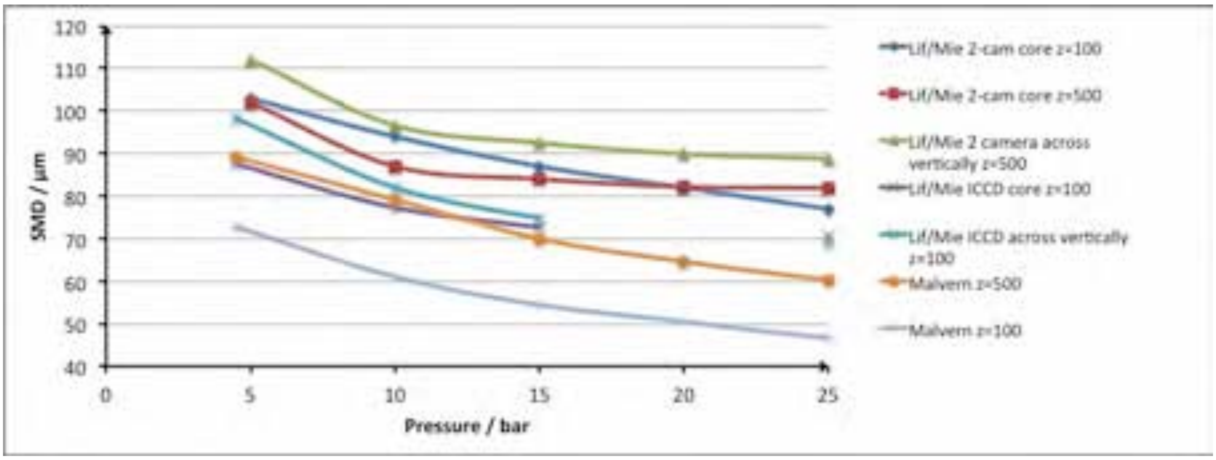

Figure 103: Pressure variation of the Le1 nozzle at z=500mm.

All sets of measurements had in common, that the diameter was gradually reduced with increased pressure.

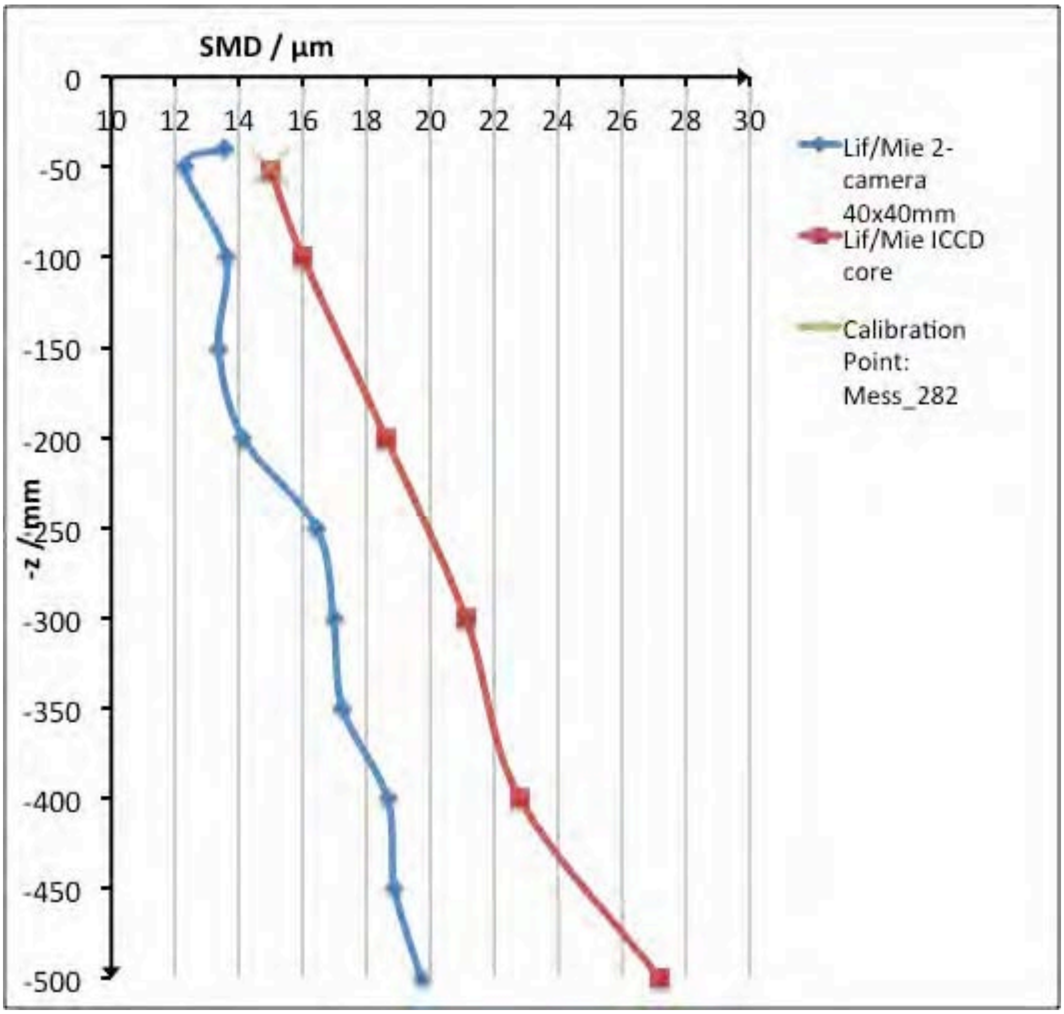

Figure 104: The Mee nozzle with varying axial distance to the orifice, measured at 138000 mbar.

Viewing the Le1 nozzle again, the droplet diameter decreased with increasing pressure as expected. Quite large variations between the individual measurement systems and setups were observed.

6.9.2 Distance-to-orifice variation

For this investigaiton pressure was kept constant at the nozzles standard condition. From z = 50mm on, a continuous increase of droplet diameter with increasing axial distance was observed (Figure 104). While the 2-camera setup showed slight oscillations, the ICCD cameras slope was very smooth. Averaging was carried out for a square of 40mm by 40mm moving with the core of the spray. As mentioned above, the spray tilts to the side, therefore, with increasing distance, the core of the spray was not at the origin of the coordinate system any longer. The core of the spray had to be estimated. The increased area of averaging reduced the influence of not exactly finding the center of the spray.

Regarding the distance variation of Le1 (Figure 105), uncertainties get very obvious. The dark blue and the green curve had identical nozzle configurations, and measurement setups. Both curves were obtained by averaging a 10mm square at the core. The only difference was, that the green curve was acquired 2 weeks earlier than the blue one. A dramatic difference in diameter was observed, while qualitatively they compared very well.

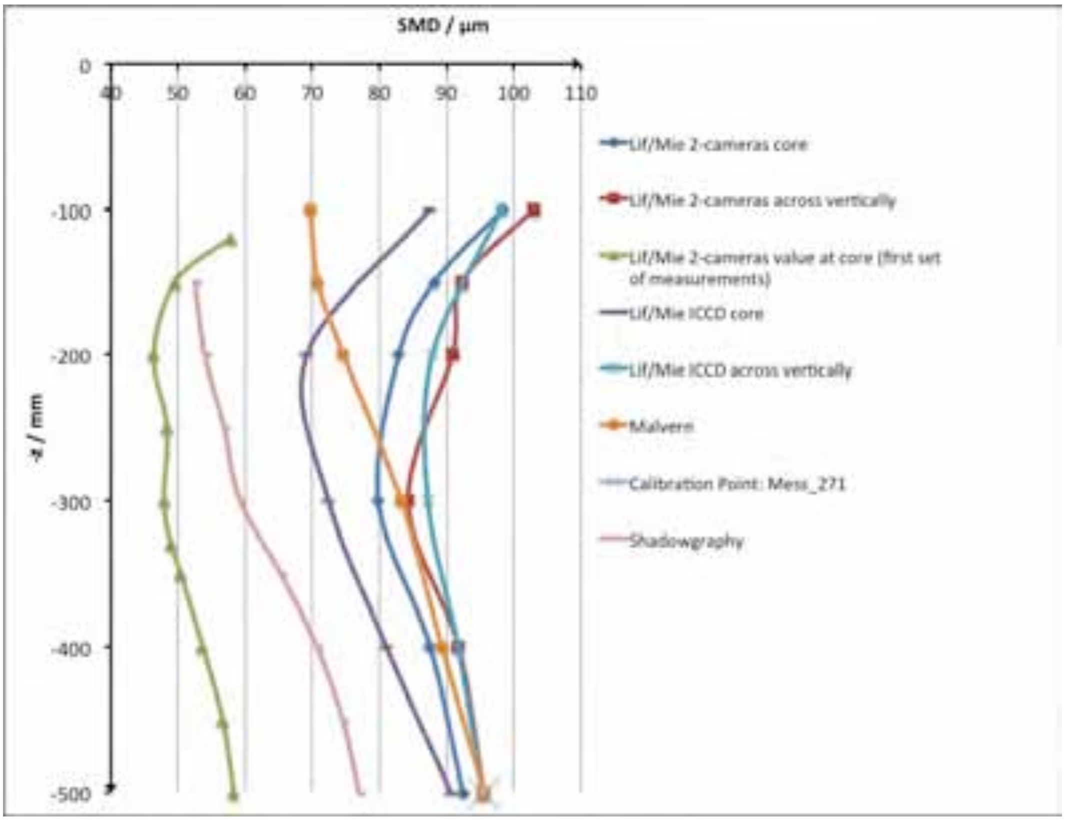

Figure 105: The Le1 nozzle with varying axial distance to the orifice, measured at 4500 mbar.

Both LIF/Mie setups showed an initial decrease of droplet diameter up to 200mm or 300mm distance to orifice, followed by a continuous increase. While diffractometry and shadowgraphy generally agreed with the trend of LIF/Mie measurements did not record an the initial decrease of diameter.

6.10 Discussion of LIF/Mie records

6.10.1 Mee nozzle pressure variation

Regarding the Mie nozzle recorded with the 2-camera setup (Figure 106.a-d) a big difference in terms of shape of the spray was obvious. At low pressure, individual jets coming out of the fog-like spray can be seen in Figure 106 a-d. With increasing pressure, they gradually reduced, until a homogeneous but not symmetrical spray area was seen at 138,000 mbar. The ICCD setup on the other side did not show those jets. In Figure 107.a-d it can be seen, that from 35,000 mbar on there was a reasonably homogenous spray. At no time the spray was resolved as fine as with the 2-camera setup. As in all the other records of the Mee nozzle, on the top and on the bottom of the spray, there were regions of extremely high droplet sizes, which could not be explained physically. It must have come from the measurement system.

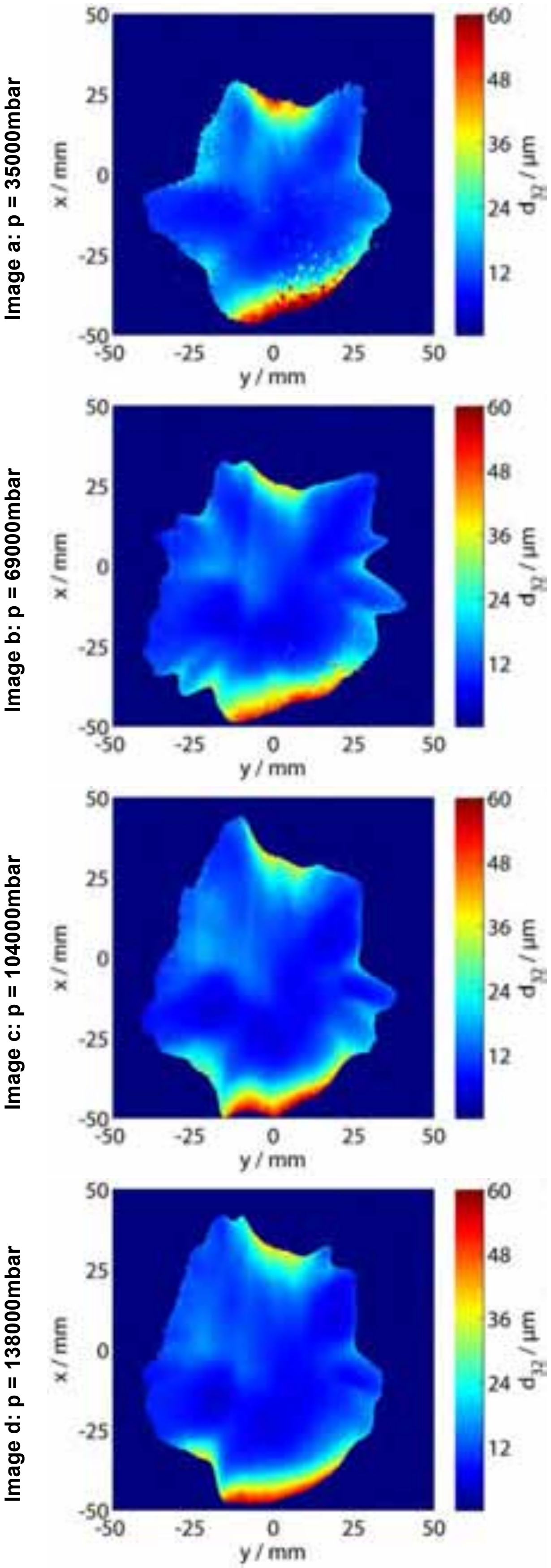

Figure 106.a-d: The Mee nozzle with varying pressure recorded with the 2-camera setup.

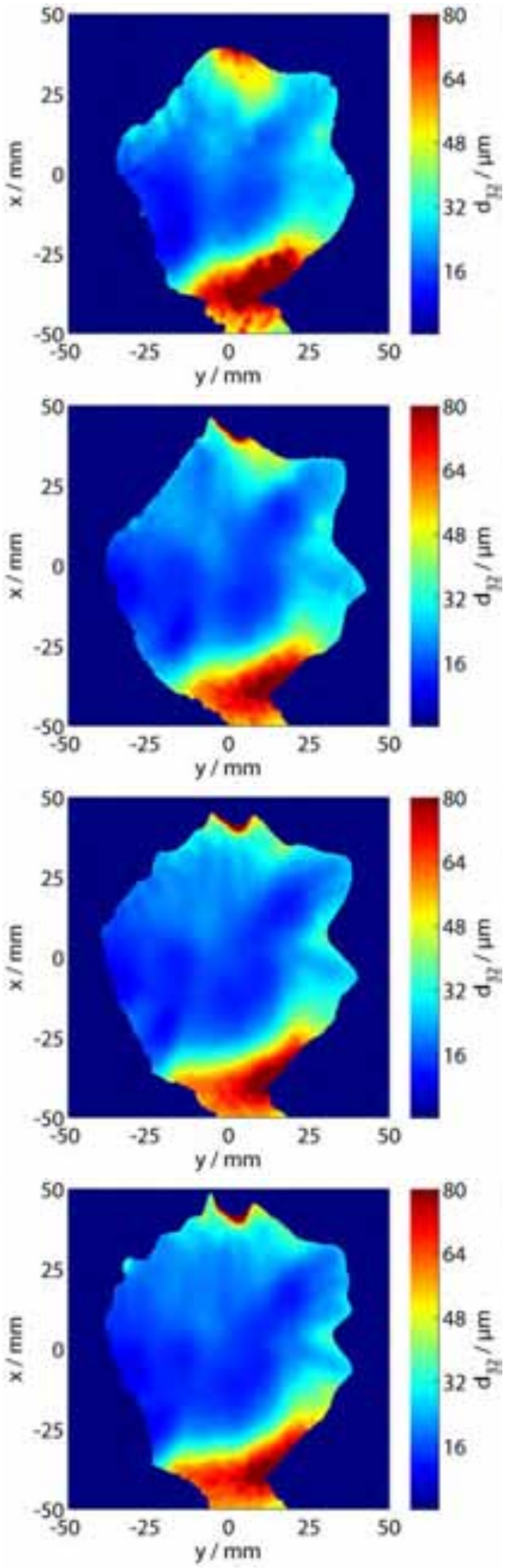

Figure 107.a-d: The Mee nozzle with varying pressure recorded with the ICCD setup.

6.10.2 Mee nozzle – distance to orifice variation

Generally Figure 108.a-f and Figure 109.a-f show a good agreement between the ICCD and the CCD setups. In both the spray tilted down (-x direction) and both presented a similar droplet diameter. In Figure 109.a it can be seen, that the edge of the spray has the same shape as the profile of the nozzle head. The nozzle blocks the light of the droplets, located in the positive x direction. Comparing Figure 108.b and Figure 109.b the difference in image quality got obvious. The ICCD camera's image The 2-camera picture appeared a lot smoother. This can be explained by the fact that the ICCD camera's SXGA chip provided only a quarter of the pixels of the CCD's UXGA chip, and therefore has less resolution.

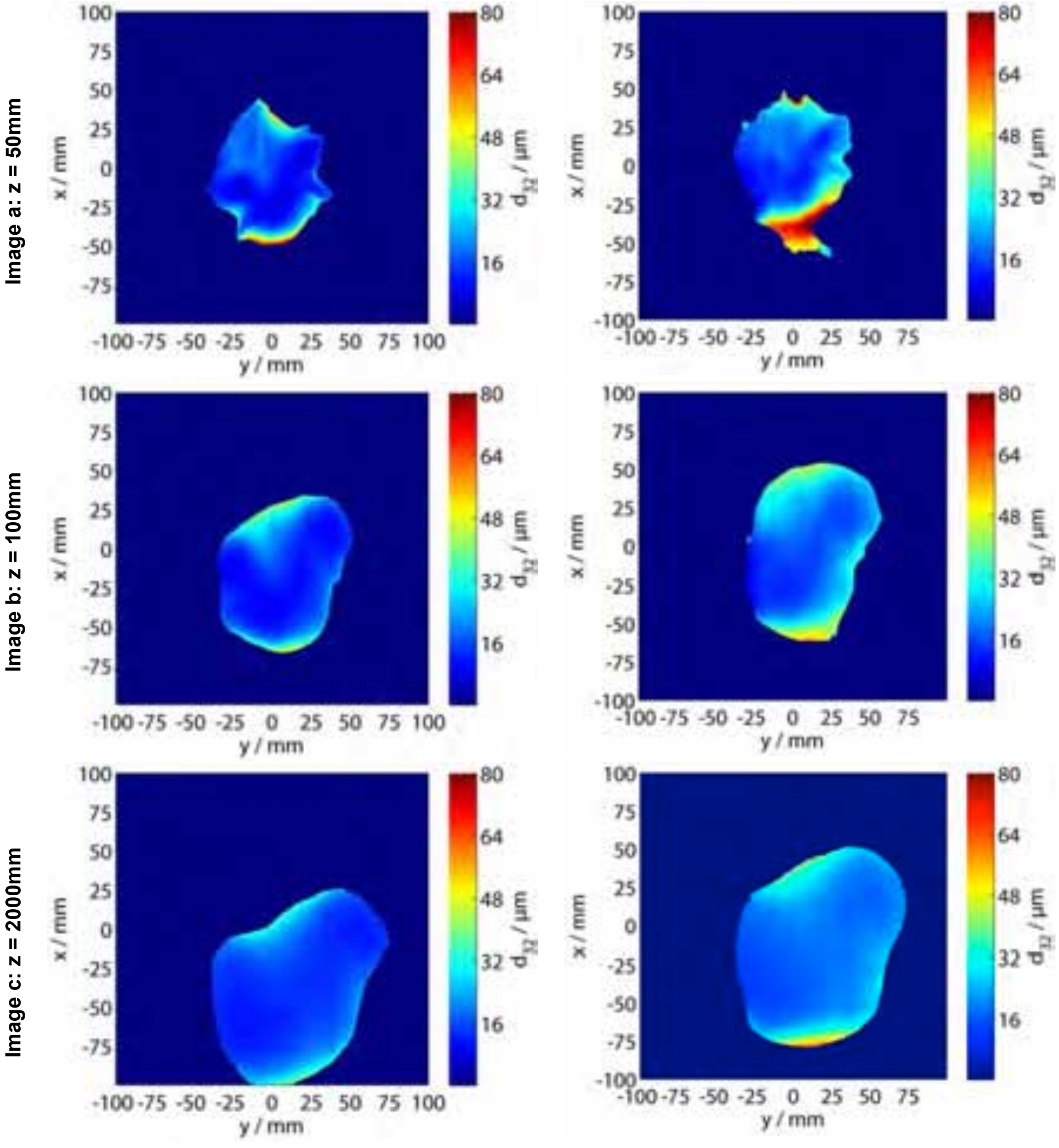

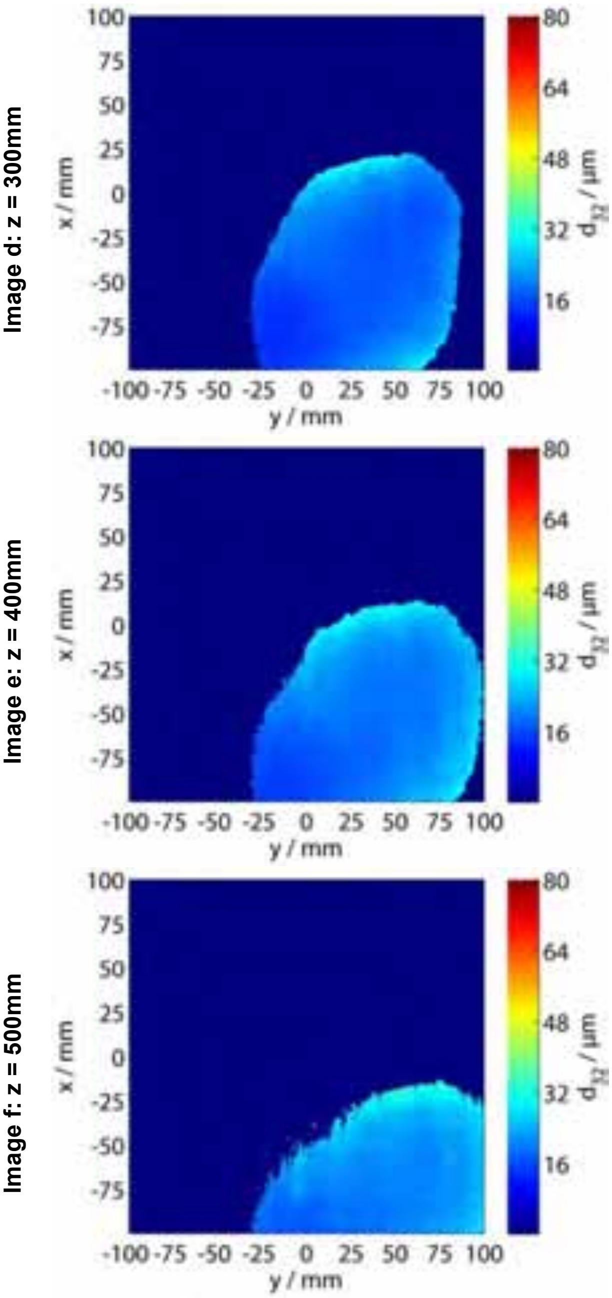

Figure 108.a-f: The Mee nozzle with varying distance to orifice, recorded with the 2-camera setup.

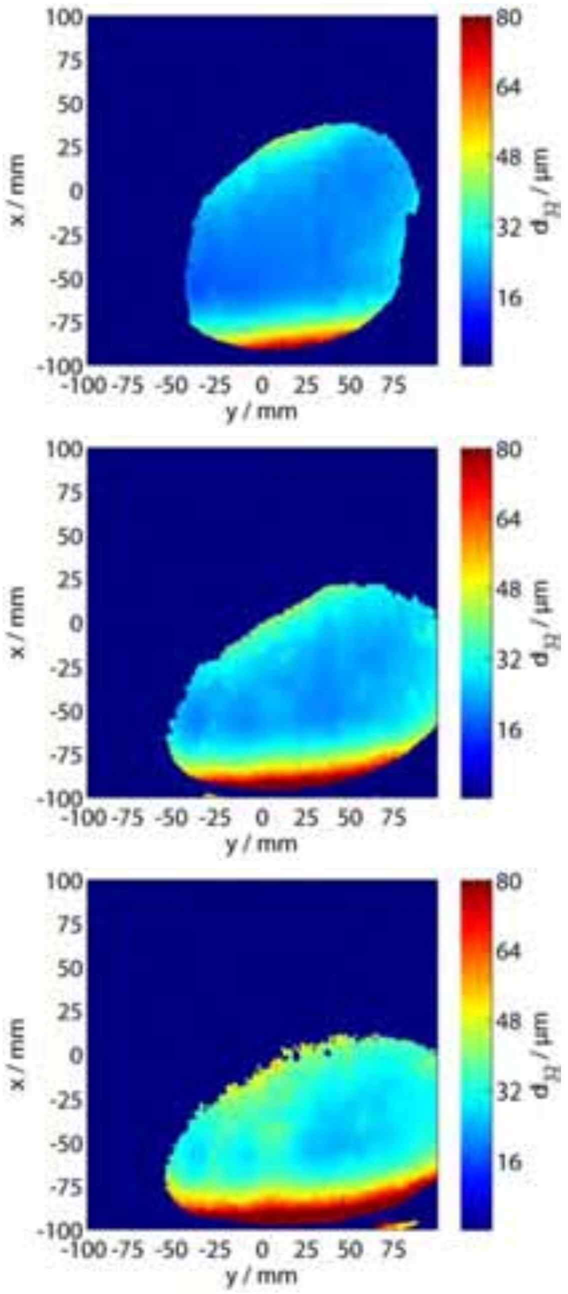

Figure 109.a-f: The Mee nozzle with varying distance to orifice, recorded with the ICCD setup.

6.10.3 Pressure Variation of the pilot oil nozzles

Both, OP-P12 shown in Figure 110.a-e and OP-37 shown in Figure 111.a-e were recorded using the 2 camera setup. The nozzles were designed to have 2 jets rich in droplets in a global spray of low density. Comparing the two, it can be seen, that only OP-P12 kept those jets at pressures as high as 40,000 mbar. The OP-37 was able to properly keep them until 10,000 mbar. At 20,000 mbar they were still existent, but at 30,000 mbar they are absolutely gone. Never the less at both sprays a trend towards homogeneity and smaller droplet size became obvious with increased distance.

Regarding the OP-P12 nozzle, a clockwise rotation of the jets was observed with increasing pressure.

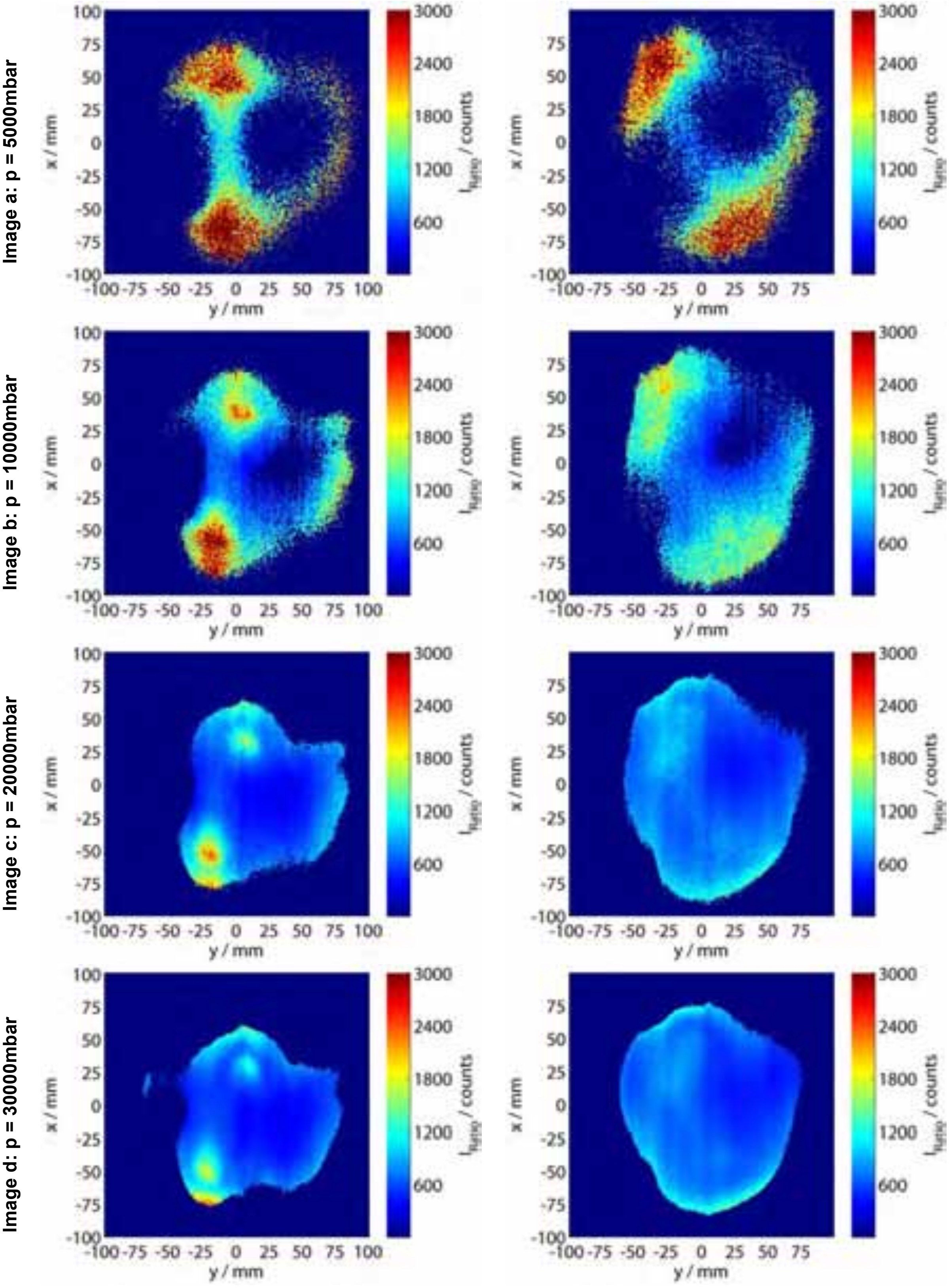

Image e: p = 40000mbar

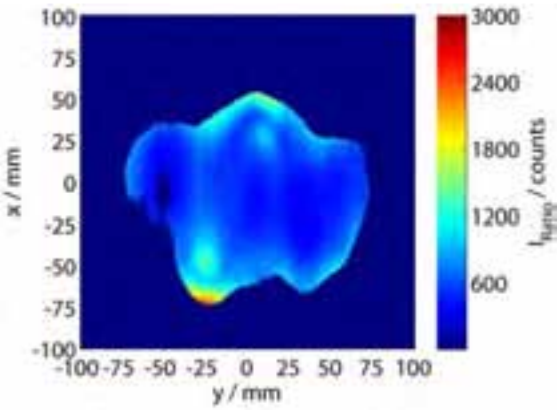

Figure 110.a-e: The op-p12 nozzle, set to a 200mm distance to orifice, with varying pressure recorded with the 2-camera setup,.

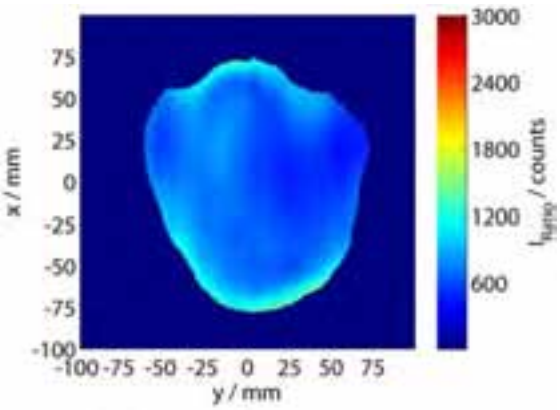

Figure 111.a-d: The op-37 nozzle, with varying pressure recorded with the ICCD setup. The distance to orifice was 200mm except for Figure 111.a were it was only 100mm.

6.10.4 Le1 - Pressure variation

Regarding Le1’s records in Figure 112.a-e the rough surface of the spray was seen. Compared to the Mee nozzle, the edges were not as well defined, although the sample size was identical with 200 shots per measurement point.

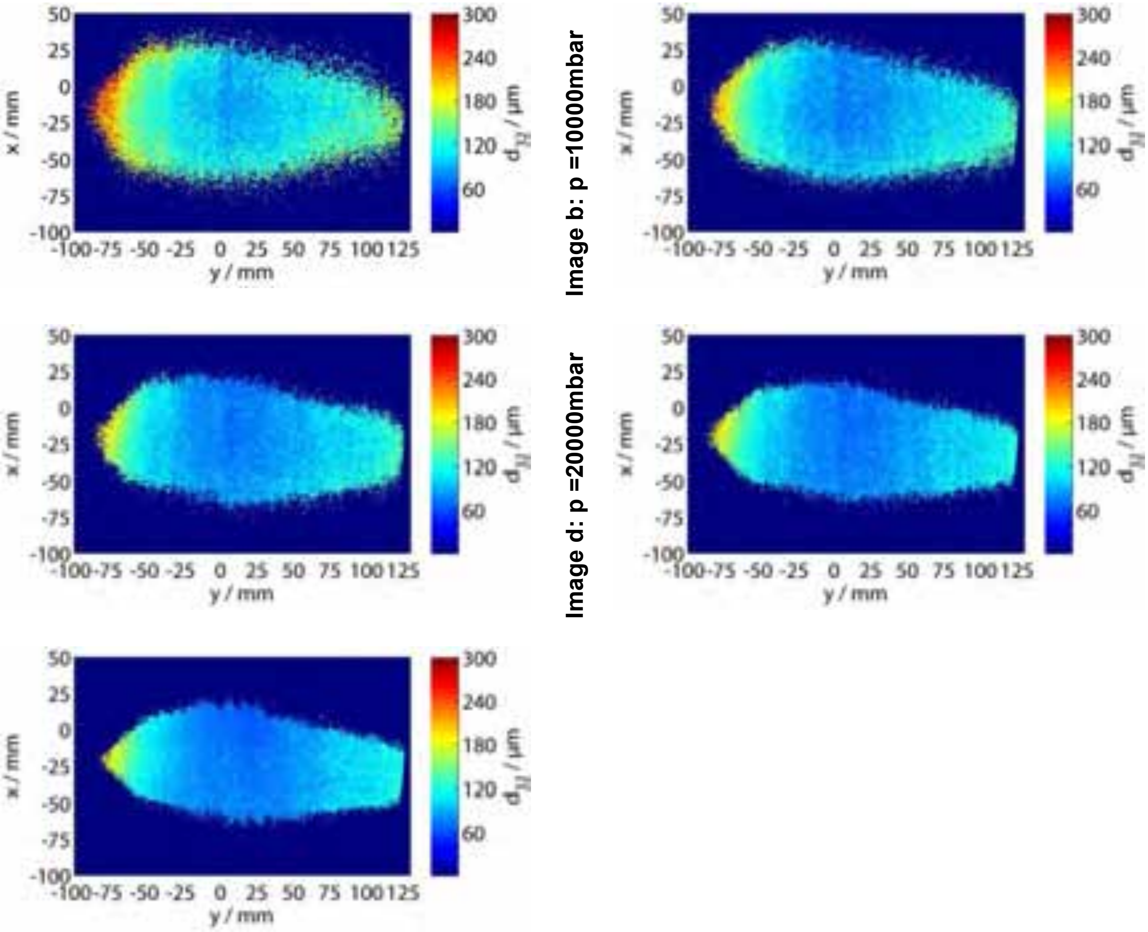

Image a: p =4500mbar

Image b: p =10000mbar

Image c: p =15000mbar

Image d: p =20000mbar

Image e: p =25000ar

Figure 112.a-e: The Le1 nozzle, set to a 500mm distance to orifice, with varying pressure from 4500 to 25000 mbar, recorded with the 2-camera setup.

Looking at the difference of the individual Le1 records, again a diameter drop with increased pressure was evident. The spray got more and more compact with increaseing pressure.

6.10.5 Pulsation

Although there was no pulsation visible to the eye, it was localized. The images (Figure 81 and Figure 115) were calculated by subtracting 10 single shots from the average. The resulting images were then themselves averaged. These pictures are compared to the averaged images in Figure 80 and Figure 115.

The Mee nozzle pulsation was limited to the edge of the spray while the core did not show any variation in time. The Le1 on the other side was highly turbulent and showed variation even in the very core of the spray. One explanation for the phenomenon could be the higher number of droplets in the Mee nozzle. While both nozzles were recorded with the same number of images, the number of particles on each Mee image was many times higher as the number on the Le1 images.

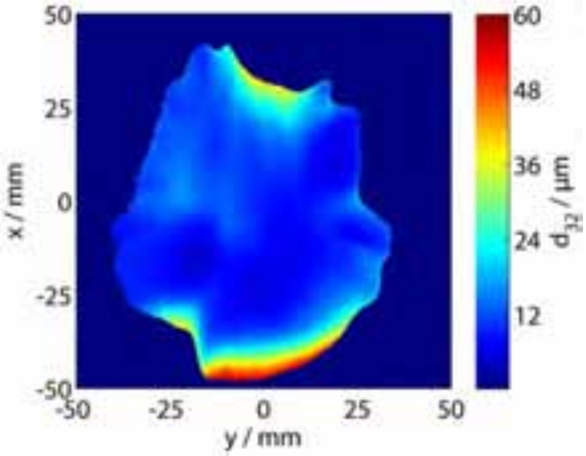

Figure 113: The Mee nozzle, recorded in standard conditions with 200 images averaged.

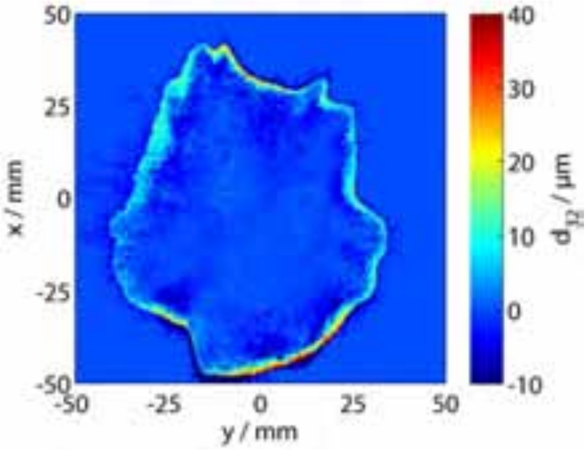

Figure 114: The spray pulsation of the Mee nozzle at standard conditions.

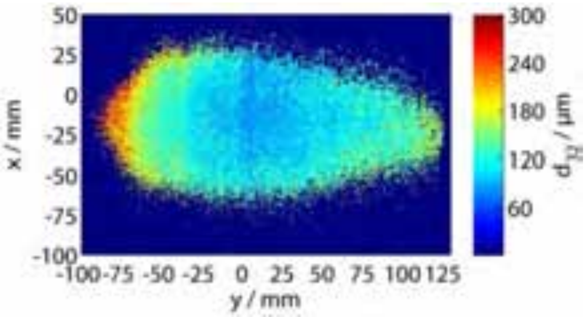

Figure 115: The Le1 nozzle, recorded in standard conditions with a sample number of 200 images.

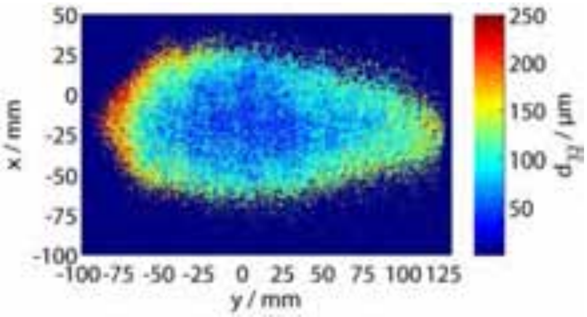

Figure 116: Pulsation of the Le1 nozzle at standard conditions.

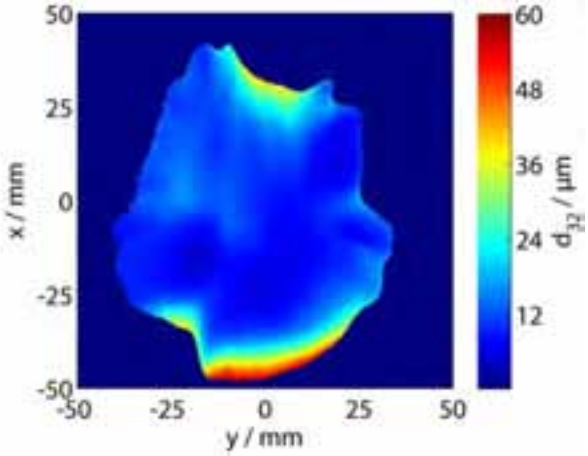

Figure 117: The Mee nozzle, recorded in standard conditions with 200 images averaged.

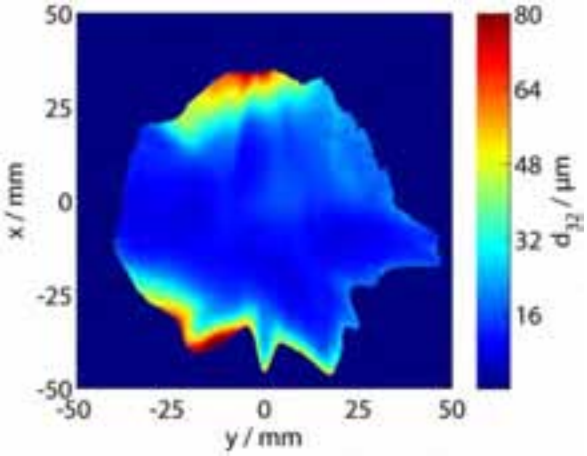

Figure 118: An image of the Mee nozzle at standard conditions, with the nozzle rotated by 90°.

6.10.6 Rotation of the nozzle

In order to prove, that the unreasonably high droplet diameters on top and bottom of the spray (Figure 117) were caused by the physics of the measurement system and were not part of the actual spray, the nozzle was rotated 90° counter clockwise and recorded with the same settings. Surprisingly, not only the regions of big particles

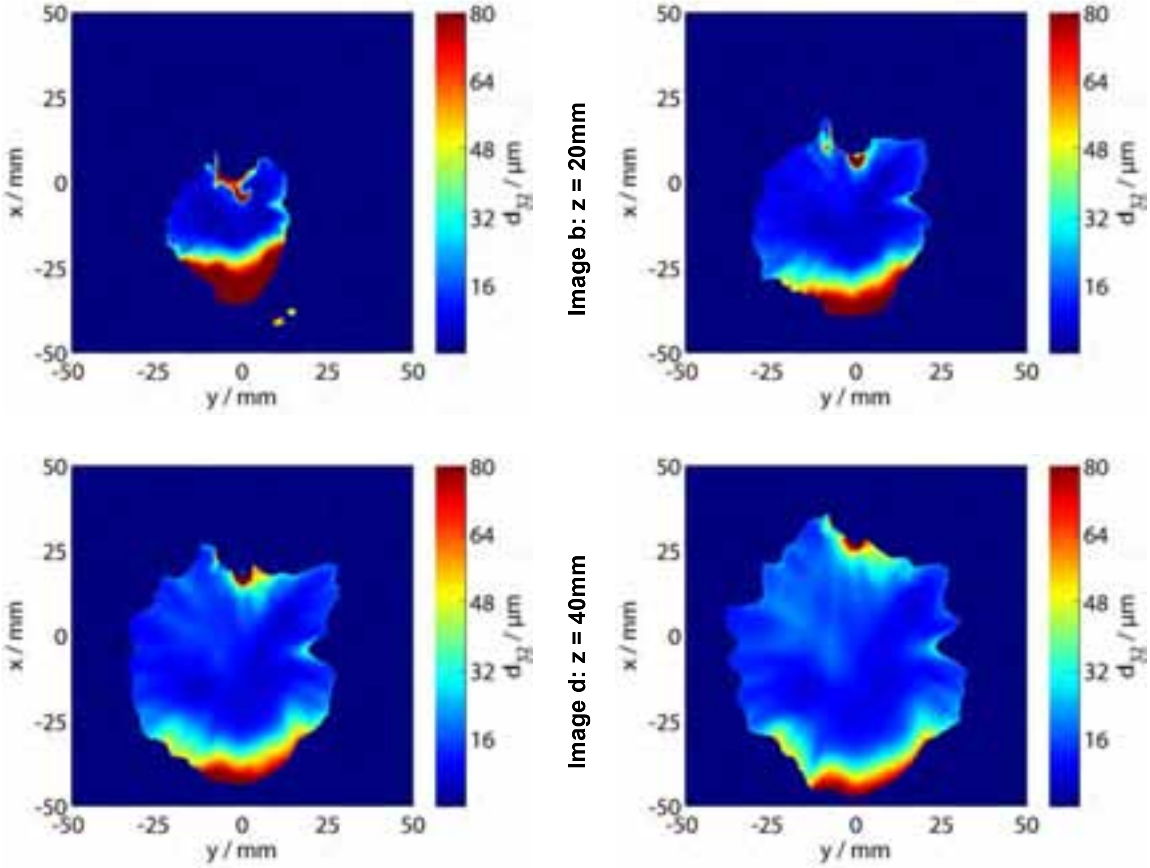

Image a: z = 10mm

Image b: z = 20mm

Image c: z = 30mm

Image d: z = 40mm

Figure 119.a-d: The Mee nozzle with varying distance to orifice in the region between z = 10mm and 40mm.

have moved, but also the spray was a lot more structured, some fingers of the spray came out at the bottom and right side. This shows that the measurement method was not unaffected by highly dense sprays such as the one from the Mee nozzle.

The close shots between 10mm and 40mm off the orifice are presented in Figure 119. As already seen in Figure 108.a-f, the miss-recording at the bottom of the spray was even stronger the closer the measurement plane came to the orifice. In contrast to that the fine pattern shown on the left and right side of the spray, which is particularly developed in Figure 119.d looked a lot more reasonable. White lines were observed, coming from the nozzle head and spreading downwards. They seemed to originate off the measurement plane, somewhere at the edge of the spray between laser sheet and nozzle.

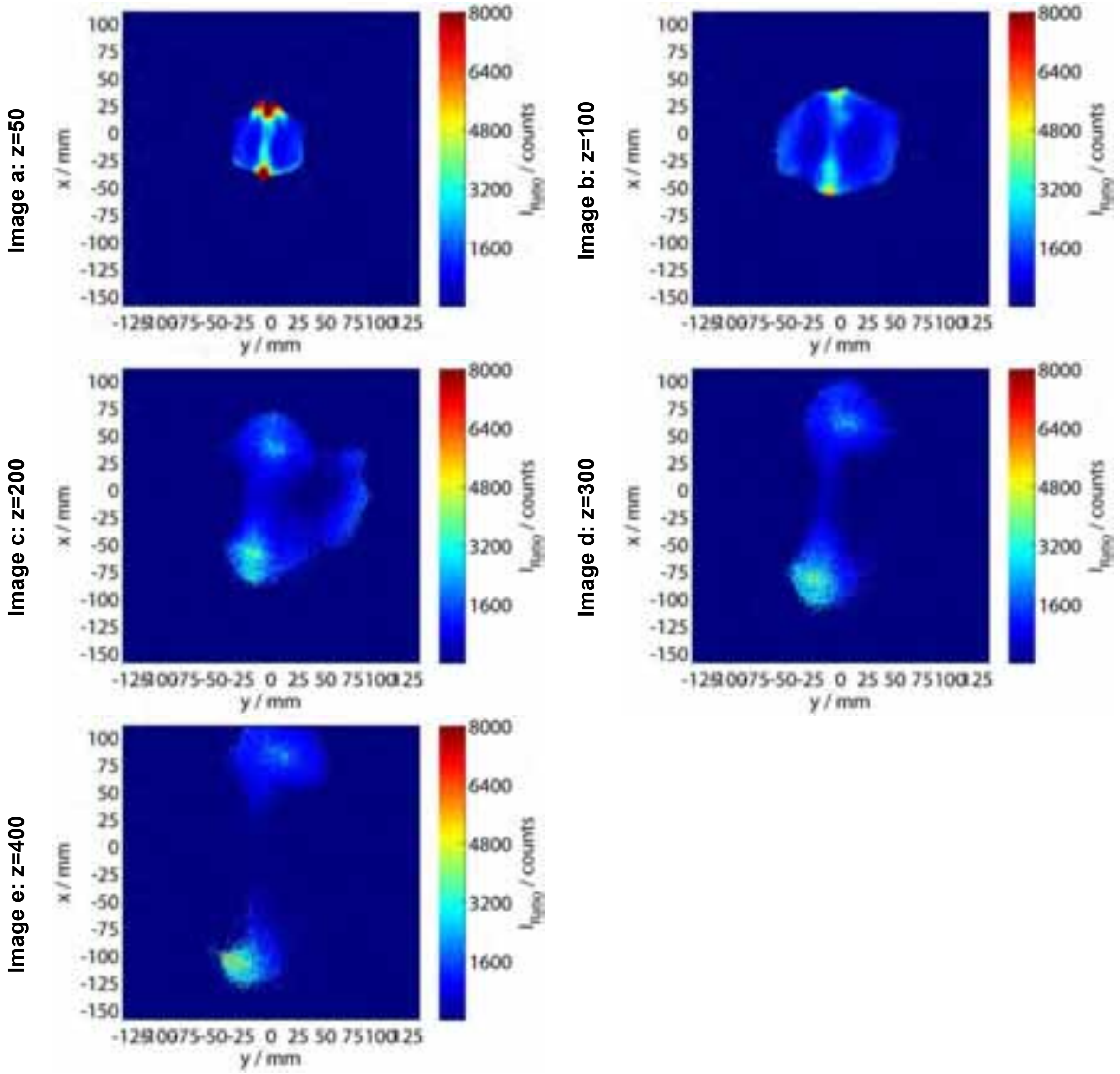

Figure 120.a-e: The OP-P12 nozzle, set to 10,000 mbar, with varying distance to orifice from 50 to 400mm, recorded with the 2-camera setup.

6.10.7 Pilot oil nozzle – variation of distance to orifice

Regarding Figure 120.a extremely high intensity can be observed. This might show, that in this region, the jet did not break up jet. Furthermore the spray's cross section was almost circular. At z=100mm it already started to break up, and further down the axis only the two jets were left. Around these rich areas the signal strength was not high enough, and therefore was cut off by the defined threshold.

Surprisingly, the distance did not change the position of the jets. In contrast to the pressure variation of Chapter 6.10.3, they were fix in rotational direction. On the other side, variation of z caused the jets to spread in radial distance.

7 Summary and conclusions

In this work a planar droplet sizing system in a 45° forward scattering configuration applied to the atmospheric test rig in Alstom's Spray lab in Birr, Switzerland was investigated. The system used laser-induced-fluorescence (LIF) and Mie scattering to record the diameter of droplets in a spray. This laser-optical sytem was build by LaVision (LaVision, Göttingen, Germany). It was the first time that such a system was used to investigate fuel injection systems at Alstom (Birr, Switzerland). Therefore this thesis was performed at Alstom.

As a first step, nozzles of appropriate characteristics were selected, and the manufacturers specifications were validated with a Malvern (Malvern, Great Britain) diffraction system and a LaVision (LaVision, Göttingen, Germany) shadowgraphy system. The Mee Nozzle (IP-16, Mee Industries Inc. Monrovia, California, USA), originally intended for gas turbine inlet fogging, was particularly interesting, since a very detailed paper was published (Chaker et al. 2002 & 2003). Measurements generally agreed with the datasheets, although there were parameters, which prohibit an exact comparison. For example, Lechler (Metzingen, Germany) does not define the type of measurement system, or how their results have been acquired. Mee Inc. on the other hand does not specify which way their nozzle was built in, or how much the nozzles vary among each other.

There was quite a discrepancy between the integrative measurement technique provided by the diffraction based system, and the point-measurement technique shadowgraphy. Regarding disperse sprays, one cannot be sure, how much the diversity of the spray contributed to a different result. Therefore, particles of known distribution have been investigated. These particles, originally intended for PIV measurements and not spherical, showed that the diffraction-based system provided by Malvern Inc. was the more reliable system. The doubts about Shadowgraphy's accuracy still remain.

In a next step, the behavior of Mie scattering was experimentally and computationally validated. A camera support was built up, optimized for a quick change of angles rather than superior stiffness. The variation of angles was recorded for backscattering and compared with the Lorenz-Mie theory using the computer program Mieplot (Laven, 2011, *http://www.philiplaven.com/mieplot.html*). The power-law relation of Mie scattering was verified.

The main part of the work was started with an analysis of background and white sheet correction in order to define the necessary number of images averaged for the background and to find a suitable setup for the white sheet recording. From 500 images on, increasing the number of samples did not make a difference for the background image. Concerning the white sheet, acquisition from a white computer screen proved to work well, and produced a good sheet-image for reference.

Processing was kept with LaVision's suggestion. Additionally, a macro was written in order to shift the images against each other for a perfect match, tackling the main problem of the 2-camera setup, which was mechanical play of the lenses resulting in a low reproducibility of aligned images.

.

The actual measurements were structured in two parts. Firstly, a comparison of the different nozzles with diffractometry, shadowgraphy and the two LIF/Mie was presented. By variation of the pressure and the distance to orifice, a fine diameter grading was achieved with only 3 nozzles. The same nozzle conditions were used for comparing the 2-camera setup and the ICCD setup.

Finally, a pilot oil nozzle used in current combustors was recorded in order to prove the systems capabilities on an actual piece of interest (OP-37 pilot oil nozzle, Alstom).

Regarding the LIF/Mie setup in general, it was possible to prove the capabilities of the system, being a qualitative measurement system. The correlations with pressure variation were very good, while the variation of distance to orifice did not match, the reference date the way they should. Here, apparently an influence of spray density is present. The spray density is also a critical factor with nozzles generating big droplets. Since less pressure meant less but larger droplets, the spray got less dense which was a problem to the measurement system. If, for example, only one out of ten images saw a droplet in a certain position, averaging them resulted in a tenth of the original intensity measured. This limited the system to medium to high-density sprays with little to medium turbulence.

Comparing the two setups, the ICCD version was clearly the sleeker configuration, as there were less parts and cables lying around. The camera unit was also a lot more compact, since there was no T-bar in order to hold 2 cameras and a beam splitter. Using our equipment, four times more pixels per image did affect resolution, to a degree were it became visible to the eye. The Nanostar ICCD was quite an old model. New ones would have a higher chip resolution. Under these conditions, the ICCD system should be the preferred solution. Never the less, the two camera setup was a good alternative, when it was required to only use parts which were already available in the Spraylab.

Taking the given measurement results into consideration, it can be said, that:

The accuracy of the LIF/Mie method is not high enough to be used by itself. Therefore it does not replace point measurement techniques such as PDA or Shadowgraphy.

According to LaVision (2010) generally uncertainties are not less than 30% at optimal conditions. Regarding the results of this thesis, the calibration was not valid for a wide range of droplet sizes. Currently, a linear characteristic is used for data reduction, but the error caused by the nonlinearity of the characteristic of the actual spray, is too big when calibrating for a wide range of droplet diameters.

7.1 Further Improvements suggested

The Nikon 1.8D lens used was manufactured for consumer SLR-Cameras. The focal ring had too much play and shifted the image perpendicular to the optical axis. Only touching the lens could therefore result in an image displacement of up to 5 pixels. Matching of the LIF- and Mie image was essential, otherwise a systematic error was unnecessarily introduced to the droplet diameter. The lens play of the 2-camera setup was finally reduced in a software processing step, which was reliable but time consuming for the user and did not contribute to simplicity of the system, which would be essential for daily use. The problem could generally be avoided by replacing these lenses by a more reliable brand, in order to desensitize the system towards vibration or a person accidentally touching the setup.

For future work, proof of concept at the High Density Fluid Channel (HDFC) is suggested. The T-bar camera support was designed to be moved quickly from one rig to the next. Therefore only experimental desing how to set up the laser sheet including the beam traps and the shadowgraphy system would be necessary.

Assuming an increased demand for testing and validation of sprays in the near future, a droplet generator would be an important investment. Then every measurement system could be calibrated properly. A lot of time could be saved when further investigations of the reliability of the systems shadowgraphy and diffractometry get necessary.

Integration of a polynomic calibration curve should be a priority when the LIF/Mie system shall be used for daily research business. The characteristic used in this work, was linear with one data point at the origin, this assumption of linearity introduced an unnecessary error.

Further investigation on the assumption of a planar measurement sheet should be made in order to approach the problem of unreasonably large droplets measured at the lower side of the Mee nozzle’s spray.

A solution to the spray density problem could be implemented as follows. As described in chapter 6.8.1, averaging the images after processing, introduced an error. This would no longer be the case, when only pixels were considered for averaging which do not count zero. Then it would be possible to process images individually first, and then average, only considering pixels with counts.

References

Albrecht et al. 2003	Albrecht, H.-E.; Borys, M.; Damaschke, N.; Tropea, C.: Laser Doppler and Phase Doppler Measurement Techniques. Berlin: Springer, 2003, ISBN 3-540-67838-7
Chaker et al. 2002	Chaker, M.; Cyrus, B.; Mee, T.: *INLET FOGGING OF GAS TURBINE ENGINES – PART B: FOG DROPLET SIZING ANALYSIS, NOZZLE TYPES, MEASUREMENT AND TESTING.* Proceedings of the ASME Turbo Expo 2002 paper 2002-GT-30563
Chaker et al. 2003	Chaker, M.; Cyrus, B.; Mee, T.: *INLET FOGGING OF GAS TURBINE ENGINES – EXPERIMENTAL AND ANALYTICAL INVESTIGATIONS ON IMPACTION PIN FOG NOZZLE BEHAVIOR*. Proceedings of the ASME Turbo Expo 2003 paper 2003-GT-38801
Charalampous and Hardalupas 2011 a	Charalampous, G.; Hardalupas, Y.: *Numerical evaluation of droplet sizing based on the ratio of fluorescent and scattered light intensities (LIF/Mie technique).* Applied Optics Vol. 50 (2011) Nr. 9 P.1197-1209
Charalampous and Hardalupas 2011 b	Charalampous, G.; Hardalupas, Y.: *A novel method to reduce errors of droplet sizing based on the ratio of fluorescent and scattered light intensities (LIF/Mie technique).* To be posted in Applied optics (2011) Doc. ID: 144138
Greenhalgh 1994	Greenhalgh, D.: *Inelastic Scattering Laser Diagnostics; CARS, PLANAR LIF AND PLANAR LII.* in: *Optical Diagnostics for Flow Processes* New York: Plenum Press, 1994, ISBN 0-306-44817-3
Laven 2011	Online: Laven, P.: *Mieplot program and manual.* Url: *http://www.philiplaven.com/mieplot.html*

LaVision 2010 a	LaVision Gmbh: *Spraymaster D32,* *Product Manual.* *Doc.No.: 1004052_SprayMaster_D32_D80* Göttingen, Germany (2010)
LaVision 2010 b	LaVision Gmbh: *ParticleMaster Shadow D72,* *Product Manual.* *1003014_ParticleMaster_Shadow_D72* Göttingen, Germany (2010)
Ruck 1987	Ruck, B.: *Laser-Doppler-Anemometrie* Stuttgart: AT-Fachverlag, 1987, ISBN 3-921 681-00-6

Appendix A

- **Datasheet for Le1**
- **Datasheet for Le2**
- **Safety instructions for Rhodamine 6g (in German)**

Datasheet of the Le1 nozzle:

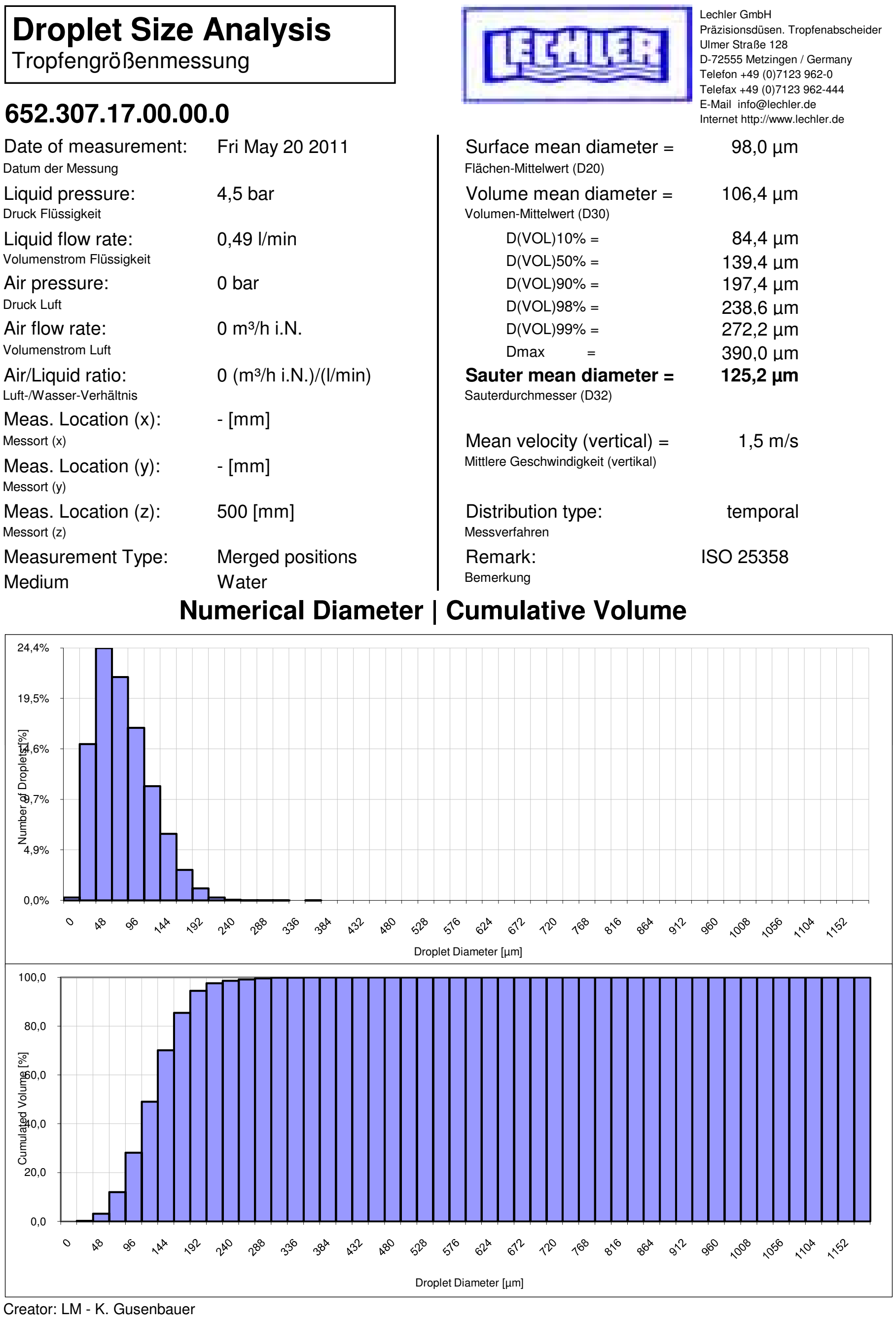

Droplet Size Analysis

Tropfengrößenmessung

Lechler GmbH
Präzisionsdüsen. Tropfenabscheider
Ulmer Straße 128
D-72555 Metzingen / Germany
Telefon +49 (0)7123 962-0
Telefax +49 (0)7123 962-444
E-Mail info@lechler.de
Internet http://www.lechler.de

652.307.17.00.00.0

Date of measurement: Datum der Messung	Fri May 20 2011
Liquid pressure: Druck Flüssigkeit	4,5 bar
Liquid flow rate: Volumenstrom Flüssigkeit	0,49 l/min
Air pressure: Druck Luft	0 bar
Air flow rate: Volumenstrom Luft	0 m³/h i.N.
Air/Liquid ratio: Luft-/Wasser-Verhältnis	0 (m³/h i.N.)/(l/min)
Meas. Location (x): Messort (x)	- [mm]
Meas. Location (y): Messort (y)	- [mm]
Meas. Location (z): Messort (z)	500 [mm]
Measurement Type:	Merged positions
Medium	Water

Surface mean diameter = Flächen-Mittelwert (D20)	98,0 µm
Volume mean diameter = Volumen-Mittelwert (D30)	106,4 µm
D(VOL)10% =	84,4 µm
D(VOL)50% =	139,4 µm
D(VOL)90% =	197,4 µm
D(VOL)98% =	238,6 µm
D(VOL)99% =	272,2 µm
Dmax =	390,0 µm
Sauter mean diameter = Sauterdurchmesser (D32)	**125,2 µm**
Mean velocity (vertical) = Mittlere Geschwindigkeit (vertikal)	1,5 m/s
Distribution type: Messverfahren	temporal
Remark: Bemerkung	ISO 25358

Numerical Diameter | Cumulative Volume

Creator: LM - K. Gusenbauer

Datasheet of the Le2 nozzle:

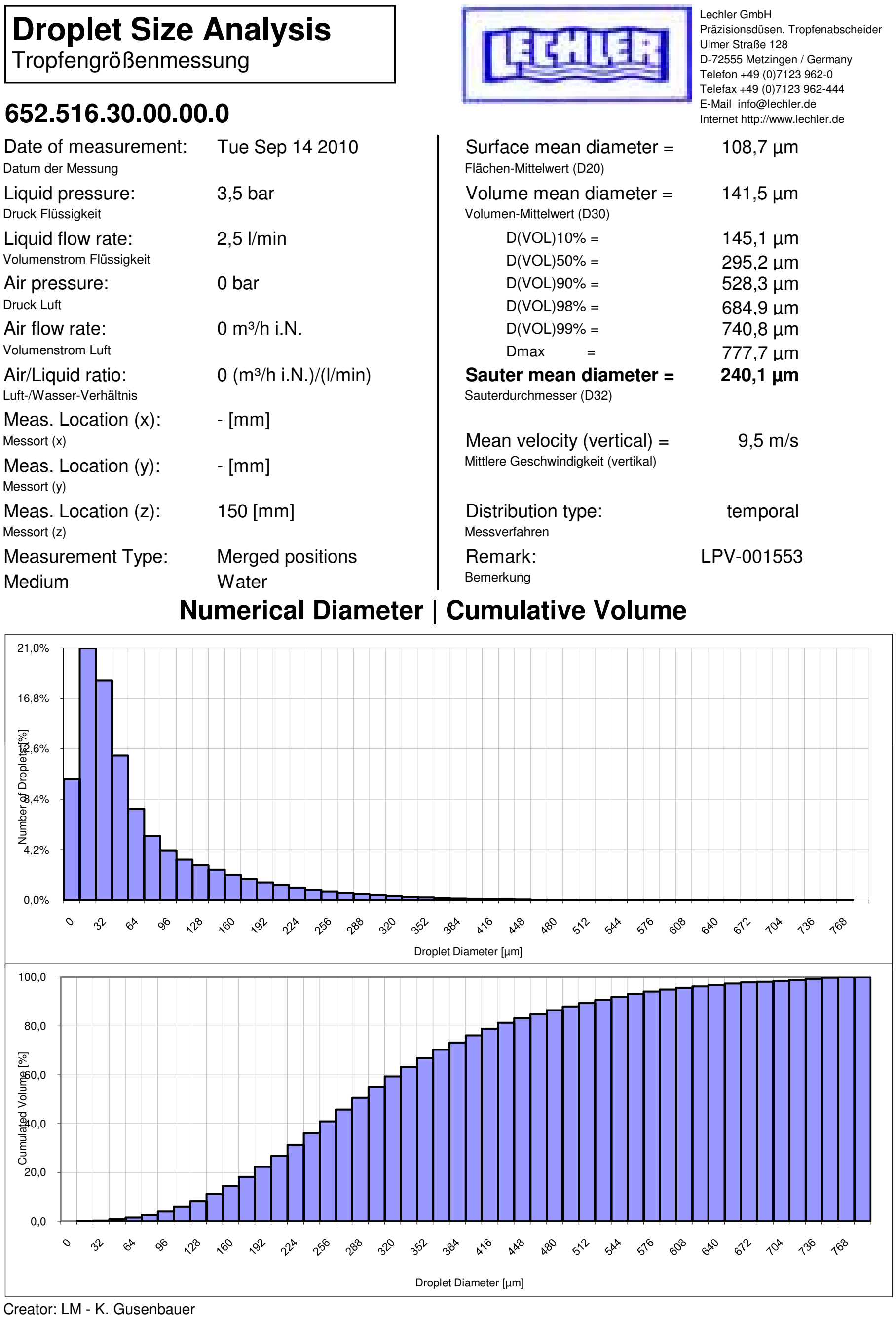

Droplet Size Analysis
Tropfengrößenmessung

Lechler GmbH
Präzisionsdüsen. Tropfenabscheider
Ulmer Straße 128
D-72555 Metzingen / Germany
Telefon +49 (0)7123 962-0
Telefax +49 (0)7123 962-444
E-Mail info@lechler.de
Internet http://www.lechler.de

652.516.30.00.00.0

Date of measurement: Datum der Messung	Tue Sep 14 2010
Liquid pressure: Druck Flüssigkeit	3,5 bar
Liquid flow rate: Volumenstrom Flüssigkeit	2,5 l/min
Air pressure: Druck Luft	0 bar
Air flow rate: Volumenstrom Luft	0 m³/h i.N.
Air/Liquid ratio: Luft-/Wasser-Verhältnis	0 (m³/h i.N.)/(l/min)
Meas. Location (x): Messort (x)	- [mm]
Meas. Location (y): Messort (y)	- [mm]
Meas. Location (z): Messort (z)	150 [mm]
Measurement Type:	Merged positions
Medium	Water

Surface mean diameter = Flächen-Mittelwert (D20)	108,7 µm
Volume mean diameter = Volumen-Mittelwert (D30)	141,5 µm
D(VOL)10% =	145,1 µm
D(VOL)50% =	295,2 µm
D(VOL)90% =	528,3 µm
D(VOL)98% =	684,9 µm
D(VOL)99% =	740,8 µm
Dmax =	777,7 µm
Sauter mean diameter = Sauterdurchmesser (D32)	**240,1 µm**
Mean velocity (vertical) = Mittlere Geschwindigkeit (vertikal)	9,5 m/s
Distribution type: Messverfahren	temporal
Remark: Bemerkung	LPV-001553

Numerical Diameter | Cumulative Volume

Creator: LM - K. Gusenbauer

Rhodamine 6g Data sheet:

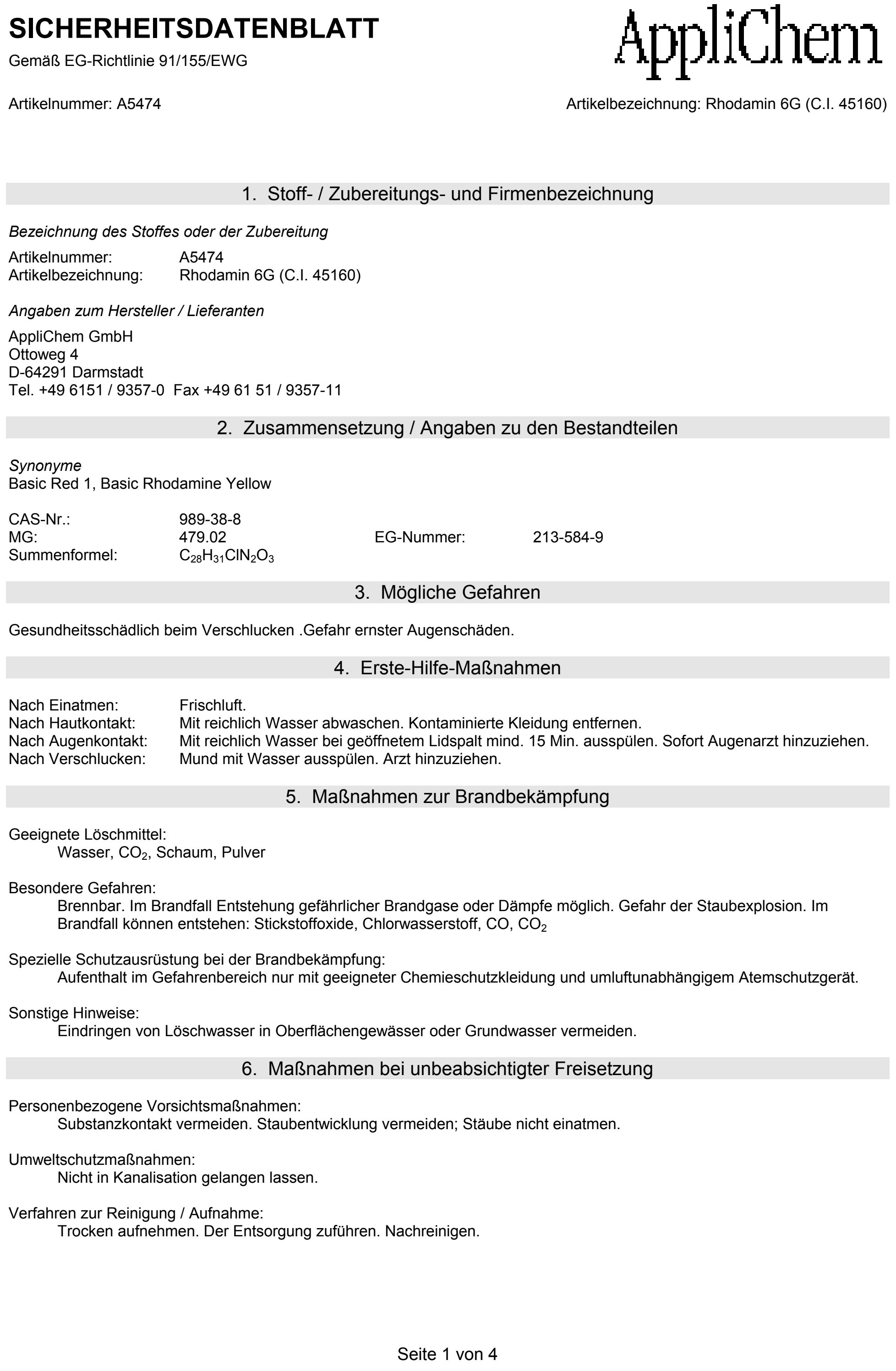

SICHERHEITSDATENBLATT

Gemäß EG-Richtlinie 91/155/EWG

AppliChem

Artikelnummer: A5474
Artikelbezeichnung: Rhodamin 6G (C.I. 45160)

1. Stoff- / Zubereitungs- und Firmenbezeichnung

Bezeichnung des Stoffes oder der Zubereitung

Artikelnummer: A5474
Artikelbezeichnung: Rhodamin 6G (C.I. 45160)

Angaben zum Hersteller / Lieferanten

AppliChem GmbH
Ottoweg 4
D-64291 Darmstadt
Tel. +49 6151 / 9357-0 Fax +49 61 51 / 9357-11

2. Zusammensetzung / Angaben zu den Bestandteilen

Synonyme
Basic Red 1, Basic Rhodamine Yellow

CAS-Nr.: 989-38-8
MG: 479.02 EG-Nummer: 213-584-9
Summenformel: $C_{28}H_{31}ClN_2O_3$

3. Mögliche Gefahren

Gesundheitsschädlich beim Verschlucken .Gefahr ernster Augenschäden.

4. Erste-Hilfe-Maßnahmen

Nach Einatmen: Frischluft.
Nach Hautkontakt: Mit reichlich Wasser abwaschen. Kontaminierte Kleidung entfernen.
Nach Augenkontakt: Mit reichlich Wasser bei geöffnetem Lidspalt mind. 15 Min. ausspülen. Sofort Augenarzt hinzuziehen.
Nach Verschlucken: Mund mit Wasser ausspülen. Arzt hinzuziehen.

5. Maßnahmen zur Brandbekämpfung

Geeignete Löschmittel:
Wasser, CO_2, Schaum, Pulver

Besondere Gefahren:
Brennbar. Im Brandfall Entstehung gefährlicher Brandgase oder Dämpfe möglich. Gefahr der Staubexplosion. Im Brandfall können entstehen: Stickstoffoxide, Chlorwasserstoff, CO, CO_2

Spezielle Schutzausrüstung bei der Brandbekämpfung:
Aufenthalt im Gefahrenbereich nur mit geeigneter Chemieschutzkleidung und umluftunabhängigem Atemschutzgerät.

Sonstige Hinweise:
Eindringen von Löschwasser in Oberflächengewässer oder Grundwasser vermeiden.

6. Maßnahmen bei unbeabsichtigter Freisetzung

Personenbezogene Vorsichtsmaßnahmen:
Substanzkontakt vermeiden. Staubentwicklung vermeiden; Stäube nicht einatmen.

Umweltschutzmaßnahmen:
Nicht in Kanalisation gelangen lassen.

Verfahren zur Reinigung / Aufnahme:
Trocken aufnehmen. Der Entsorgung zuführen. Nachreinigen.

SICHERHEITSDATENBLATT

Gemäß EG-Richtlinie 91/155/EWG

AppliChem

Artikelnummer: A5474

Artikelbezeichnung: Rhodamin 6G (C.I. 45160)

7. Handhabung und Lagerung

Handhabung:
Keine weiteren Anforderungen.

Lagerung:
Dicht verschlossen. Trocken. Bei +5°C bis +30°C.

8. Expositionsbegrenzung und persönliche Schutzausrüstung

Persönliche Schutzausrüstung:

Atemschutz:	erforderlich bei Auftreten von Stäuben.		
Augenschutz:	erforderlich		
Handschutz:	Bei Vollkontakt:		
		Handschuhmaterial:	Nitrilkautschuk
		Schichtstärke:	0.11 mm
		Durchbruchzeit:	>480 Min
	Bei Spritzkontakt:		
		Handschuhmaterial:	Nitrilkautschuk
		Schichtstärke:	0.11 mm
		Durchbruchzeit:	>480 Min

Die einzusetzenden Schutzhandschuhe müssen den Spezifikationen der EG-Richtlinie 89/686/EWG und der sich daraus ergebenden Norm EN374 genügen. Diese Empfehlung gilt nur für das im Sicherheitsdatenblatt genannte Produkt, das von uns geliefert wird und den von uns angegebenen Verwendungszweck. Bei der Lösung in oder bei der Vermischung mit anderen Substanzen und bei den von der EN374 abweichenden Bedingungen, müssen Sie sich an den Lieferanten von CE-genehmigten Handschuhen wenden.

Körperschutzmittel sind in ihrer Ausführung in Abhängigkeit von Gefahrstoffkonzentration und -menge arbeitsplatzspezifisch auszuwählen. Die Chemikalienbeständigkeit der Schutzmittel sollte mit deren Lieferanten abgeklärt werden.

Angaben zur Arbeitshygiene:
Kontaminierte Kleidung wechseln. Vorbeugender Hautschutz empfohlen. Nach Arbeitsende Hände waschen.

9. Physikalische und chemische Eigenschaften

Form:	fest	
Farbe:	braun	
Geruch:	fast geruchlos	
pH-Wert bei 50 g/l H_2O	(20 °C)	~ 5.0
Schmelztemperatur		nicht verfügbar
Siedetemperatur		nicht verfügbar
Zündtemperatur		nicht verfügbar
Flammpunkt		nicht verfügbar
Explosionsgrenzen	untere	nicht verfügbar
	obere	nicht verfügbar
Relative Dampfdichte		nicht verfügbar
Dichte	(20 °C)	nicht verfügbar
Löslichkeit in	Wasser (20 °C)	30 g/l
	Ethanol (20 °C)	10 g/l

SICHERHEITSDATENBLATT

AppliChem

Gemäß EG-Richtlinie 91/155/EWG

Artikelnummer: A5474

Artikelbezeichnung: Rhodamin 6G (C.I. 45160)

10. Stabilität und Reaktivität

Zu vermeidende Bedingungen
keine Angaben vorhanden

Zu vermeidende Stoffe
starke Oxidationsmittel

Gefährliche Zersetzungsprodukte
bei Brand: siehe Kapitel 5.

Weitere Angaben
Staubexplosion möglich.

11. Angaben zur Toxikologie

Akute Toxizität
LD50 (intraperitoneal, Maus): 6150 mg/kg .

Subakute bis chronische Toxizität
Dieses Produkt ist oder enthält einen Bestandteil, der gemäß den KlassierungeN von IARC, ACGIH, NTP oder EPA bezüglich der krebserzeugenden Wirkung nicht eigestuft wird.

Weitere toxikologische Hinweise

Nach Augenkontakt:	Reizungen. Gefahr ernster Augenschäden.
Nach Einatmen:	Reizungen. Möglichweise gesundheitsschädlich
Nach Hautkontakt:	Reizungen. . Möglichweise gesundheitsschädlich bei Absorption.
Nach Augenkontakt:	Reizungen.
Nach Verschlucken:	Möglichweise gesundheitsschädlich.

Weitere Angaben
Weitere gefährliche Eigenschaften können nicht ausgeschlossen werden.
Das Produkt ist mit der bei Chemikalien üblichen Vorsicht zu handhaben.

12. Angaben zur Ökologie

Ökotoxische Wirkungen:
Quantitative Daten zur ökologischen Wirkung dieses Produkts liegen uns nicht vor.

Weitere Angaben zur Ökologie:
Nicht in Gewässer, Abwasser oder Erdreich gelangen lassen!

13. Hinweise zur Entsorgung

Produkt:
Es liegen keine einheitlichen Bestimmungen zur Entsorgung von Chemikalien in den Mitgliedsstaaten der EU vor. In Deutschland ist durch das Kreislaufwirtschafts- und Abfallgesetz (KrW/AbfG) das Verwertungsgebot festgeschrieben, dementsprechend sind "Abfälle zur Verwertung" und "Abfälle zur Beseitigung" zu unterscheiden.
Besonderheiten - insbesonders bei der Anlieferung - werden darüber hinaus auch durch die Bundesländer geregelt. Bitte nehmen Sie mit der zuständigen Stelle (Behörde oder Abfallbeseitigungsunternehmen) Kontakt auf, wo Sie Informationen über Verwertung oder Beseitigung erhalten.

Verpackung:
Entsorgung gemäß den behördlichen Vorschriften. Kontaminierte Verpackungen sind wie der Stoff zu behandeln. Sofern nicht behördlich geregelt, können nicht kontaminierte Verpackungen wie Hausmüll behandelt oder einem Recycling zugeführt werden.

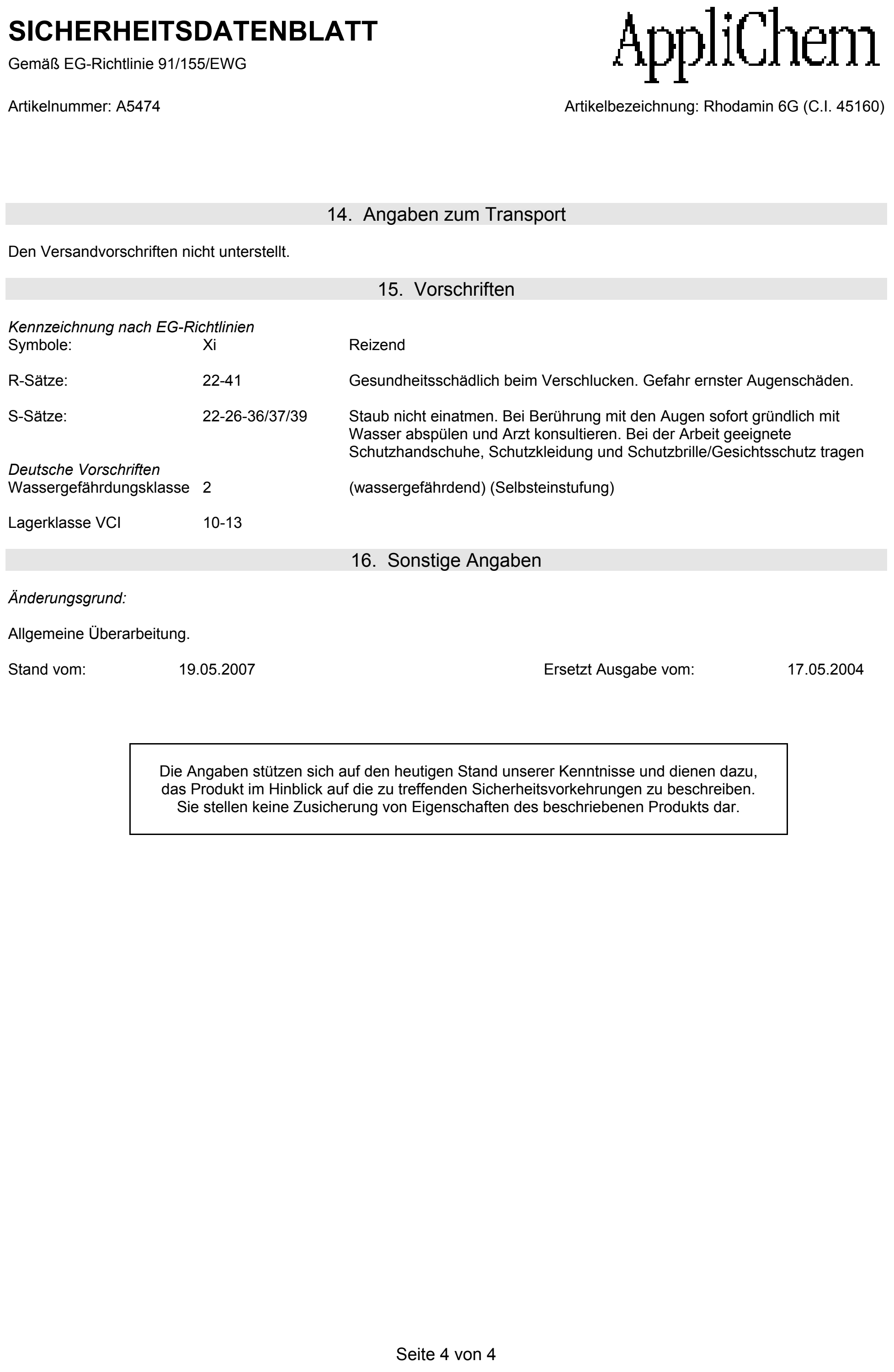

SICHERHEITSDATENBLATT

Gemäß EG-Richtlinie 91/155/EWG

AppliChem

Artikelnummer: A5474 Artikelbezeichnung: Rhodamin 6G (C.I. 45160)

14. Angaben zum Transport

Den Versandvorschriften nicht unterstellt.

15. Vorschriften

Kennzeichnung nach EG-Richtlinien		
Symbole:	Xi	Reizend
R-Sätze:	22-41	Gesundheitsschädlich beim Verschlucken. Gefahr ernster Augenschäden.
S-Sätze:	22-26-36/37/39	Staub nicht einatmen. Bei Berührung mit den Augen sofort gründlich mit Wasser abspülen und Arzt konsultieren. Bei der Arbeit geeignete Schutzhandschuhe, Schutzkleidung und Schutzbrille/Gesichtsschutz tragen
Deutsche Vorschriften		
Wassergefährdungsklasse	2	(wassergefährdend) (Selbsteinstufung)
Lagerklasse VCI	10-13	

16. Sonstige Angaben

Änderungsgrund:

Allgemeine Überarbeitung.

Stand vom: 19.05.2007 Ersetzt Ausgabe vom: 17.05.2004

Die Angaben stützen sich auf den heutigen Stand unserer Kenntnisse und dienen dazu, das Produkt im Hinblick auf die zu treffenden Sicherheitsvorkehrungen zu beschreiben. Sie stellen keine Zusicherung von Eigenschaften des beschriebenen Produkts dar.

Appendix B – CD: Planar droplet sizing LIF/Mie

- **Figures in high resolution**
- **Processing document file for Shadowgraphy**
- **DaVis - Macros**
- **List of Measurements**
- **Matlab Processing file**
- **Images from the Spraylab at Alstom**